

University of Windsor

## Scholarship at UWindor

---

Electronic Theses and Dissertations

Theses, Dissertations, and Major Papers

---

2012

### Sliding Wear of a Squeeze Cast Magnesium Composite AM60-(Al<sub>2</sub>O<sub>3</sub>)<sub>f</sub> at Low Loads

Anindya Banerji  
*University of Windsor*

Follow this and additional works at: <https://scholar.uwindsor.ca/etd>

---

#### Recommended Citation

Banerji, Anindya, "Sliding Wear of a Squeeze Cast Magnesium Composite AM60-(Al<sub>2</sub>O<sub>3</sub>)<sub>f</sub> at Low Loads" (2012). *Electronic Theses and Dissertations*. 172.  
<https://scholar.uwindsor.ca/etd/172>

This online database contains the full-text of PhD dissertations and Masters' theses of University of Windsor students from 1954 forward. These documents are made available for personal study and research purposes only, in accordance with the Canadian Copyright Act and the Creative Commons license—CC BY-NC-ND (Attribution, Non-Commercial, No Derivative Works). Under this license, works must always be attributed to the copyright holder (original author), cannot be used for any commercial purposes, and may not be altered. Any other use would require the permission of the copyright holder. Students may inquire about withdrawing their dissertation and/or thesis from this database. For additional inquiries, please contact the repository administrator via email ([scholarship@uwindsor.ca](mailto:scholarship@uwindsor.ca)) or by telephone at 519-253-3000ext. 3208.

# **Sliding Wear of a Squeeze Cast Magnesium Composite**

## **AM60-(Al<sub>2</sub>O<sub>3</sub>)<sub>f</sub> at Low Loads**

By

**Anindya Banerji**

A Thesis  
Submitted to the Faculty of Graduate Studies  
through Engineering Materials  
in Partial Fulfillment of the Requirements for  
the Degree of Master of at the University of Windsor

Windsor, Ontario, Canada

2012

©2012 Anindya Banerji

**Sliding Wear of a Squeeze Cast Magnesium Composite AM60-(Al<sub>2</sub>O<sub>3</sub>)<sub>f</sub>  
at Low Loads**

By  
**Anindya Banerji**

APPROVED BY:

---

A.T. Alpas, Co-Advisor  
Department of Mechanical, Automotive & Materials Engineering

---

H. Hu, Co-Advisor  
Department of Mechanical, Automotive & Materials Engineering

---

A.R. Riahi, Program Reader  
Department of Mechanical, Automotive & Materials Engineering

---

D. Ting, Outside Program Reader  
Department of Mechanical, Automotive & Materials Engineering

---

Dr. R. Bowers, Chair of Defense  
Department of Mechanical, Automotive & Materials Engineering

## **DECLARATION OF ORIGINALITY**

I hereby certify that I am the sole author of this thesis and that no part of this thesis has been published or submitted for publication.

I certify that, to the best of my knowledge, my thesis does not infringe upon anyone's copyright nor violate any proprietary rights and that any ideas, techniques, quotations, or any other material from the work of other people included in my thesis, published or otherwise, are fully acknowledged in accordance with the standard referencing practices. Furthermore, to the extent that I have included copyrighted material that surpasses the bounds of fair dealing within the meaning of the Canada Copyright Act, I certify that I have obtained a written permission from the copyright owner(s) to include such material(s) in my thesis and have included copies of such copyright clearances to my appendix.

I declare that this is a true copy of my thesis, including any final revisions, as approved by my thesis committee and the Graduate Studies office, and that this thesis has not been submitted for a higher degree to any other University or Institution.

## ABSTRACT

Mg matrix composites AM60-x% ( $\text{Al}_2\text{O}_3$ )<sub>f</sub> (x=9,11,26) were fabricated by  $\text{Al}_2\text{O}_3$  fibre preform preparation and squeeze casting technique. Sliding wear behaviour of these composites were studied by conducting boundary lubricated pin-on-disk tests under ultra-mild wear conditions at 25 °C and 100 °C against AISI 52100 steel balls. The damage in AM60-9% ( $\text{Al}_2\text{O}_3$ )<sub>f</sub> at 25 °C occurred as follows:  $\text{Al}_2\text{O}_3$  fibre fracture and fragmentation, sinking in of the fragmented fibres leading to decrease in fibre elevation, and damage to Mg matrix. The fibre fracture and fragmentation process, leading towards damage to the Mg matrix, was attributed to: i) high applied contact pressure, ii) matrix hardening and, iii) high fibre length.

Increasing the  $\text{Al}_2\text{O}_3$  fibre volume content delayed the transition to higher rate of material loss but inflicted greater damage to the counterface. At 100 °C, the formation of an oil residue layer on the worn surfaces delayed the wear transition.

DEDICATION

*To my parents,*

*Srikumar and Anulekha Banerjee*

*for their love, encouragement and support throughout.*

## **ACKNOWLEDGEMENTS**

My sincerest thanks and gratitude to Dr. A. T. Alpas for his supervision, valuable suggestions and support that guided me throughout this research for my M.A.Sc. at the University of Windsor, and to Dr. H.Hu for his valuable advice, constant help and encouragement during the course of this research.

Sincere thanks to my committee members, Dr. A.R.Riahi, and Dr. D.Ting, for their helpful suggestions. Dr. X. Meng-Burany's contribution to discussions on TEM analyses is greatly appreciated. Sincere thanks to Dr. M. Chen for solving the Greenwood-Tripp contact stress equations. Technical help from Mr. A. Jenner and help in casting from Mr.Xuezhi Zhang are greatly acknowledged.

I appreciate all researchers of the NSERC/General Motors of Canada/University of Windsor Industrial Research Chair in Tribology of Lightweight Materials, for their help, cooperation, constant support and encouragement.

Sincere thanks to the Natural Sciences and Engineering Research Council of Canada (NSERC) and General Motors of Canada Ltd. for their financial support.

## Table of Contents

<b>DECLARATION OF ORIGINALITY</b> .....	iii
<b>ABSTRACT</b> .....	iv
<b>DEDICATION</b> .....	v
<b>ACKNOWLEDGEMENTS</b> .....	vi
<b>LIST OF FIGURES</b> .....	ix
<b>LIST OF TABLES</b> .....	xv
<b>Chapter 1: Introduction</b> .....	1
1.1. Background of this work	1
1.2. Objectives of current research	2
1.3. Scope of this work	3
1.4. Organization of this Thesis	3
<b>Chapter 2: Literature Survey</b> .....	6
2.1. Introduction to this survey	6
2.2. Wear stabilization under dry sliding conditions	6
2.2.1. Wear of Al-Si and Mg-Al alloys	6
2.2.2. Al and Mg metal matrix composites	19
2.2.2.1. Strengthening mechanisms in metal matrix composites	19
2.2.2.2. Wear of Al and Mg matrix composites	31
2.3. Wear stabilization under lubricated sliding conditions	39
2.4. Summary	58
<b>Chapter 3: Experimental Methodology</b> .....	59
3.1. Introduction	59
3.2. Description and fabrication of Mg matrix composites	59
3.3. Sliding wear tests	68
3.4. Observation of worn surfaces	69
<b>Chapter 4: Results</b> .....	76



4.1. Introduction	76
4.2. Wear of unreinforced alloy AM60	76
4.3. Comparison of wear of AM60-(9% (Al <sub>2</sub> O <sub>3</sub> ) <sub>f</sub> + 4% (Al <sub>2</sub> O <sub>3</sub> ) <sub>p</sub> ) and AM60-9% (Al <sub>2</sub> O <sub>3</sub> ) <sub>f</sub>	83
4.4. Wear of Mg composites reinforced with different volume percentages of Al <sub>2</sub> O <sub>3</sub> fibres	89
4.5. Wear of composite; AM60-9% (Al <sub>2</sub> O <sub>3</sub> ) <sub>f</sub> at 25 °C and 100 °C	94
4.5.1. Decrease in height of Al <sub>2</sub> O <sub>3</sub> fibres at at 25 °C and 100 °C	94
4.5.2. Comparison of damage features of AM60-9% (Al <sub>2</sub> O <sub>3</sub> ) <sub>f</sub> at 25 °C and 100 °C	94
4.6. Damage to the counterface AISI 52100	110
<b>Chapter 5: Discussion</b> .....	115
5.1. Introduction	115
5.2. Contact pressure analysis	116
5.3. Effect of matrix hardness	126
5.4. Effect of Al <sub>2</sub> O <sub>3</sub> fibre morphology	129
5.4.1 Critical fibre length under normal force	129
5.4.2. Critical fibre aspect ratio during shear force	135
5.5. Damage events	139
5.6. Comparison with Al-Si alloys and role of oil residue layer	144
<b>Chapter 6: Summary and Conclusions</b> .....	151
6.1 Summary	151
6.2 Conclusions	153
6.3 Future work	156
<b>REFERENCES</b> .....	157
<b>VITA AUCTORIS</b> .....	164

## List of Figures

Fig.2.1. Wear mechanism map for 6061 Al alloy [21].	12
Fig.2.2. Variation of friction and wear rate with humidity content in air [22].	13
Fig.2.3. Plot of variation of wear rate vs. load for A390 in air and argon and against AISI 52100 and DLC [23].	14
Fig.2.4. Plot of wear rate as a function of load. At low loads ( $\leq 20$ N) wear rate decreased with increasing Si percentage whereas at higher loads ( $\geq 25$ N) the Al-20 Si showed superior wear resistance [26].	15
Fig.2.5. Wear rates of A390, 383 and Al-25 Si showing the presence of two subregimes of mild wear-MW-1 AND MW-2 [27].	16
Fig.2.6. Schematic representation of processes leading to the formation of metallic aluminum layer (for A390) within tribolayers in MW-2. (a) Tribolayer supporting the load; (b) Removal of tribolayer exposing Al to counterface; (c) Extrusion of Al accompanied by metal transfer and back transfer processes [28].	17
Fig.2.7. (a) Wear rate map for AZ91 in dry sliding wear. Each point on the map represents a wear rate measurement made at a given set of load and sliding speed. The continuous line represents the boundary between the mild and severe wear. The transitions between the sub-regimes are marked by dashed lines; (b) wear transition map for AZ91 showing the region of dominance of wear mechanisms and the transition boundaries between them: BB: mild wear to severe wear transition; AA [29].	18
Fig. 2.8. Schematic diagram showing the particle-matrix interaction in the AZ91/SiC composite [33].	26
Fig. 2.9. Optical micrographs of (a) unreinforced AZ91 alloy and (b) AZ91/SiC composite [33].	27
Fig.2.10. Average grain size for unreinforced AZ91 and AZ91/SiC composite [33].	28
Fig.2.11. Stress-strain curves for (a) Mg-8Li (f) composites and (b) Mg-8Li (p) composites at various temperatures [39].	29
Fig.2.12. Variation of stress along a fibre in a fibre reinforced composite [38].	30
Fig.2.13. (a) Backscattered SEM image of cross-section of A356 Al-10% SiC-4% Gr worn at 159 N and 2.0 m/s; (b) Schematic representation of constituents of tribolayer in graphitic metal matrix composite [46].	36
Fig.2.14. Secondary SEM micrographs showing the subsurface microstructures of A390 at 10 N in: (a) air and (b) argon indicating the difference in the composition of the tribolayer formed under different experimental medium [23].	37

Fig.2.15. Diagram illustrating the conditions and approximate boundaries of dominance of the five wear mechanisms identified in the present study [54]. .....	38
Fig.2.16. Cross-sectional TEM micrograph obtained from: (a) worn subsurface of Al-11% Si tested under laboratory conditions [11] and (b) worn Al-11% Si cylinder bore [64]. It is to be noted that both the microstructures show similar features and the presence of protective oil residue layer. ....	47
Fig.2.17. (a) and (b) represents SEM and optical profilometry images of Al-18.5% Si indicating scratches on Si particles with no damage to the matrix; (c) and (d) represents SEM and optical profilometry images of Al-11% Si showing matrix damage [60]......	48
Fig.2.18. Volumetric wear loss of Al-18.5% Si at 5.0 N load. The wear loss is measurable after $5 \times 10^4$ sliding cycles [63]......	49
Fig.2.19. Cross-sectional TEM image of the microstructure of the material under the wear track showing ultra-fine aluminum grains around the silicon particle and the oil residue layer [11]......	50
Fig.2.20. Variation of volumetric wear with sliding cycles in Al-11% Si in comparison with Al-25% Si indicating the three stages of UMW [11]......	51
Fig.2.21. Schematic representation of deformation microstructures and grain subdivision process. (a) Small to medium strain deformation showing long microbands and dense dislocation walls surrounding groups of cells in cell blocks; (b) at large strain deformation, with lamellar boundaries parallel to the deformation direction, sandwiching in narrow slabs of cells or equiaxed subgrains [65]......	52
Fig.2.22. The Stribeck curve showing three lubricated regimes: boundary lubrication, mixed lubricated and hydrodynamic lubrication. Z=lubricant viscosity; N=sliding speed; P=applied load [77]......	53
Fig.2.23 Structure of zinc dithiophosphate. The 'R' group indicates whether it's an alkyl or an aromatic dithiophosphate [78]. .....	54
Fig.2.24. Infrared spectra for (a) tribologically derived ZDDP antiwear film; (b) a simulated spectrum of tribochemical film; (c) amorphous calcium pyrophosphate and (d) amorphous magnesium orthophosphate [79]......	55
Fig.2.25. P L-edge spectra of ZDDP films generated under different rubbing times measured using (a) TEY and (b) FY modes. Differences in the polyphosphate chain-length can be observed between the surface (TEY) and the bulk (FY) of the film by comparing the a/c peak heights [72]. .....	56
Fig.2.26. XANES spectra of model compounds and antiwear films formed on different Al-Si and steel couples. (a) P L-edge XANES spectra; (b) P K-edge XANES spectra [78].	57
Fig.3.1. Al <sub>2</sub> O <sub>3</sub> fibre preform after compression and drying. ....	62

Fig.3.2.(a) The squeeze casting machine and (b) the furnace. The dies are closed by raising the lower die against the upper one by the hydraulic press. The magnesium alloy AM60 was melt at 750 °C in the furnace (b), and poured into the die. ....	63
Fig.3.3. Flow diagram of the squeeze casting technique. ....	64
Fig.3.4. Secondary scanning electron micrograph showing the initial microstructures of (a) AM60-9% (Al <sub>2</sub> O <sub>3</sub> ) <sub>f</sub> ; (b) AM60-11% (Al <sub>2</sub> O <sub>3</sub> ) <sub>f</sub> ; (c) AM60-26% (Al <sub>2</sub> O <sub>3</sub> ) <sub>f</sub> . ....	65
Fig.3.5. Al <sub>2</sub> O <sub>3</sub> fibre length and width distribution in AM60-9% (Al <sub>2</sub> O <sub>3</sub> ) <sub>f</sub> . ....	67
Fig.3.6. Pin-on-disk tribometer used to conduct lubricated sliding wear tests on Mg composites. ....	71
Fig.3.7. (a) Optical profilometry image used to calculate the worn area. (b) 2D-profile plot obtained from the marked X-X' region of image (a). ....	73
Fig.3.8. Histogram representing the decrease in the Al <sub>2</sub> O <sub>3</sub> fibre height from the initial surface after 2×10 <sup>5</sup> sliding cycles. The horizontal distance between the two peaks is the Al <sub>2</sub> O <sub>3</sub> fibre elevation. ....	75
Fig.4.1. SEM micrographs (secondary electron mode) of worn AM60 alloy tested at 1.0 N load. (a) wear grooves observed at 7.5×10 <sup>4</sup> sliding cycles; (b) worn surface oxidation at 4.0×10 <sup>5</sup> sliding cycles; (c) MgO debris particles. ....	78
Fig.4.2. SEM micrograph of counterface AISI 52100 worn against AM60 matrix alloy, at 1.0 N load and for 4×10 <sup>5</sup> cycles, indicating the presence of MgO debris particles transferred from the worn composite surface and carbon (C) from the lubricating oil. This serves as evidence that at higher sliding cycles (≥2×10 <sup>5</sup> cycles) oxidation and adhesion type wear occurred. ....	79
Fig.4.3. Volumetric wear loss vs. sliding cycles plot for AM60 alloy at 1.0 N load indicating presence of two wear regimes: wear by surface plastic deformation and wear by oxidation and adhesion. ....	80
Fig.4.4. SEM micrographs showing the difference in the width of wear tracks of (a) AM60 alloy at 1.0 N and 2.5×10 <sup>4</sup> cycles and (b) AM60-9% (Al <sub>2</sub> O <sub>3</sub> ) <sub>f</sub> at 2.0 N and 6×10 <sup>5</sup> cycles indicating the wear resistance of the ceramic reinforced composite is higher than the alloy. ....	81
Fig.4.5. Volumetric wear loss vs. sliding cycles plot for AM60 alloy and AM60-9% (Al <sub>2</sub> O <sub>3</sub> ) <sub>f</sub> . The wear loss of the composite is 10 <sup>2</sup> times lower than that of the matrix alloy. Note the wear of the composite was shown at 5.0 N and the matrix at 1.0 N load in order to emphasize the higher wear resistance of the composite AM60-9% (Al <sub>2</sub> O <sub>3</sub> ) <sub>f</sub> compared to AM60 alloy. ....	82
Fig.4.6. a) SEM micrograph at 500X magnification showing the morphology of worn surface AM60-9% (Al <sub>2</sub> O <sub>3</sub> ) <sub>f</sub> after 1.0×10 <sup>5</sup> cycles indicating presence of wear grooves; b)	

SEM micrograph at 1000X magnification showing morphology of worn surface of AM60-(9% (Al<sub>2</sub>O<sub>3</sub>)<sub>f</sub> + 4% (Al<sub>2</sub>O<sub>3</sub>)<sub>p</sub>) after 1.0×10<sup>5</sup>cycles indicating no damage to Mg matrix. ....85

Fig.4.7. (a) and (b) represent histogram plot for AM60-(9% (Al<sub>2</sub>O<sub>3</sub>)<sub>f</sub> + 4% (Al<sub>2</sub>O<sub>3</sub>)<sub>p</sub>) and AM60-9% (Al<sub>2</sub>O<sub>3</sub>)<sub>f</sub> respectively under etched conditions with an initial elevation of Al<sub>2</sub>O<sub>3</sub> by 2.8±0.20 μm, obtained from optical profilometry measurements. It is shown that after 1.0×10<sup>5</sup> sliding cycles the Al<sub>2</sub>O<sub>3</sub> fibres+particles (f+p) were exposed by 1.8±0.22 μm for AM60-(9% (Al<sub>2</sub>O<sub>3</sub>)<sub>f</sub> + 4% (Al<sub>2</sub>O<sub>3</sub>)<sub>p</sub>) while the Al<sub>2</sub>O<sub>3</sub> fibres were at the same elevation as that of the Mg matrix for AM60-9% (Al<sub>2</sub>O<sub>3</sub>)<sub>f</sub>. (c) is the plot of fibre height decrease against number of sliding cycles at 5.0 N load. ....87

Fig.4.8. Plot of volumetric wear of AM60-9% (Al<sub>2</sub>O<sub>3</sub>)<sub>f</sub> and AM60-(9% (Al<sub>2</sub>O<sub>3</sub>)<sub>f</sub> + 4% (Al<sub>2</sub>O<sub>3</sub>)<sub>p</sub>) with increasing sliding cycles. In case of AM60-9% (Al<sub>2</sub>O<sub>3</sub>)<sub>f</sub> it is evident that at 2.0 N load the transition to higher volumetric wear loss occurs at 2.0×10<sup>5</sup> sliding cycles while at 5.0 N load it occurs after 1.0×10<sup>5</sup> cycles. However, for AM60-(9% (Al<sub>2</sub>O<sub>3</sub>)<sub>f</sub> + 4% (Al<sub>2</sub>O<sub>3</sub>)<sub>p</sub>) zero volumetric wear loss is observed after 1.0×10<sup>5</sup> cycles at 1.0 N load indicating higher wear resistance compared to AM60-9% (Al<sub>2</sub>O<sub>3</sub>)<sub>f</sub>.....88

Fig.4.9. SEM micrographs in secondary electron mode illustrating the worn surfaces at 2.0 N and after 1×10<sup>6</sup> cycles of (a) AM60-9% (Al<sub>2</sub>O<sub>3</sub>)<sub>f</sub> indicating fibre fracture and extensive plastic deformation of Mg matrix; (b) AM60-11% (Al<sub>2</sub>O<sub>3</sub>)<sub>f</sub> indicating damage in the form of wear grooves; (c) AM60-26% (Al<sub>2</sub>O<sub>3</sub>)<sub>f</sub> showing almost no damage to matrix. ....91

Fig. 4.10. Volumetric material loss vs. sliding cycles at 2.0 N load indicating the effect of Al<sub>2</sub>O<sub>3</sub> fibre volume percentage on the transition to higher rate of material removal of the composite. It is to be noted that the transition to higher volumetric wear loss was delayed to 1×10<sup>6</sup> cycles for AM60-26% (Al<sub>2</sub>O<sub>3</sub>)<sub>f</sub> as opposed to 6×10<sup>5</sup> cycles for AM60-9% (Al<sub>2</sub>O<sub>3</sub>)<sub>f</sub> and AM60-11% (Al<sub>2</sub>O<sub>3</sub>)<sub>f</sub>. ....92

Fig.4.11. Plot of variation of Al<sub>2</sub>O<sub>3</sub> fibre height with sliding cycles at 1.0 N, 2.0 N and 5.0 N for AM60-9% (Al<sub>2</sub>O<sub>3</sub>)<sub>f</sub> composite at 25 °C. The fiber height reduction was delayed with decreasing load. ....98

Fig.4.12. Plot of variation of Al<sub>2</sub>O<sub>3</sub> fibre height with sliding cycles at 25 °C and 100 °C under 2.0 N load for AM60-9% (Al<sub>2</sub>O<sub>3</sub>)<sub>f</sub> composite. The fiber height reduction is less in case of elevated temperature tests. ....99

Fig.4.13. SEM micrographs of AM60-9% (Al<sub>2</sub>O<sub>3</sub>)<sub>f</sub> at room temperature and at 1.0 N, 2.0 N and 5.0 N. (a) No damage to matrix after 8.0×10<sup>5</sup> cycles under 1.0 N load; (b) High magnification image at 1.0 N load and 8.0×10<sup>5</sup> cycles indicating: i) fibre fracture and fragmentation ii) sinking in of the fragmented fibres iii) pile up of the adjacent Mg matrix without any damage to matrix; (c) Damage to the matrix in the form of wear grooves along with deformation of the Mg matrix at 2.0 N and after 8.0×10<sup>5</sup> cycles; (d) Damage to Mg matrix in the form of wear grooves as early as 1×10<sup>5</sup> cycles at 5.0 N load. ....101

Fig.4.14. Volumetric wear loss vs. sliding cycles plot of AM60-9% (Al<sub>2</sub>O<sub>3</sub>)<sub>f</sub> at 1.0 N, 2.0 N and 5.0 N load at 25 °C. The transition to higher volumetric wear loss was delayed as the applied load was reduced- at 5.0 N the transition occurred at 1×10<sup>5</sup> cycles, at 2.0 N the transition occurred at 6×10<sup>5</sup> cycles while at 1.0 N zero volumetric wear continued for the highest sliding cycles tested 1×10<sup>6</sup> cycles. In the initial cycles fiber fracture preceded sinking in with no damage to the matrix. At higher sliding cycles damage to the Mg matrix by the counterface was observed.....102

Fig.4.15. SEM micrographs (secondary electron mode) of worn surface of AM60-9% (Al<sub>2</sub>O<sub>3</sub>)<sub>f</sub> at 2.0 N load. (a) and (b) represents worn surfaces after 2×10<sup>5</sup> cycles showing damage features including fibre fragmentation, sink in and Mg matrix pile up- without damage to matrix. (c) represents worn surface after 6×10<sup>5</sup> cycles indicating damage to the matrix in form of plastic deformation.....104

Fig.4.16. Plot of fibre height decrease and volumetric wear loss at 2.0 N load with increasing sliding cycles. After 6×10<sup>5</sup> cycles, the Al<sub>2</sub>O<sub>3</sub> fibre height decreased to 0.50±0.02 μm which corresponds to the increase in volumetric wear loss from 0.00-0.38 (×10<sup>-3</sup>) mm<sup>3</sup>. Thus damage to Mg matrix can be predicted by quantifying the fibre height decrease.....105

Fig.4.17. Back-scattered SEM micrographs of worn AM60-9% (Al<sub>2</sub>O<sub>3</sub>)<sub>f</sub> at 100 °C. (a) Tribofilm formation on top of Al<sub>2</sub>O<sub>3</sub> fibre at 1.0 N load after 1.0×10<sup>6</sup> cycles; (b) EDS analysis revealed that the tribofilm consisted of Zn, S, Ca and P; (c) Formation of tribofilm on top of Al<sub>2</sub>O<sub>3</sub> fibre and on the Mg matrix at 2.0 N load after 1.0×10<sup>6</sup> cycles.107

Fig.4.18. Comparison of volumetric wear loss vs. sliding cycles plot of AM60-9% (Al<sub>2</sub>O<sub>3</sub>)<sub>f</sub> at 100 °C and at 25 °C under 2.0 N load. The plot indicates that under the same conditions the wear rate was lower in case of tests conducted at 100 °C than at 25 °C. The transition to higher volumetric wear loss occurred after 6×10<sup>5</sup> cycles at 25 °C while at 100 °C the transition is postponed till after 8×10<sup>5</sup> cycles.....108

Fig.4.19. Back-scattered SEM micrographs of worn AM60-9% (Al<sub>2</sub>O<sub>3</sub>)<sub>f</sub> and 2.0 N load at (a) 100 °C and (b) 25 °C. For tests conducted at 2.0 N load and 100 °C formation of the oil residue layer could be detected whereas at 25 °C the oil residue layer was not found.109

Fig.4.20. SEM image of the wear track on the counterface worn against AM60-9% (Al<sub>2</sub>O<sub>3</sub>)<sub>f</sub> at 25 °C, after 1×10<sup>6</sup> cycles, showing damage in the form of wear grooves....111

Fig.4.21. Plot of volumetric wear loss from the counterface against AM60-9% (Al<sub>2</sub>O<sub>3</sub>)<sub>f</sub> and Al-18.5% Si alloy at 5.0 N load. AM60-9% (Al<sub>2</sub>O<sub>3</sub>)<sub>f</sub> causes greater damage to the counterface than Al-18.5% Si alloy.....112

Fig.4.22. SEM micrograph and EDS result of the wear track on the counterface worn against AM60-9% (Al<sub>2</sub>O<sub>3</sub>)<sub>f</sub> at 100 °C and after 1×10<sup>6</sup> cycles. Presence of Zn, P, S and Ca on the worn counterface surface indicates formation of an oil residue layer on the counterface.....113

Fig.5.1. Histogram of the initial surface of AM60-9%  $(Al_2O_3)_f$  under unetched conditions with 3 other curves fitted to the Mg peak,  $Al_2O_3$  fibre peak and summation of all the curve fittings respectively. ....119

Fig.5.2. (a) The calculated G-T contact pressure distribution on the  $Al_2O_3$  fibres for AM60-9%  $(Al_2O_3)_f$  at 5.0 N and 1.0 N load. The Hertzian pressure distribution is also shown. (b) Plot of G-T stress with increasing load and (c) Optical profilometry image, at 5.0 N load and after  $1 \times 10^6$  cycles, indicating maximum damage at the centre of the wear track and the width of wear track ( $260 \pm 15.5 \mu m$ ) approximately equal to the width of wear track predicted by plot (a). ....126

Fig.5.3. Representative fibre orientations (a) parallel and (b) perpendicular to the direction of applied normal load in the Mg composites. The model developed in section 5.4.1 considers only (a) where the fibre is parallel to the direction of loading. ....132

Fig.5.4. Correlation plot between number of fragments observed for an initial length L obtained from experimental observations and the values predicted from Eqn.5.25. ....134

Fig.5.5. SEM micrographs indicating difference in damage features after single pass sliding contact tests performed at constant loads of (a) 0.05 N and (b) 0.07 N. ....137

Fig.5.6. Plot of matrix hardness and volumetric wear loss after  $6 \times 10^5$  cycles at 2.0 N load for AM60-9%  $(Al_2O_3)_f$ , AM60-11%  $(Al_2O_3)_f$  and AM60-26%  $(Al_2O_3)_f$ . The extent of wear resistance expected due to the high matrix hardness of AM60-26%  $(Al_2O_3)_f$  is not observed. ....141

Fig.5.7. Plot of matrix hardness, volumetric wear loss (after  $6 \times 10^5$  cycles) and change in aspect ratio for AM60-9%  $(Al_2O_3)_f$ , AM60-11%  $(Al_2O_3)_f$  and AM60-26%  $(Al_2O_3)_f$  after  $6 \times 10^5$  cycles at 2.0 N load. The low wear resistance of AM60-26%  $(Al_2O_3)_f$  might be explained by highest change in aspect ratio due to fracture and fragmentation. ....142

Fig.5.8. Plot of decrease of  $Al_2O_3$  fibre length and fibre height with sliding cycles for AM60-9%  $(Al_2O_3)_f$  at 2.0 N load indicating the predominance of fracture and fragmentation in the initial sliding cycles; sinking in of the fragmented fibres is observed at higher sliding cycles; 'h' represents the  $Al_2O_3$  fibre elevation. ....143

Fig.5.9. Comparison of Greenwood-Tripp plot for AM60-9%  $(Al_2O_3)_f$  and Al-18.5% Si at 5.0 N load (25 °C) indicating the considerably higher applied contact pressure for the Mg composite compared AM60-9%  $(Al_2O_3)_f$  to Al-18.5% Si under the same conditions. ...146

Fig.5.10. Comparison of the maximum G-T contact pressure and the corresponding volumetric wear loss at 5.0 N load and  $2 \times 10^5$  sliding cycles. AM60-9%  $(Al_2O_3)_f$  shows a higher rate of material loss due to the higher maximum contact pressure on it compared to the Al-18.5% Si alloy. ....147

Fig.5.11. Comparison of the volumetric wear loss vs. sliding cycles (at 25 °C) plot for eutectic and hypereutectic Al-Si alloys with the Mg composites. It is to be noted that

wear stabilization is observed in the case of Al-11% Si alloy due to the formation of the oil residue layer. ....	148
Fig.5.12. Cross-sectional TEM image of the microstructure of the subsurface material under the wear track, tested at 1.0 N load and 100 °C, showing formation of oil residue layer on top of Al <sub>2</sub> O <sub>3</sub> fibres. Corresponding EDS analysis of the oil residue layer show the constituent elements of the oil residue layer to be Zn, P, S, Ca and C. ....	149
Fig.5.13. Cross-sectional TEM micrograph of the subsurface material under the wear track, tested at 100 °C and 2.0 N load, showing formation of continuous oil residue layer on the worn Mg matrix. Immediately below the layer presence of Mg nano-grains were detected. ....	150
Fig.6.1. Plot of variation of volumetric wear loss with change in Al <sub>2</sub> O <sub>3</sub> fibre volume percentage and operating temperature. Increasing the fibre volume percentage from 9% (AM60-9% (Al <sub>2</sub> O <sub>3</sub> ) <sub>f</sub> ) to 26% (AM60-26% (Al <sub>2</sub> O <sub>3</sub> ) <sub>f</sub> ) decreased the volumetric wear loss ( $0.379 \times 10^{-3} \text{ mm}^3 - 0.14 \times 10^{-3} \text{ mm}^3$ ) but increased the damage to the counterface. At 100 °C AM60-9% (Al <sub>2</sub> O <sub>3</sub> ) <sub>f</sub> showed comparable wear resistance to that of AM60-26% (Al <sub>2</sub> O <sub>3</sub> ) <sub>f</sub> proving to be the optimum operating condition. ....	155

### List of Tables

Table 2-1. Tensile properties of AZ91 alloy and AZ91/SiC composite. [33,36] .....	25
Table 3-1: Determination of preform volume percentage. ....	62
Table 3-2: Indentation hardness values AM60 alloy and fibre reinforced Mg composites. ....	66
Table 3-3: Parameters for calculation of lubrication conditions. ....	72
Table 3-4: The average volumetric wear loss calculated from the individual worn area loss calculated from different portions of the wear track. ....	74
Table 4-1: Al <sub>2</sub> O <sub>3</sub> fibre elevation over the Mg matrix for the composites after $6 \times 10^5$ sliding cycles. ....	93
Table 4-2: Volume of material lost from AISI 52100 counterface and Mg matrix composites after $1 \times 10^6$ sliding cycles. ....	114
Table 5-1. Parameters used to calculate the composite elastic modulus E*. ....	117
Table 5-2. Parameters used to calculate the Hertzian pressure distribution. ....	118
Table 5-3. Parameters used to calculate the Greenwood-Tripp contact pressure on Al <sub>2</sub> O <sub>3</sub> fibres. ....	124



Table 5-4. Parameters used to calculate the increase in dislocation density in Mg composites AM60-9% (Al <sub>2</sub> O <sub>3</sub> ) <sub>f</sub> , AM60-11% (Al <sub>2</sub> O <sub>3</sub> ) <sub>f</sub> and AM60-26% (Al <sub>2</sub> O <sub>3</sub> ) <sub>f</sub> .....	128
Table 5-5. Comparison of calculated values of hardness with experimentally measured microindentation hardness results.....	129
Table 5-6. Calculation of average critical length of fragmented fibre.....	133
Table 5-7. Calculation of critical fibre aspect ratio. Fibres are expected to fracture when $(t/l) < (t/l)_c$ .....	138

# Chapter 1: Introduction

## 1.1. Background of this work

Ever-increasing fuel prices and concern about pollution from automobile emissions have increased attention to automotive fuel economy and ways to mitigate its effect on climatic changes, air pollution and related health hazards [1,2]. Technologies geared toward improving fuel economy and reducing emissions require research on strategies for manufacturing lighter-weight vehicles. Among the various mass-reduction modes adopted by the automotive industries, replacement of the materials used in the construction for powertrain components with materials possessing low strength-to-weight ratio promises to be the most effective.

Frictional interaction between the cylinder block, the piston skirt and the piston ring forms a major part (48%) of the total engine friction [3,4]. Cylinder blocks have traditionally been made of gray cast iron. However, the need for increased fuel economy, combined with environmental regulations, has resulted in the use of cast aluminum as an alternative. One of the earliest cast aluminum alloys possessing sufficient wear resistance was Al-18.5% Si (A390), which has been used for monolithic cylinder blocks [5]. The surface of the alloy was etched before use in order to expose the second phase Si particles, which acted as load-bearing elements. However, the high Si content also posed problems during machining of the alloy. Thus it is important to study the wear behaviour of lightweight materials intended for use as engine components.

The motivation to further reduce mass in automobiles has led to extensive study of Magnesium (Mg) alloys and composites, as they possess better strength-to-weight ratios than Aluminum (Al) or Iron (Fe). Magnesium, the eighth most common element, is

produced through either the metallothermic reduction of magnesium oxide with silicon or the electrolysis of magnesium chloride melts from seawater. Each cubic metre of seawater contains approximately 1.3 kg (0.3%) magnesium. Mg Studies [2,6] have shown that use of a Mg engine block in place of cast iron or Al alloy helps achieve 40% and 19% weight reduction, respectively. Apart from being lighter than Al, other factors that make the use of Mg lucrative are its good castability and machinability. Mg composites [7,8] in particular possess superior mechanical properties, such as bulk hardness and yield stress, compared to the Mg alloy.

## **1.2. Objectives of Current Research**

Engine block-piston ring applications require the constituent materials to provide high sustainability over long periods of sliding interactions. The sliding components usually operate under boundary lubrication conditions, in which asperities in metals are in contact with each other [9]. The presence of very thin films derived from the additives used in the lubricants is extremely important for reducing wear on the interacting components. The amount of material removed during the engine-piston sliding interaction is less than that observed in mild or severe wear [10]. The micromechanisms of wear operating in this regime, known as ultra mild wear (UMW), also differ from traditional mild and severe wear [11]. In this study, the lubricated sliding wear of Mg composites against a steel counterface has been investigated.

Thus the objectives of the present research are:

i) to investigate boundary lubricated sliding wear behaviour of Mg composites and the matrix alloy.

ii) to study and compare the wear mechanisms of the Mg composites and the matrix alloy.

iii) to correlate the microstructural features to the wear behaviour of both the tested composite and the matrix alloy.

### **1.3. Scope of this work**

The scope of this work includes the fabrication of Mg (AM60 alloy) matrix composites with a specific range (7-25 vol%) of reinforcement ( $\text{Al}_2\text{O}_3$  fibre) by using preform and squeeze casting techniques; pin-on-disk sliding testing of Mg composites under lubricated conditions; the observation of the worn surfaces and their cross-sections with optical/electron microscopes as well as optical profilometry.

In summary, this research elucidates the prevalent micromechanisms causing damage during the sliding interaction between the Mg matrix composite and a steel counterface. The understanding of wear mechanisms will help in further development of composites suitable for engine bore applications.

### **1.4. Organization of this Thesis**

This thesis consists of five chapters. The contents of this chapter are described below:

**Chapter 1** is the introductory section, starting with the background and followed by the scope and objective of this research, and includes this current section.

**Chapter 2** reviews earlier studies conducted on wear of Al-Si and Mg alloys/composites under dry and lubricated conditions. The first half of the chapter is a discussion of the effects of load, sliding velocity, contact temperature, humidity, and atmosphere on dry sliding behaviour of Al and Mg alloys and composites. The various strengthening

mechanisms of metal matrix composites are also described. In the second half, the chapter subsequently deals with the lubricated sliding wear behaviour of Al-Si alloys, elaborating on the prevalent wear mechanisms, followed by a discussion of the observation techniques of tribolayer formation from ZDDP degradation and the associated mechanisms. Finally, there is a short summary indicating the main findings of the literature survey.

**Chapter 3** describes the squeeze casting method employed to fabricate the Mg composites. Then it describes the various parameters used to perform pin-on-disk sliding wear tests and the corresponding lubrication regime. This chapter also describes the different methods used to observe and quantify the damage process in the Mg composites.

**Chapter 4** discusses the results of the wear tests conducted on the Mg composites. There is a comparison between the wear of the matrix alloy and composite, the particle and fibre reinforced composite, composites with different volume percentages of Al<sub>2</sub>O<sub>3</sub> fibre and finally the improvement in high-temperature wear test resistance.

**Chapter 5** is the discussion and explanation of the wear mechanisms by quantifying the applied contact pressure on the Al<sub>2</sub>O<sub>3</sub> fibres. This was followed by a discussion on the strengthening of Mg composites due to the addition of reinforcement. Subsequently, the effect of Al<sub>2</sub>O<sub>3</sub> fibre morphology on wear behaviour was discussed and a critical fibre length was calculated based on which fibre fracture could be predicted. Finally, the chapter ends with a brief discussion on subsurface microstructure and composition, with special attention to the role of the oil residue layer on the wear of Mg composites.

**Chapter 6** is a summary of the entire research project and presents the conclusions of this work, including future prospects in this field of study.

## Chapter 2: Literature Survey

### 2.1. Introduction to this survey

This chapter is divided into two sections summarizing relevant studies conducted on the dry and lubricated wear properties. The first section is a survey of the work done on dry sliding wear and the effects of various factors on the transition between mild to severe wear and the role of tribolayer formation in the wear stabilization process. This is followed by a description of the strengthening mechanisms in a composite with ceramic reinforcement and the dry sliding wear of Al and Mg composites. The second half of the chapter presents a brief review on the ultra-mild wear mechanisms of eutectic and hypereutectic Al-Si alloys and the wear stabilization in this regime due to formation of a protective oil residue layer. The degradation mechanisms of ZDDP are also discussed.

### 2.2. Wear stabilization under dry sliding conditions

#### 2.2.1. Wear of Al-Si and Mg-Al alloys

Wear is defined [ASTM G40] as “damage to a solid surface, generally involving progressive loss of material due to relative motion between the surfaces and a contacting substance or substances.” When two surfaces in contact slide over one another, one or both of the surfaces will suffer wear. An empirical rule, assuming asperity (high spots) contact only, was given by Archard [12]:

$$Q = \frac{KW}{H} \quad (2.1)$$

where  $Q$ =volume worn per unit distance;  $W$ =normal load;  $K$ =coefficient of wear, a dimensionless quantity;  $H$ =hardness of the softer surface. The value of  $K$ , wear coefficient, is of great importance as it allows the comparison of severity of different wear processes. It must be noted that this equation, though one of the fundamental

equations of wear, predicts a linear relationship between the volume worn away to the applied load, which might not be the case in many instances. Extensive studies have been conducted on dry sliding wear of Fe [13-17] and Al/Al-Si [18-20] alloys wherein the wear mechanisms can be well demarcated into mild and severe wear. In the mild wear regime, the wear rates are low ( $10^{-4}$ - $10^{-3}$  mm<sup>3</sup>/m) and the contact surface, characterized by presence of tribolayers, exhibits less damage as compared to the severe wear regime. The transition from mild to severe wear, characterized by higher wear rates ( $\geq 10^{-2}$  mm<sup>3</sup>/m), occurs during conditions of increased load, velocity and temperature, and features massive surface damage and material transfer to the counterface [21].

Zhang and Alpas [21] have investigated mild and severe wear transitions for Al-Mg-Si alloy (6061 Al) by conducting dry block-on-ring tests against SAE 52100 bearing steel rings at the load range of 1-450 N and sliding velocity 0.1-5.0 m s<sup>-1</sup>. Mild to severe wear transition was found to depend on a combination of load, velocity and surface temperature (induced by sliding distance). The transition load of 230 N at 0.4 m/s reduced to 9.0 N when the sliding speed was increased to 5.0 m/s. The role of contact surface temperature in wear was studied by carefully positioning thermocouple probes on the sliding specimens. It was observed that mild to severe wear transition occurred when the bulk surface temperature ( $T_b$ ) exceeded the critical temperature ( $T_c$ ) of 123°C for this system. This observation enables the prediction of wear transition for Al-alloys sliding against steel from a single bulk temperature measurement. SEM revealed the presence of two types of wear debris, suggesting two different types of wear mechanisms represented in the form of a wear map (Fig.2.1): i) The first wear mechanism is spalling of mechanically mixed layers, where aluminum oxide forms at contact points due to



oxidation of Al, acting as an abrasive. Fe particles transferred from the counterface led to the formation of dark discontinuous compacted layers of mechanically mixed wear particles on the contact surfaces allowing mild wear to continue at a steady state. The wear debris comprised of this mechanically mixed layer. ii) The second wear mechanism is delamination wear: the wear debris at higher loads and velocity, having plate-like morphology, consists of Al (observed by Electron Dispersive X-Ray Spectroscopy (EDS)) detached from the bulk of 6061 Al. The suggested mechanism is delamination wear, where a subsurface crack develops and propagates until a wear fragment becomes detached.

Other factors like humidity, atmosphere and the counterface also affect tribological properties of materials. Yen et al. [22] conducted unlubricated sliding wear tests with a eutectic Al-Si alloy against a cast iron counterface at relative humidity (RH) range 1-95%. It was observed that up to 70% RH mild wear was characterized by the formation of an iron-rich compacted surface layer, while from 70%-95% RH the wear rate decreased two fold due to the formation of an iron oxide-rich surface film, which was facilitated by an increase in moisture content (Fig.2.2). The effects of atmosphere and counterface on this phenomenon were studied by Elmadagli and Alpas [23]. The authors investigated unlubricated wear of an A390 (Al-18.5 wt% Si) alloy against SAE 52100 bearing steel in dry air and an argon atmosphere. It was observed that wear rates in an argon atmosphere were always less than those in dry air (5% RH). EDS results show that worn surfaces in dry air were covered with oxidized tribolayers, whereas no peak for oxygen was identified in the EDS spectrum of tribolayers formed in an argon atmosphere. The authors also performed sliding wear tests with A390 samples in air (5% RH) against

graphitic diamond-like carbon (DLC) coatings over the steel counterface. This coating prevented direct contact between the sample and the counterface, resulting in lower wear rates than those observed in the argon atmosphere (Fig.2.3).

The wear behavior of Al alloys also depends on the alloy hardness, along with weight percent, size, and aspect ratio of second phase particles. Bai and Biswas [24] found that in the range of Al 4-24 wt% Si, although wear resistance improved with addition of Si, no systematic trends in wear resistance of the Al-Si alloy could be formulated with respect to Si content. These findings were contradicted in a study by Clarke and Sarkar [25], where it was reported that up to near eutectic compositions the wear resistance of Al-Si alloys improved with Si content. Furthermore it was indicated that seizure resistance improved as a result of Si addition. Wang et al. [26] investigated the effect of Si content on pin-on-disk dry sliding wear behavior of spray-deposited Al-Si alloys containing 12, 20 and 25% Si against T8 tool steel. The authors observed that at the low load of 8.9 N, wear rates of the alloys decreased with increase in Si percentage, and that oxidative wear prevailed (Fig.2.4). At higher loads, the delamination wear mechanism was dominant and the dependence of wear resistance with silicon percentage was not linear. Thus contradictory views exist regarding the effect of Si content on the wear of Al-Si alloys. A definitive study on the effect of Si particle content on wear resistance was performed by Elmadagli and Alpas [27], who conducted unlubricated block-on-ring tests with as cast 383 (with 9.5 wt.% Si), A390 (with 18.5 wt.% Si), and Al-25Si (with 25 wt.% Si) against SAE 52100 steel. The mild wear regime showed two subregimes: the first mild wear subregime (MW-1) and the second mild wear subregime

(MW-2) (Fig.2.5). The steady state of mild wear regime and the relationship of wear rate (W) to load (L) are represented by the relation:

$$W = CL^n \quad (2.2)$$

where C=wear coefficients comprising of  $C_1$  for MW-1 and  $C_2$  for MW-2 were sensitive to microstructure, while n=wear exponent was independent of it. Pair-wise comparison was made on the basis of the role of each microstructure in wear on the three alloys by keeping the other factors constant. The following information was obtained: i) An increase in Si wt% from 9.5 to 25 wt.% increased transition load by 140%, but had only a minor effect on C; ii) An increase in alloy hardness from 31.6 to 53.5 HRB greatly increased transition load by 400%, but had only a minor effect on C; iii) A 47% decrease in the Si particle aspect ratio reduced wear coefficients  $C_1$  by 27% and  $C_2$  by 31%, with minor increase in transition load; iv) A 93% decrease in Si Particle size reduced  $C_1$  by 35% and  $C_2$  by 58%, while  $L_1$  and  $L_2$  were increased by 71% and 33% respectively, where C is the wear coefficient. These subregimes were also observed in another study [28] as a function of applied loads for wear tests conducted on A390 blocks against 52100 steel rings in dry air (RH 5%). It was observed that the wear rate in MW-2 is greater than that MW-1. Although tribolayer formation, generated by mixing and transfer of material from the counterface to the Al-Si contact surface, was detected in both the subregimes, the transition from MW-1 to MW-2 coincided with an increase in the amount of material transferred to the counterface. The high wear rate observed in MW-2 suggests that the aluminum matrix came in contact with the counterface through the fractured portions of the tribolayer in MW-2. The presence of Al layers on the tribolayer was observed in the MW-2. Both Spallation of the thick tribolayers formed in MW-2, which

cause transfer and back-transfer of the aluminum from the counterface (Fig.2.6), along with the extrusion of the exposed aluminum surface over the tribolayers caused the increased wear rate in MW-2 as compared to MW-1.

Similar studies of dry sliding wear were conducted on Mg-Al alloys. Chen and Alpas [29] conducted unlubricated block-on-ring tests on a Mg-9Al-0.9Zn (AZ91) alloy and presented a wear map where the volumetric wear rates were plotted as a function of load and sliding velocity. The authors classified sliding wear of an AZ91 alloy into two main wear regimes, mild wear and severe wear. In the mild wear regime, wear progressed under steady-state wear rate conditions with the two predominant wear mechanisms being oxidational wear, which is characterized by MgO debris formation, and delamination wear, characterized by material transfer from the alloy to the steel counterface. In the severe wear regime, wear rates increased continuously with the sliding distance. The severe wear regime was also subdivided into two wear regimes: plastic deformation-induced wear and melt wear. The wear mechanisms were summarised in a wear mechanism map (Fig.2.7), which helps predict the load and sliding velocity marking the wear transitions. Aung et al. [30] studied the dry sliding wear of AZ91 alloy at constant load of 10 N and varying sliding distances. The authors reported similar wear mechanisms of oxidational and delamination wear. An et al. [31] reported studies of dry sliding wear tests conducted on as-cast magnesium alloys  $Mg_{97}Zn_1Y_2$  and AZ91 using a pin-on-disc configuration, where the authors detected five prevalent wear mechanisms: abrasion, oxidation, delamination, thermal softening and melting.

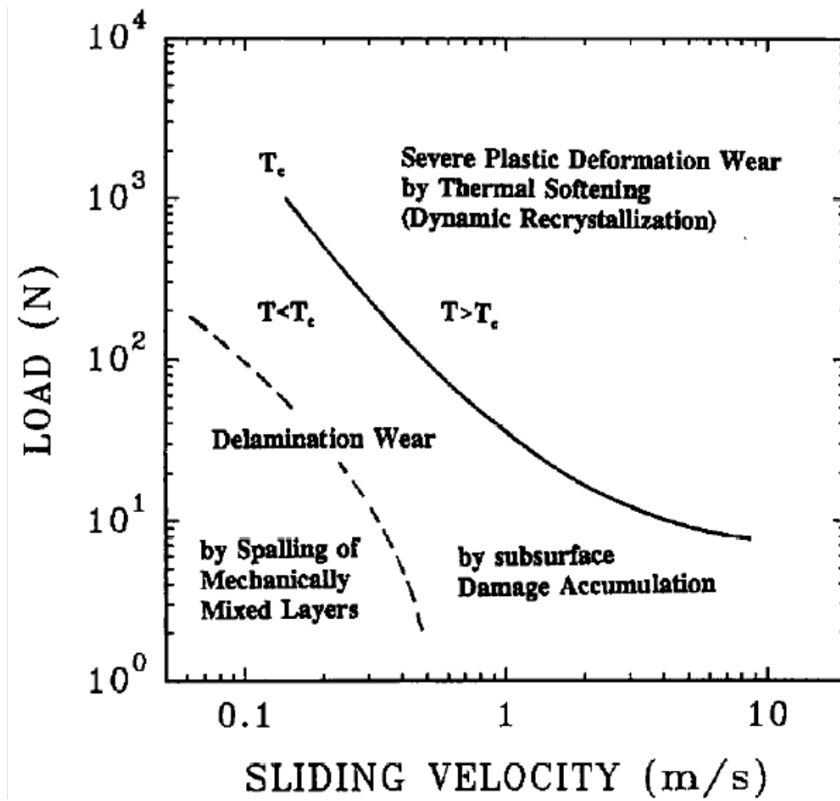


Fig.2.1. Wear mechanism map for 6061 Al alloy [21].

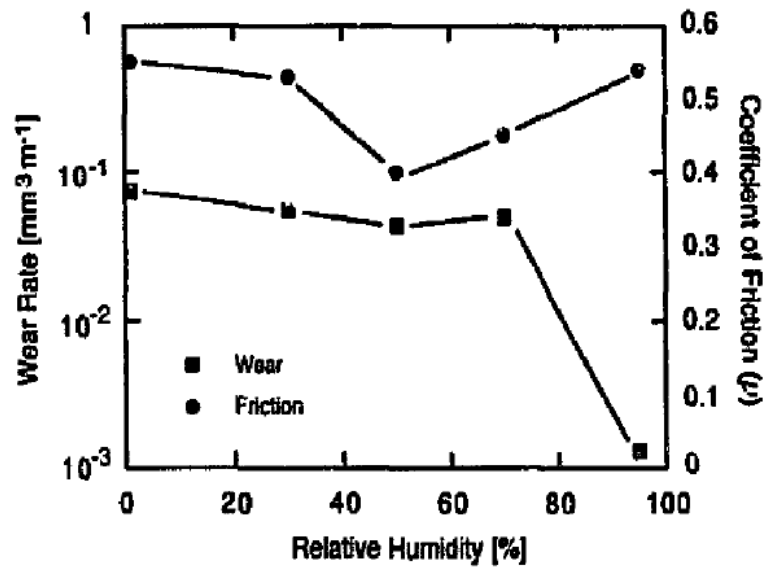


Fig.2.2. Variation of friction and wear rate with humidity content in air [22].

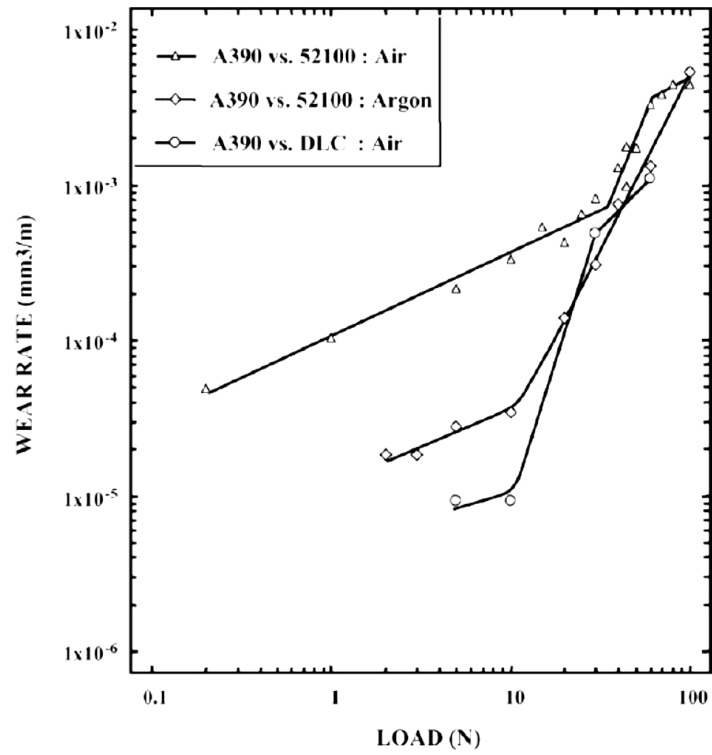


Fig.2.3. Plot of variation of wear rate vs. load for A390 in air and argon and against AISI 52100 and DLC [23].

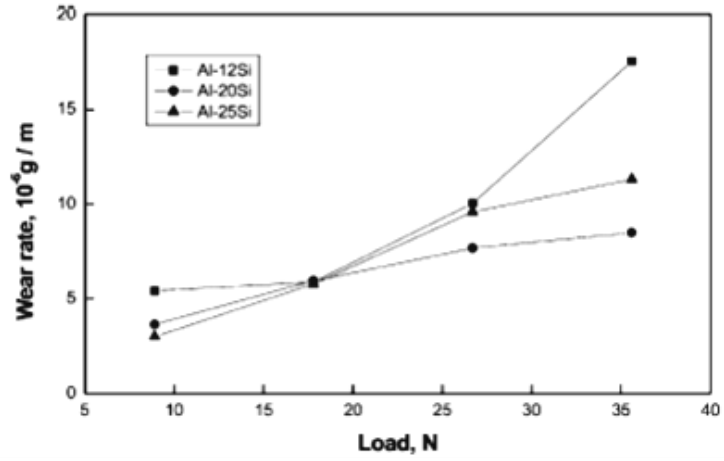


Fig.2.4. Plot of wear rate as a function of load. At low loads ( $\leq 20$  N) wear rate decreased with increasing Si percentage whereas at higher loads ( $\geq 25$  N) the Al-20 Si showed superior wear resistance [26].



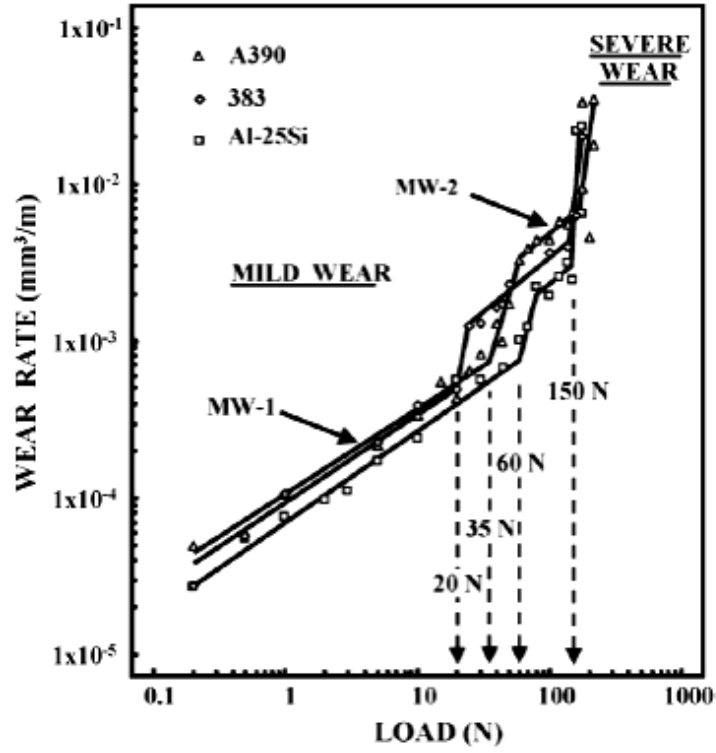


Fig.2.5. Wear rates of A390, 383 and Al-25 Si showing the presence of two subregimes of mild wear-MW-1 AND MW-2 [27].

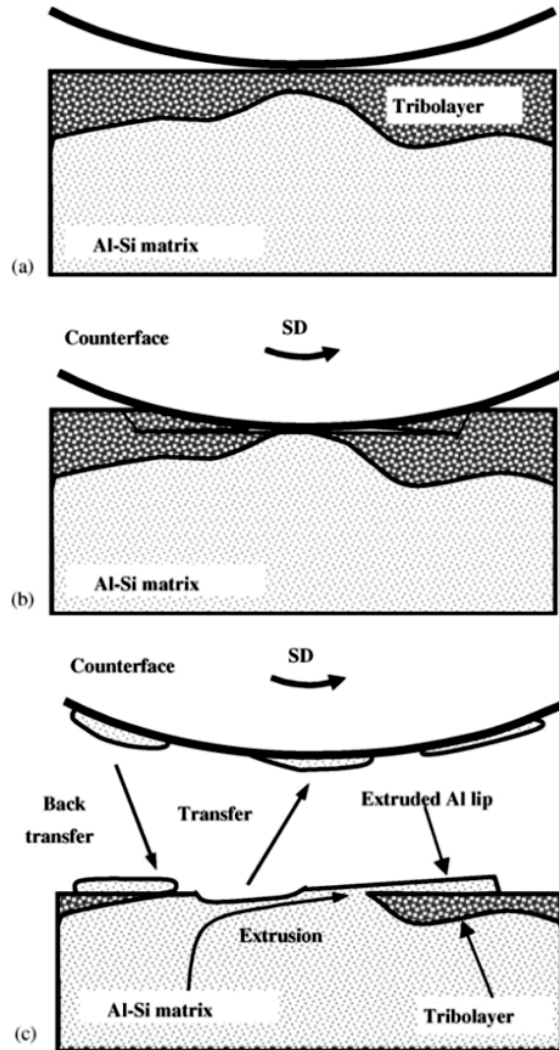


Fig.2.6. Schematic representation of processes leading to the formation of metallic aluminum layer (for A390) within tribolayers in MW-2. (a) Tribolayer supporting the load; (b) Removal of tribolayer exposing Al to counterface; (c) Extrusion of Al accompanied by metal transfer and back transfer processes [28].

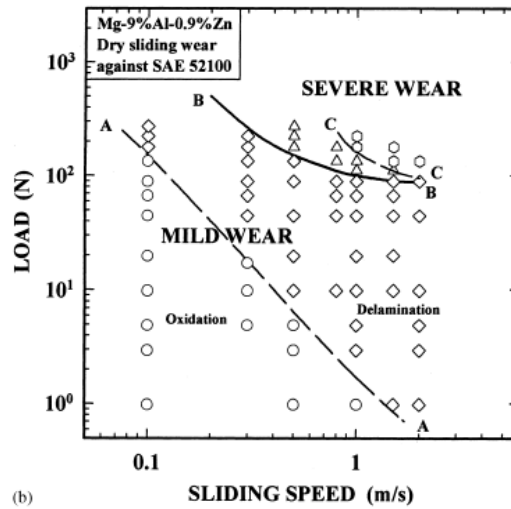
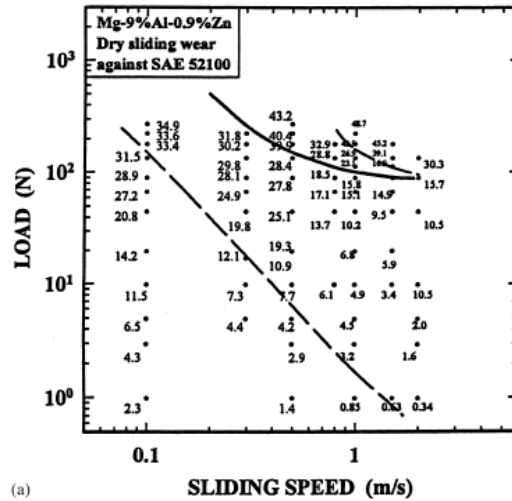


Fig.2.7. (a) Wear rate map for AZ91 in dry sliding wear. Each point on the map represents a wear rate measurement made at a given set of load and sliding speed. The continuous line represents the boundary between the mild and severe wear. The transitions between the sub-regimes are marked by dashed lines; (b) wear transition map for AZ91 showing the region of dominance of wear mechanisms and the transition boundaries between them: BB: mild wear to severe wear transition; AA [29].

## 2.2.2. Al and Mg metal matrix composites

### 2.2.2.1. Strengthening mechanisms in metal matrix composites

Strengthening mechanisms in metal matrix composites A composite is an artificially made multiphase material where the constituent phases are chemically dissimilar and are separated by a distinct interface [32]. Luo [33] fabricated Mg matrix composites by adding preheated SiC particulate (10 vol%) to molten commercially pure AZ91 (Mg- 9% Al-1% Zn) alloy. Mechanical properties like elastic modulus (EM), ultimate tensile strength (UTS), yield strength (YS) and elongation to failure ( $E_f$ ) were determined by tensile testing, and the fracture surfaces were analyzed using a scanning electron microscope (SEM). Table 2-1 summarizes the improvement noted in the mechanical properties of the unreinforced alloy (AZ91) and the composite (AZ91-SiC<sub>p</sub>), consisting of a significant increase (56%) in the yield strength and a slight increase (5%) of the elastic modulus of the composite over the unreinforced magnesium alloy, although the UTS of the composite decreases. The strengthening of the AZ91/SiC composite is explained by comparing its strain hardening behavior with that of the unreinforced alloy. The as-cast microstructure of the composite is characterized by Mg-grains, grain boundary eutectic phase (Mg<sub>17</sub>Al<sub>12</sub>) and the reinforcing hard SiC particles. During plastic deformation the slip behavior of the Mg-grain is highly constrained by the intragranular and intergranular SiC particles, which are too strong to be deformed (elastic modulus of and fracture strength of SiC are 440 GPa and 2000 MPa respectively as compared to 42.7 GPa and 203 MPa of the AZ91 matrix). The significantly high strain hardening rate and yield strength of the composite might be attributed to the strong internal stress that develops between the SiC particles and the matrix, thus resisting slip in the Mg-matrix. This is schematically represented in Fig.2.8 where it is shown that the SiC particles and

the eutectic  $\beta$  phase  $Mg_{17}Al_{12}$  act as barriers to the slip line causing strengthening of the composite. A similar observation was made in the study of the solidification process of AM60 matrix alloy in the presence of  $Al_2O_3$  fibre reinforcement [34], where the grain refinement process consisted of heterogeneous nucleation of the eutectic phase on the reinforcement fibres. In another study on SiC reinforced Al (A356) matrix composite [35] it was pointed out that depending on the particle distribution, particle size, matrix grain size, and relative strength of the particle to the metal matrix, the distribution of the internal stress is complicated and usually creates triaxiality of the real stress state in the composite material. This model suggests that internal stress and stress triaxiality are responsible for a higher strain-hardening rate of the composite. Localized damage as a result of particle cracking, matrix cracking and interface debonding occurs when local superposition of internal and applied stress becomes sufficiently high and results in relaxing of the internal stress around the SiC particles to give the decreased strain hardening rate (at higher strain levels) approaching the strain hardening rate of the matrix alloy. Finally, the coalescence of these localized damages at even higher strain levels leads to fracture of the composite material.

Fig.2.10 [33] shows the grain refinement in the unreinforced AZ91 and the composite with the reduction in grain size by a factor of 3. The mechanism of grain refinement is illustrated in a study of solidification of Mg (AZ91)/SiCp composite [36]. Heterogeneous growth of primary magnesium on SiC particles is attributed to the major grain refinement mechanism. This was suggested on the basis of the significant numbers of SiC particles that are located within the primary magnesium grains, suggesting heterogeneous nucleation mechanism. The grain refinement effect was also attributed to

the reduced growth rate of the primary phase as a result of the presence of SiC particles around growing magnesium crystals, creating diffusion barriers to growth. This restricted growth provides sufficient time for the melt to generate more nuclei, leading to smaller grain size in the finally solidified microstructure. Thus, this reduction in grain size contributes to the strengthening of the composite material by the grain boundary strengthening mechanism. The relationship between yield stress and grain size is illustrated by the Hall-Petch relationship [37,38] :

$$\sigma_0 = \sigma_i + kD^{-1/2} \quad (2.3)$$

where  $\sigma_0$  = yield stress;  $\sigma_i$  = friction stress;  $k$  = locking parameter;  $D$  = grain diameter.

Trojanová et al. [39] studied the strengthening of Mg-xLi (x=4,8,12) composites reinforced by short, discontinuous  $\delta$ -alumina ( $Al_2O_3$ ) fibres by gas-pressure infiltration of evacuated fibrous preform (10 vol %) with metallic melt in the autoclave. The mean fibre length and diameter were 100  $\mu m$  and 3  $\mu m$  respectively. Compression tests were carried out on the Mg-composites (both particle- and fibre-reinforced) at temperatures ranging from room temperature to 300 °C using an INSTRON testing machine. The stress-strain curves for the fibre- and particle-reinforced composites at different strains and temperatures are shown in Fig.2.11. The various possible strengthening mechanisms include i) load transfer mechanism; ii) matrix strengthening due to grain size reduction,; iii) Orowan mechanism and iv) increase in dislocation density due to geometrical and thermal mismatch.

The shear lag model (Fig. 2.12) [38,40,41] assumes that load transfer occurs between the reinforcement and the matrix via shear stress at the reinforcement-matrix interface. The fibre acting as the reinforcement carries part of the applied load. This

model assumes uniform matrix deformation. The flow stress  $\sigma_{LT}$  necessary for composite deformation due to load transfer is calculated by Eqn.2.4. The strengthening component depends on the reinforcement volume fraction in the following way:

$$\Delta\sigma_{LT} = \sigma_m 0.5f \quad (2.4)$$

When the metal matrix composite is cooled from a higher processing temperature, mismatch in strains occur as a result of differential thermal contraction at the interface. The strain thus induced may be higher than the yield stress of the matrix, leading to the generation of new dislocation at the interface. Thus, after cooling, the dislocation density of the system increases. The new dislocation density and corresponding strengthening may be calculated using Eqn.2.5.

$$\rho_T = \frac{Bf\Delta f\Delta\alpha}{b(1-f)} \frac{1}{t} \quad (2.5)$$

where  $t$  is the minimum size of the reinforcing phase particles,  $b$  is the magnitude of the Burgers vector of the newly created dislocations,  $B$  is a geometrical constant,  $\Delta\alpha$  is the difference between the two thermal expansion coefficients and  $\Delta T$  is the temperature variation.

Similarly, the addition of the reinforcement phase induces the generation of geometrically necessary dislocations (GND) to accommodate the mismatch in plastic deformation of the matrix. The density of geometrically necessary dislocation may be calculated by:

$$\rho_g = \frac{f\delta\varepsilon_p}{bt} \quad (2.6)$$

where  $\varepsilon_p$  is plastic strain. The introduction of the reinforcement phase not only induces the generation of thermally formed and geometrically necessary dislocations, but also the

dislocations stored in the reinforcement phase. The resulting total dislocation density is given by Eqn.2.7.

$$\rho_{\text{total}} = \rho_t + \rho_G + (\rho_S + \rho_a) \quad (2.7)$$

where  $\rho_s$  is the statistically stored dislocation density in an unreinforced matrix and  $\rho_a$  is the diminished part of the statistically stored dislocations due to the addition of a reinforcing phase. The strengthening, calculated by the Taylor relation, is attributed to the deformation resistance induced by the reinforcement phase:

$$\Delta\sigma_D = \alpha_1 \psi Gb \quad (2.8)$$

where  $\alpha_1$  is a constant,  $\psi$  is the Taylor factor and  $G$  is the shear modulus of the matrix.

Closely-spaced hard alumina fibres and dislocation pile-ups in the vicinity of fibres provide resistance to dislocation motion. The strengthening as a result of this mechanism may be calculated as follows:

$$\Delta\sigma_{\text{OR}} = \left( \frac{Gb}{\Lambda} + \frac{5}{2\pi} Gf\varepsilon_p \right) \quad (2.9)$$

where  $\Lambda$  is the distance between fibres and  $\varepsilon_p$  is plastic deformation. It is generally accepted that Orowan strengthening [42] is not a significant strengthening mechanism for composites since particles are coarse and interfibre spacing is large.

At higher temperatures, stresses can attain yield stress and the composite undergoes plastic deformation owing only to temperature cycling. The thermal stress in the fibre-matrix interphase may be calculated by:

$$\Delta\sigma_{\text{TS}} = \frac{E_f E_m}{(E_f f + E_m (1-f))} f \Delta\alpha \Delta T \quad (2.10)$$



where  $E_f$  and  $E_M$  are Young's moduli of the reinforcing phase (fibres or particles) and the matrix, respectively. The thermal stress decreases with distance from the fibre (or particle). Volume-averaged residual stresses in the matrix reach their maximum value ( $\langle \sigma_m \rangle_{\max}$ ):

$$\langle \sigma_m \rangle_{\max} = \frac{2}{3} \sigma_y \ln\left(\frac{1}{f}\right) \frac{f}{1-f} \quad (2.11)$$

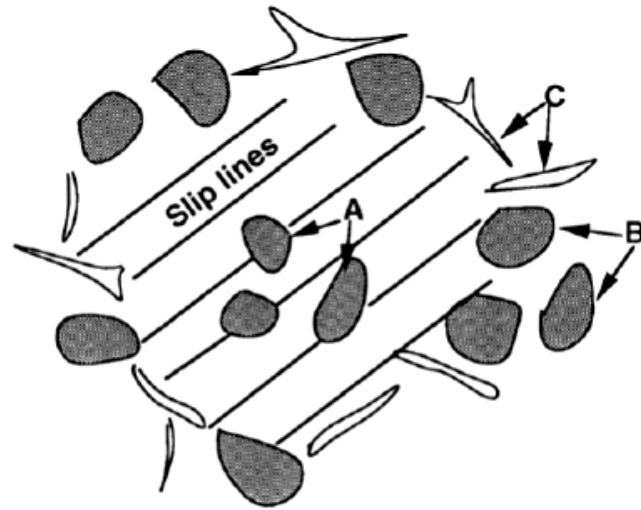
where  $\sigma_y$  is the yield stress of the matrix.

The variation of flow stresses with temperature may be due to the cross slip recovery process, which is more facile in bcc ( $\beta$ ) structure as the screw dislocation segments are easily mobile at elevated temperatures. Also, at elevated temperatures, the probability of dislocation climb increases, affecting the flow stress of the composite. At elevated temperatures the dislocation motion as a result of cross-slip and dislocation climb results in softening of the composite.

In summary, it has been described that the flow stresses of the composites are substantially higher than those of the unreinforced alloy. Load transfer from matrix to reinforcement phase due to shear stresses at the fibre-matrix interface were of greatest importance in the fibre reinforced composite, whereas in the particle-reinforced composites small grain size plays a predominant role. The increase in dislocation density as a result of thermal and geometrical mismatch is also important while considering strengthening of the matrix.

Table 2-1. Tensile properties of AZ91 alloy and AZ91/SiC composite. [33,36]

Material	Elastic Modulus (GPa)	0.2% Yield Strength (MPa)	Ultimate Tensile Strength (MPa)	Elongation %
AZ91	42.6	86.7	203	7.1
AZ91/SiC	44.7	135	152	0.8



- A - intragranular SiC particles**
- B - intergranular SiC particles**
- C - eutectic B phase ( $Mg_{17}Al_{12}$ )**

Fig. 2.8. Schematic diagram showing the particle-matrix interaction in the AZ91/SiC composite [33].

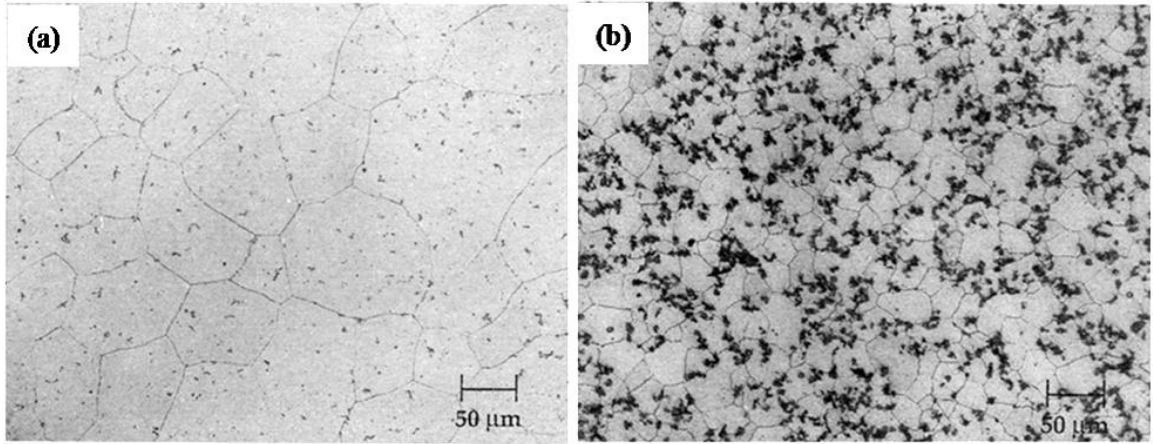


Fig. 2.9. Optical micrographs of (a) unreinforced AZ91 alloy and (b) AZ91/SiC composite [33].

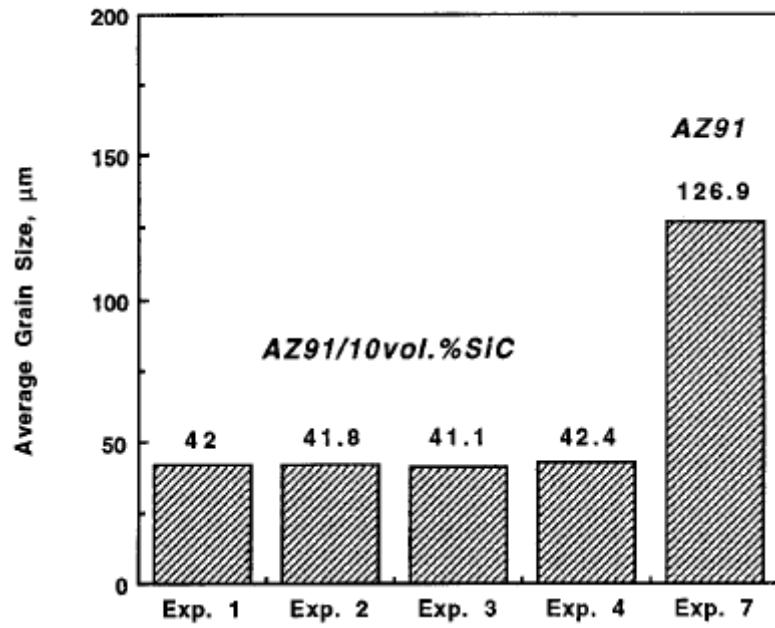


Fig.2.10. Average grain size for unreinforced AZ91 and AZ91/SiC composite [33].

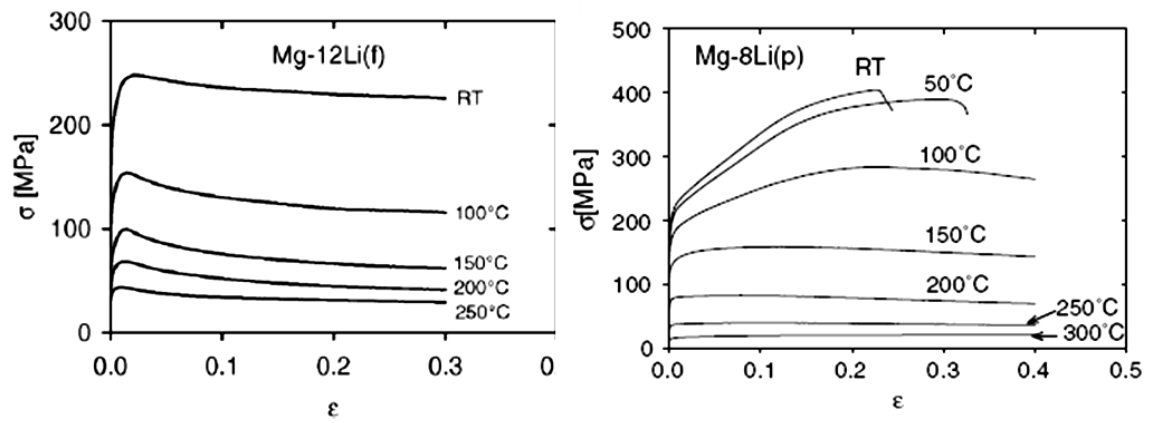


Fig.2.11. Stress-strain curves for (a) Mg-8Li (f) composites and (b) Mg-8Li (p) composites at various temperatures [39]

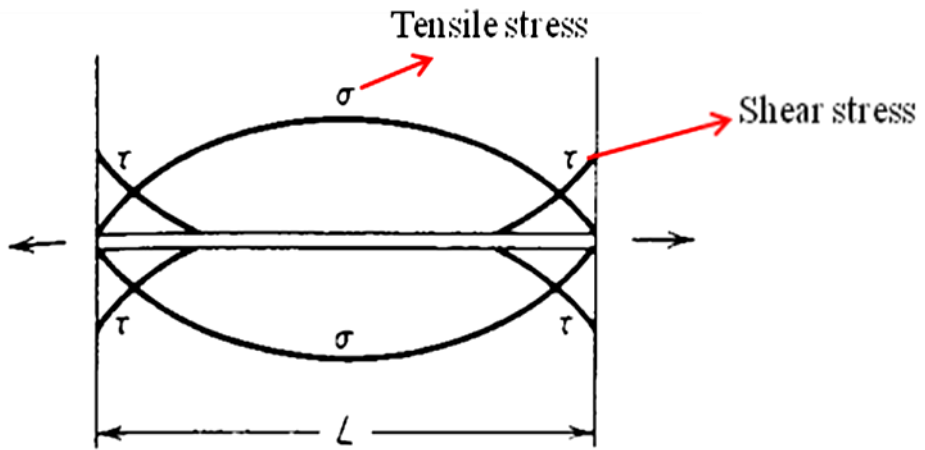


Fig.2.12. Variation of stress along a fibre in a fibre reinforced composite [38]

#### 2.2.2.2. Wear of Al and Mg matrix composites

Aluminum matrix composites have been developed for potential applications in automotive engines, in particular for cylinder liners where scuffing resistance during lubrication starvation conditions is very significant. Development of Al-Si composites reinforced with SiC particles and graphite flakes or particles have delayed the transition to seizure under dry and boundary-lubricated conditions. This can be attributed to the formation of tribolayer or mechanically mixed layers, which protects the worn surfaces, resulting in lower wear rates. The extent to which these films (oxide, adsorbed boundary lubricant, etc.) prevent intermetallic contact influences the relationship between the wear rate and the applied load. The transition between mild to severe wear regimes is associated with the breakdown of this protecting surface film [18]. The tribolayer is usually formed on the wear tracks, exhibiting different chemical composition and structural morphology compared to the bulk material, as a result of plastic deformation, transfer, interactions with the environment and mechanical mixing [43].

Characterization of the tribolayer (also termed the mechanically mixed layer (MML)) formed on the worn surface during dry block-on-ring wear tests performed on Al-Si casting alloy (A356) reinforced with 20% SiC particles against tempered M2 tool steel has been done using electron microscopy along with EDS, XRD and Mossbauer spectroscopy [44,45]. It was observed that the wear debris had microstructural features similar to that of the MML. The MML was comprised of  $\alpha$ -Al solid solution and  $\alpha$ -Fe from the counterface at low loads. At increased load, nanocrystalline structure of Fe-Al (Si) intermetallic compound and oxides of iron and aluminum formed due to oxidation and alloying caused by plastic deformation associated with frictional heating. Formation



of sandwich layers (either Fe rich or Al rich) provided evidence for material replenishment by material transfer and mixing during sliding wear.

SEM observations of worn surfaces of A356 Al-10% SiC-4% Gr and A356 Al-5% Al<sub>2</sub>O<sub>3</sub>-3% Gr [46] during dry block-on-ring wear tests against AISI 52100 steel show that a protective tribolayer was formed at nearly all sliding speeds and loads in the mild wear regime for both graphitic cast aluminum composites. The top surface of the tribolayer was comprised of iron oxide layers which were much more compact and hard (800 kg/mm<sup>2</sup>) in comparison with the bulk material while the rest of the tribolayer consists of fractured SiC, Al<sub>3</sub>Ni and Si particles (Fig.2.13) mixed with aluminum as indicated by EDS results. Lamellar graphite films were detected within the tribolayer, indicating the demarcation between the highly deformed tribolayer and the relatively undeformed bulk material. The fractured particles and thin graphite films, elongated in the sliding direction, contributed to the formation of a thicker and more stable tribolayer, delaying the mild-severe wear transition as compared to the A356 aluminum alloy and the non-graphitic aluminum matrix composites. It was also observed, however, that the steel counterface was subjected to scuffing or local material transfer from the composite as a result of abrasive action of the hard SiC carbide particles in the tribolayer and the friction heating-induced softening of aluminum. The authors concluded that such graphitic composites are well suited for use in the cylinder liners of an IC engine where scuffing resistance is significant.

Dry block-on-ring wear tests performed on A390 (Al-18.5% Si) in dry air as well as in an argon environment at different test loads against an AISI 52100 steel counterface show that wear rates were always lower in an argon atmosphere compared to dry air (5%

relative humidity) [23]. Cross-sectional SEM observations (Fig.2.14) revealed that tribolayer formation occurred on the worn surfaces under various testing conditions. The authors observed that in an argon atmosphere the initiation of sliding wear transfer of iron-rich layers occurred from the counterface to the exposed Si-particles, while as sliding progressed the composition of tribolayer changed to an Al-rich layer. Moreover, material detached from the tribolayers was also transferred to the counterface at a high rate. In air, the A390 surface was covered with iron-rich oxidized tribolayers at sliding distances over 50 m. Thus it can be concluded that the tribolayer composition and the depth of the damaged zone below it varies with testing conditions; the depth of the damaged zone and the magnitude of the subsurface plastic strains is lower compared to the results obtained in air.

In the past decade, an increasing number of studies on wear of Mg matrix composites have been conducted as a result of growing interest in Mg due to its potential applications as a lightweight alloy. Alahelisten et al. [47] examined  $\text{Al}_2\text{O}_3$ -fibre-reinforced Mg-9Al-1Zn (AZ91) composites during dry sliding, abrasion and erosion tests where the wear resistance was the highest for an optimum  $\text{Al}_2\text{O}_3$  fibre content of 10 vol%. For two-body abrasion, with increasing fibre content the abrasion resistance improved. Sharma et al. [48] studied unlubricated sliding wear behaviour of AZ91 composites reinforced with feldspar particles, with sizes ranging between 30.0-50.0  $\mu\text{m}$ . It was reported that the wear resistance of the composites was better than the unreinforced alloy and the wear rate decreased with increasing feldspar content. Also, the transition from mild to severe wear with increasing load was delayed due to the presence of feldspar particles. Franco et al. [49] studied dry sliding wear of AZ91 alloy reinforced

with TiC particles fabricated using pressureless infiltration techniques. It was concluded that the addition of TiC particles to the AZ91 alloy did not improve the wear resistance as the observed wear rate for the AZ91 alloy was approximately two times lower than the AZ91/TiC<sub>p</sub> composite. This result contradicts the general observation for Al [50-52] and Mg composites, both of which possess enhanced wear resistance over the corresponding alloys under dry sliding conditions. The authors reasoned that the failure of the interfacial bond between the matrix and the reinforcing TiC particles resulted in TiC particulate depletion during sliding wear. However, using ball-on-flat type dry sliding reciprocating wear tests at load range of 1.0-8.0 N and velocity range of 1.0-15.0 cm/s, Hu et al. [53] showed that wear rate of GW103K-based Mg matrix composites reinforced with saffil fibres show considerably lower wear rate compared to the matrix alloy. The dominant wear mechanisms were abrasion, plastic deformation and delamination wear. Lim et al. [54] studied the unlubricated wear characteristics of a Mg-9Al alloy and its 8 vol% SiC<sub>p</sub> reinforced composite under the load and sliding speed ranging between 10.0-30.0 N and 0.2-5.0 m/s, respectively, and reported five different dominant wear regimes: abrasion, oxidation, delamination, adhesion, and thermal softening and melting represented in the wear map (Fig.2.15). The authors suggested that the higher hardness of the composites, as compared to the alloy, improved their load bearing capacity and thus enhanced the resistance to adhesive and abrasive wear. However, the SiC<sub>p</sub> reinforced composite does not help in reducing wear rates for the thermally activated wear processes. Dry sliding wear characteristics of the hybrid Mg matrix composite were also evaluated by Jo et al. [55] where AZ91 alloy reinforced with short saffil fibres and SiC particles of size 1, 7 and 20 μm were worn against tool steel S45C using a ball-on-disk type tribometer under

load range of 5-30 N and sliding speeds of 0.1 and 0.2 m/s. The dominant wear mechanisms at low loads were abrasive/adhesive whereas at higher loads and higher sliding velocity the predominant wear mechanisms were severe abrasive wear and delamination wear. The authors reported that in the case of severe abrasive wear, an increase in the size of SiC particles decreased the material loss by serving as load bearing elements.

Thus, previous studies on the wear behaviour of Mg composites consisted of unlubricated wear test results where the wear resistance of the composite improved over that of the matrix alloy and the dominant wear mechanisms were reported to be abrasion, adhesion and delamination.

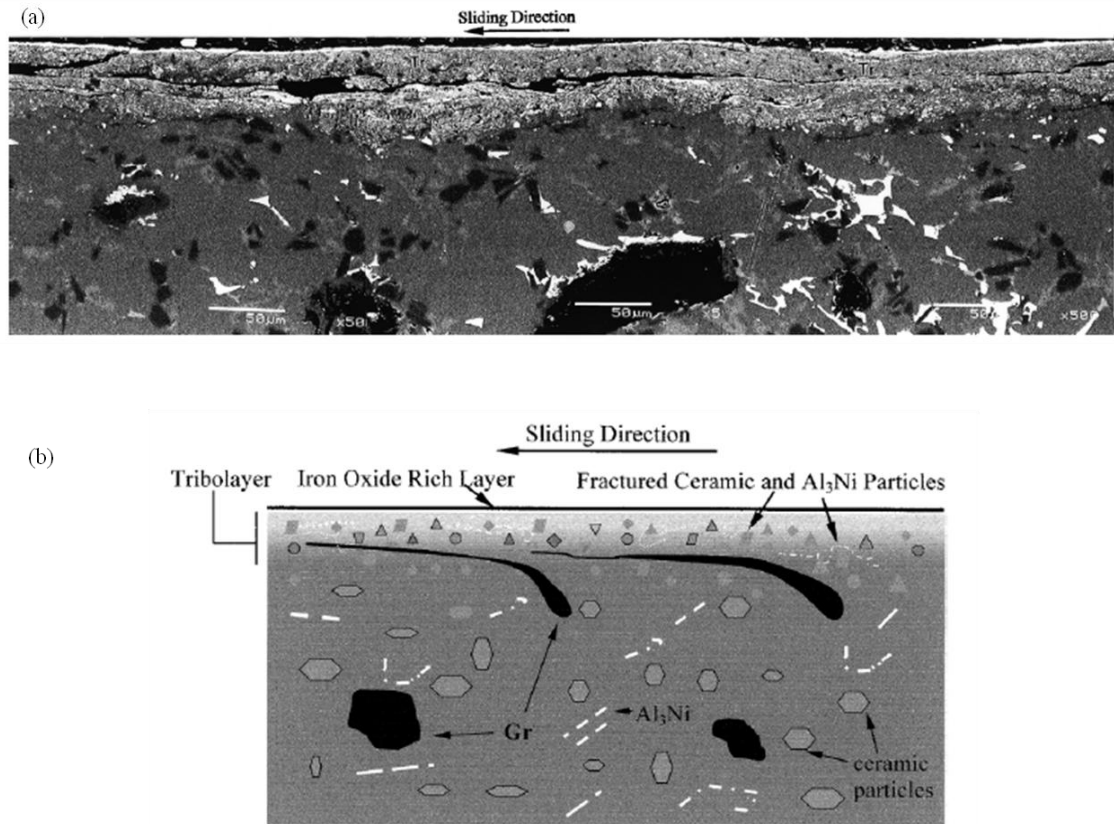


Fig.2.13. (a) Backscattered SEM image of cross-section of A356 Al-10% SiC-4% Gr worn at 159 N and 2.0 m/s; (b) Schematic representation of constituents of tribolayer in graphitic metal matrix composite [46].

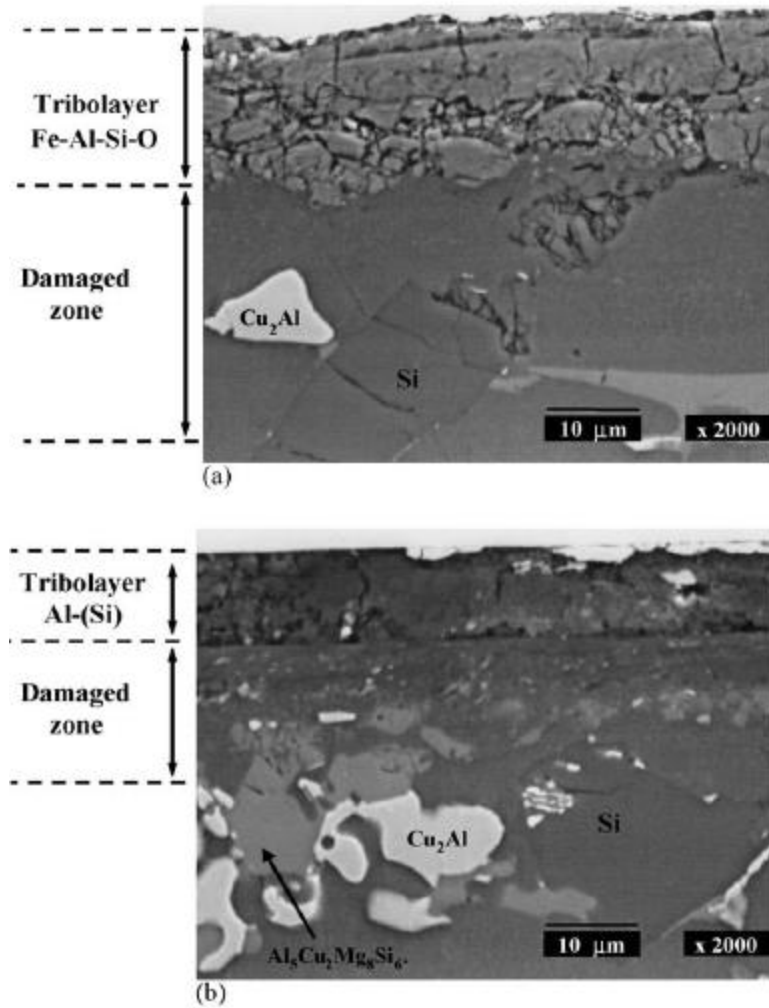


Fig.2.14. Secondary SEM micrographs showing the subsurface microstructures of A390 at 10 N in: (a) air and (b) argon indicating the difference in the composition of the tribolayer formed under different experimental medium [23].

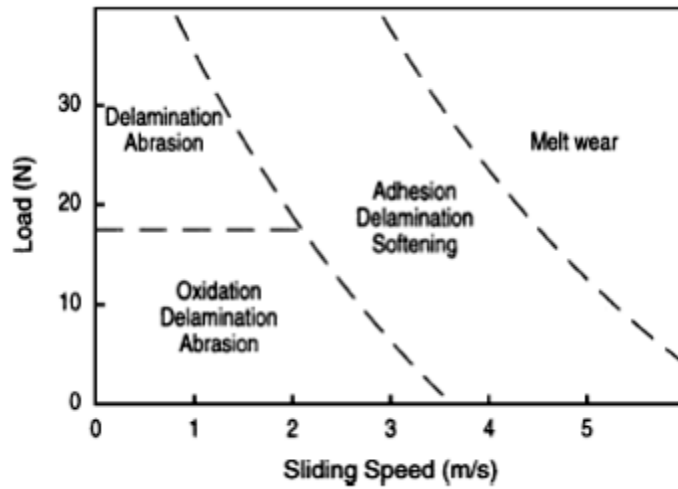


Fig.2.15. Diagram illustrating the conditions and approximate boundaries of dominance of the five wear mechanisms identified in the present study [54].

### **2.3. Wear stabilization under lubricated sliding conditions**

Previous studies on the wear behaviour of Mg composites consisted of unlubricated wear tests, which corresponded to wear regimes where the volume loss was significantly higher than that observed in lubricated engine running conditions, thus more closely emulating cold engine scuffing conditions [56,57]. However, piston cylinder bore assemblies running under lubricated conditions result in very low material removal, with the wear rate not exceeding a few nanometers per hour [10]. This feature qualifies engine wear to be classified as ultra-mild wear (UMW), since the rate of wear is a few orders lower than mild and severe wear. In addition, the micromechanisms of UMW are different from the traditionally observed mechanisms of mild and severe wear.

Due to negligible measurable weight loss during UMW, wear rate calculations cannot be performed by conventional mass loss techniques. Scherge et al. [10] developed a radionuclide technique (RNT) for wear measurement of mechanical systems showing low wear rates. Dienwiebel et al. [58] concluded from engine dynamometer tests that the Al matrix was modified due to running conditions and foreign particles were introduced as a result of wear. Studies regarding the UMW of Al-Si alloys have been reported in the literature [11, 58-64]. In these studies, pin-on-disk sliding wear tests were conducted on etched an Al-Si alloy at a load range between 0.5-5.0 N. These test parameters were chosen carefully as they are found to replicate the microstructure detected from actual engine running conditions (Fig.2.16a, b) [64]. Fig.2.16a and b represent the cross sectional TEM microstructures obtained from a worn eutectic Al-Si alloy (Al-11% Si) engine block and from an Al-11% Si sample tested under laboratory conditions, respectively. Both the micrographs show the presence of an oil residue layer (ORL),



supported by ultrafine Al grains, protecting the underlying Al matrix from further damage thereby stabilizing wear.

Chen and Alpas [60] and Dey et al. [63] studied the micromechanisms of UMW in Al–18.5% Si alloy in lubricated low-load sliding conditions. For the Al-18.5% Si alloy with large primary Si particles and high matrix hardness ( $85\pm 8.3$  HV), the surface damage was limited to scratch marks on the tops of Si particles, with the alloy retaining its original microstructure (Fig. 2.17a) when tested at very low load of 0.5 N, whereas Al-11% Si suffered damage due to the counterface after  $6\times 10^5$  cycles (Fig. 2.17b). When the load was increased to 5.0 N, Si particle fracture and fragmentation was observed at longer sliding cycles ( $>10^4$  sliding cycles) for Al–18.5% Si alloy and eventually led to surface damage and a corresponding transition from UMW to mild wear (Fig.2.18). The wear mechanisms therein comprised of i) fracture and fragmentation of Si particles, ii) sinking in of fragmented particles and iii) onset of mild wear when the Si particles were unable to protect the Al matrix by carrying the load. The authors, however, reported that after prolonged sliding the mild wear stabilized due to the oil residue layer formation.

The UMW in eutectic Al-Si alloys [11, 61] is characterized by sinking of the Si particles, which acted as load bearing elements, into the matrix. The Si particles with large aspect ratios underwent fracture followed by sinking in (UMW-I). Once the Al matrix and the Si particles reached the same height, the matrix suffered damage (UMW-II) by the counterface. This stage continued until a protective oil-residue layer formed (UMW-III) comprising of fractured Si particles comminuted to nano-sized fragments and organic components (Fig.2.19). Once this layer is formed the matrix was protected from further wear, indicated by a decreased wear rate (Fig. 2.20), and UMW regime prevailed

as long as the layer remained intact. It is to be noted that at the UMW-III stage, i.e. after the formation of a protective layer, the wear rates of Al-11% Si and Al-25% Si became comparable thus indicating that a high concentration of Si particles is not necessary for wear stabilization.

An investigation [62] of UMW damage mechanisms of Al-12.6% Si alloy investigated at 100 °C and compared with the results at room temperature showed that the three stages of UMW could be predicted depending on the value of  $\alpha$  and the ratio of aluminum matrix pile-up height to Si particle height. Also, at 100 °C an island-like tribofilm was observed on top of Si particles which acted as a load-bearing layer and led to lesser fracture and fragmentation of Si particles and delayed the transition from UMW-II to UMW-III.

The understanding of the unique process of microstructural evolution during sliding wear that leads to the formation of the ORL supported by nano-sized Al grains is the key to understanding wear stabilization during UMW in Al-Si alloys. Al nano-grain formation is similar to the processes observed in heavily cold-worked metals undergoing grain subdivision [65-68]. The process of grain refinement is qualitatively summarized as follows: Under low to medium strains ( $\epsilon=0.06-0.8$ ) the boundaries formed within a heavily cold-worked metal not only originate from the grain boundaries of the undeformed metal but also from the dislocation walls developed within the grains during plastic deformation. These walls later form subgrains (smaller than the original grain size) or cell blocks and are characteristically high angle grain boundaries (angles  $\geq 15^\circ$ ). The characteristics and orientation of these dislocation walls depend on the orientation of the grain with respect to loading. Under very high strains ( $\epsilon \geq 10$ ) the cell blocks tend to

reorient into a lamellar structure (Fig. 2.21), where lamellar boundaries sandwich thin layers of cell while the subgrains are oriented in the direction of material flow.

A lubricant is a chemical reagent (often a liquid) introduced between two moving surfaces to reduce the friction between them. An automotive engine lubricant commonly contains base oil and a mixture of various additives, incorporated for the purpose of minimizing wear, improving efficiency and consequently prolonging engine life. Most of the sliding surfaces in engines operate in a lubricated environment. Lubrication is characterized as hydrodynamic, mixed, or boundary lubricated according to the Stribeck curve (Fig.2.22).  $Z$  represents the lubricant viscosity, while  $N$  is the measure of sliding speed between surfaces,  $P$  being the applied load. In hydrodynamic lubrication, the surfaces are separated by a fluid film, which is thick in comparison to the asperity heights on the bearing surfaces. Hydrodynamic lubrication in an automotive engine is achieved by the movement of the oil, and dynamic viscosity is its most important property. As  $ZN/P$  decreases fluid film between the two solid surfaces become thinner and at low values the two bodies begin to interact. The region where the load is shared between the lubricant film and solid surfaces is known as mixed lubrication and is characterized by a sharp increase in the COF as  $ZN/P$  decreases. At a sufficiently low value of  $ZN/P$ , COF value rises to a maximum, marking the boundary lubricated condition. In the boundary lubrication condition the oil film thickness is too small to provide a film separation between the surfaces [69]. Tribologists continue to strive for developing new and more environmentally friendly oil additives to meet the tighter economic and ecological criteria.

The most effective class of antiwear, antioxidant and anticorrosive additive used in engine oil is zincdialkyldithiophosphate (ZDDP). A simple representation (Fig.2.23) of the structural formula of ZDDP is as shown below though molecular nature of ZDDP is more complex. Established surface analysis techniques like X-ray photoelectron spectroscopy (XPS), infrared spectroscopy (IR) as shown in Fig.2.24, and X-Ray absorption near edge (XANES) etc. have revealed the chemical composition of the surface films formed between the contact surfaces. Study of the chemical composition of the layer derived from ZDDP is the key to understanding the antiwear, anticorrosive properties of ZDDP.

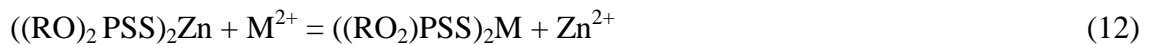
Bancroft et al. [70] have found that ZDDP tribofilms, 5  $\mu\text{m}$  across and 100 nm thick [71] formed on steel surfaces are chemically and mechanically stable. These films were composed of a mixture of long and short chains of polyphosphates, which were inter-grown with the metal oxide surface. This intergrowth provides strong attachment with the metal surface. It was further determined [72] that the layered short chain polyphosphates are present in the bulk whereas the layered longer-chain polyphosphates were present at the surface. The tribologically derived ZDDP antiwear film differs from its thermally derived counterparts in comprising a layered structure whereas the thermally derived ZDDP antiwear film lacks a layered structure but has the same chemical composition.

The chain length and composition of tribofilms derived from ZDDP are generally studied using XANES analysis. Fig.2.25 a,b indicates the P-L edge spectra of ZDDP films generated at different rubbing times. The P-L edge spectrum represents the spectral lines for phosphorus with electrons reflected from the L sub-shell. XANES analysis

permits two modes of analysis: total electron yield (TEY) and fluorescence yield (FY). Thus spectra obtained in the TEY mode, with ~5 nm of depth sensitivity, provide information regarding the surface features. The fluorescence yield (FY) mode has a sensitivity of ~ 60 nm and provides information regarding the bulk properties. The XANES spectra consists mainly of three humps marked a, b and c. The polyphosphate chain length is determined by the ratio of peak height of a/c. A higher ratio of a:c indicates larger chain length. From Fig.2.25 it can be concluded that the surface of the film consists of long-chain length polyphosphates while the shorter chain lengths are found towards the bulk.

Various mechanisms have been proposed regarding the ZDDP antiwear and antioxidant film formation on the steel surface. In solution ZDDP might undergo following reactions:

(i) Ligand exchange [73]: Labile dithiophosphate ligands can exchange the central metal cation (Zn in this case) with another divalent metal ion like Fe in the following way:



Thus ligand (LI) exchange plays an important role in the antiwear property of ZDDP.

(ii) Reaction with peroxides and hydroperoxides: Yin et al. [72] developed a five-step pathway for the decomposition of ZDDP on a steel surface:

a. ZDDP is adsorbed onto the metal surface.

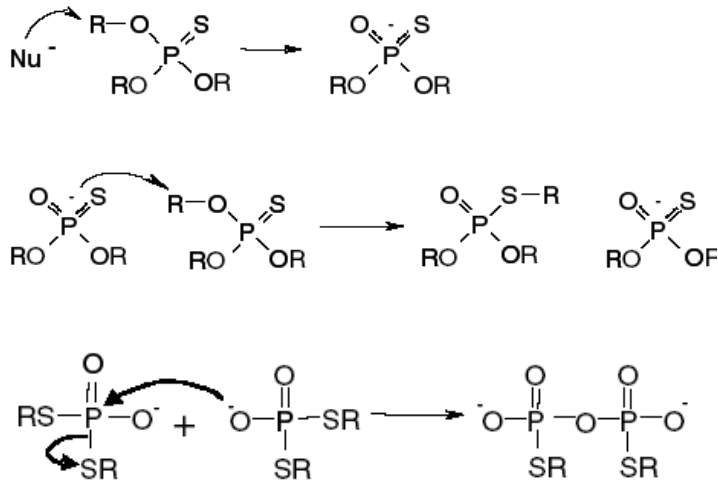
b. ZDDP (in solution) is converted to LI (in solution).

c. LI (in solution) is adsorbed to the metal surface.

d. Thermal-oxidation of adsorbed LI and ZDDP occurs by either  $\text{O}^2$  or  $\text{ROOH}$  to form long-chain polyphosphates  $\text{Zn}(\text{PO}_3)_2$ .

e. With continued rubbing, in the presence of water from the base oil, hydrolysis of polyphosphates occurs, creating short-chain polyphosphates.

(iii) Thermal degradation of ZDDP: In the absence of hydroperoxides/peroxy-radicals, ligand exchange ZDDP reacts in a different way at high temperature (130-230 °C). The mechanism of thermal degradation is described as the exchange of alkyl groups between O and S in the ZDDP molecule finally leading to the formation of polyphosphates according to the following reactions [73]:



For a steel surface, the formation of protective and sacrificial glassy-polyphosphate film as a result of the breakdown of ZDDP, limits the contact between the two rubbing surfaces. However, the exact mechanism resulting in formation of polyphosphates from degradation of ZDDP is yet to be determined. Some in situ analytical techniques along with vibrational and raman spectroscopy might be useful in this regard.

Literature studies have been conducted on the action of ZDDP as an antiwear agent in lubricated wear of Al-Si alloys. Wan et al. [74] performed ball-on-block

experiments on A2024 against AISI 52100 as the counterface under lubricated conditions at room temperature. The authors observed that the COF do not change with increasing concentration of base oil. Moreover it was reported that although ZDDP reduces adhesive wear it produces chemical wear. Hence the authors concluded that the addition of ZDDP in base stock is not beneficial in reducing wear and damage of aluminum alloys. They authors reasoned that the surface film produced by ZDDP is fragile and gets easily detached from the substrate, resulting in low concentrations of phosphorus, sulphur and zinc is observed in the surface film. However, there was no evidence to substantiate this observation. On the other hand, Fuller et al. [75] performed boundary lubricated tests on Al alloys 6061 and A-390 with ZDDP oil blend as the lubricant at 60 °C and 100 °C and concluded that addition of ZDDP to the base stock results in improvement of wear performance. The authors reported that ZDDP tribofilms formed on the worn surfaces of the Al alloys consist of polyphosphate structure identical to those formed on steel. This protective film formation occurred only after an extended period of rubbing. At 100 °C severe wear occurs, resulting in metal loss with insufficient tile for tribofilm formation. Nicholls et al. [76] reported similar results of tribofilm formation with identical composition to that of steel using XANES spectroscopy (Fig.2.26). Of the two Al-Si alloys studied, A-6061 and A-319, the latter showed increased efficiency of beneficial surface formation probably because of the increased Si content providing a platform for the surface film formation. Further in situ observations regarding the mechanism of formation of ZDDP at high temperatures for Al-Si alloys and its dependence on the percentage of Si content can inform future research.

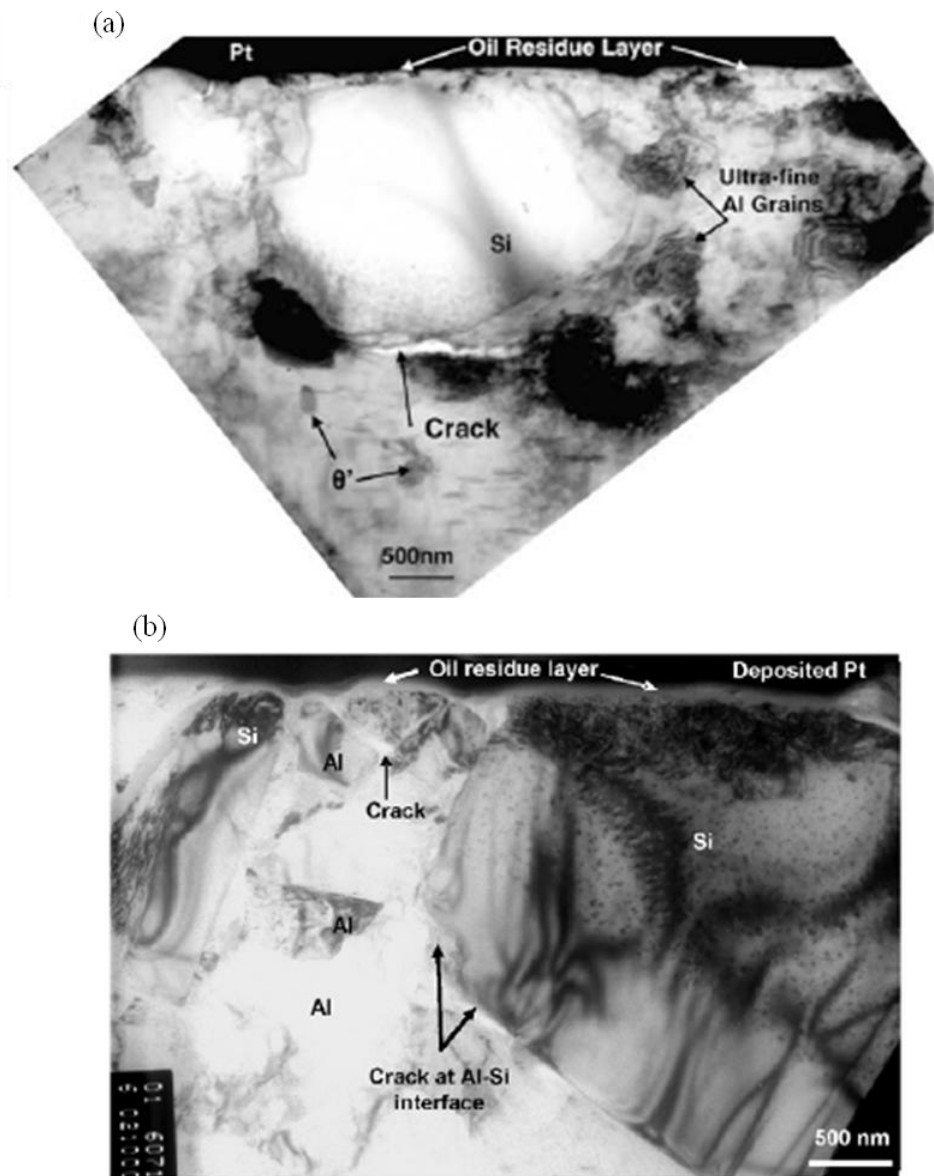


Fig.2.16. Cross-sectional TEM micrograph obtained from: (a) worn subsurface of Al-11% Si tested under laboratory conditions [11] and (b) worn Al-11% Si cylinder bore [64]. It is to be noted that both the microstructures show similar features and the presence of protective oil residue layer.



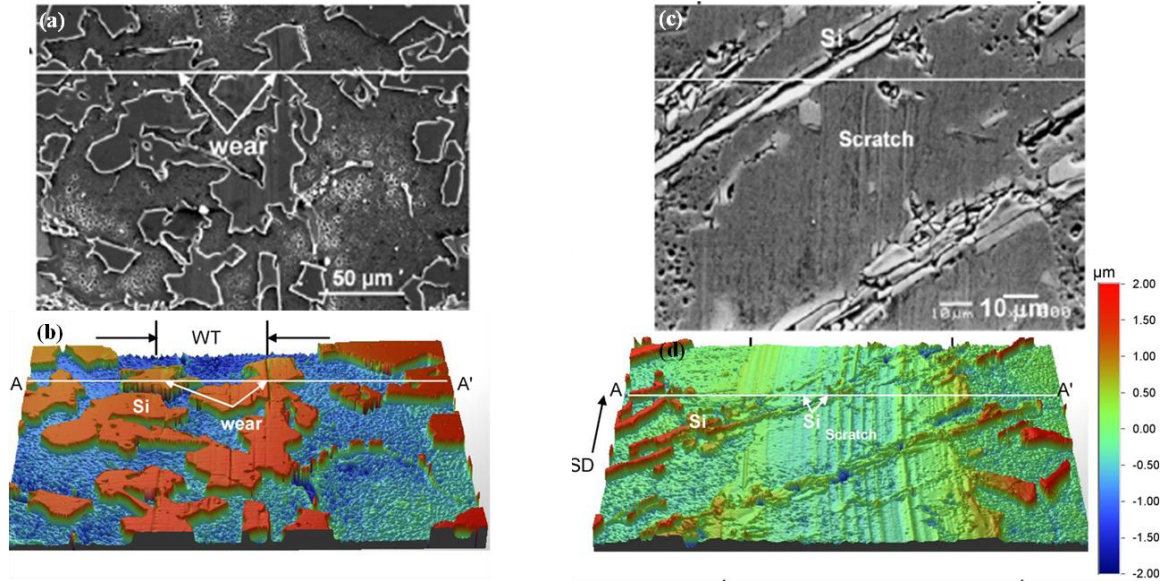


Fig.2.17. (a) and (b) represents SEM and optical profilometry images of Al-18.5% Si indicating scratches on Si particles with no damage to the matrix; (c) and (d) represents SEM and optical profilometry images of Al-11% Si showing matrix damage [60].

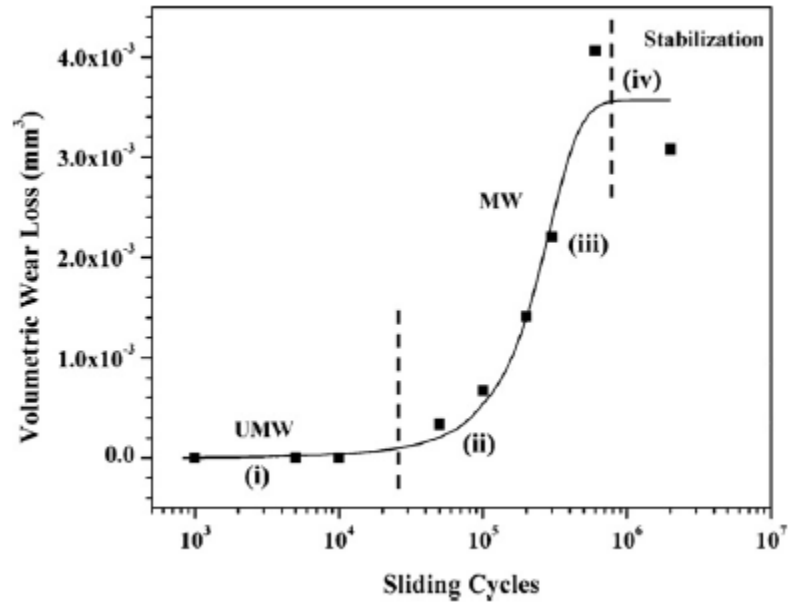


Fig.2.18. Volumetric wear loss of Al-18.5% Si at 5.0 N load. The wear loss is measurable after  $5 \times 10^4$  sliding cycles [63].

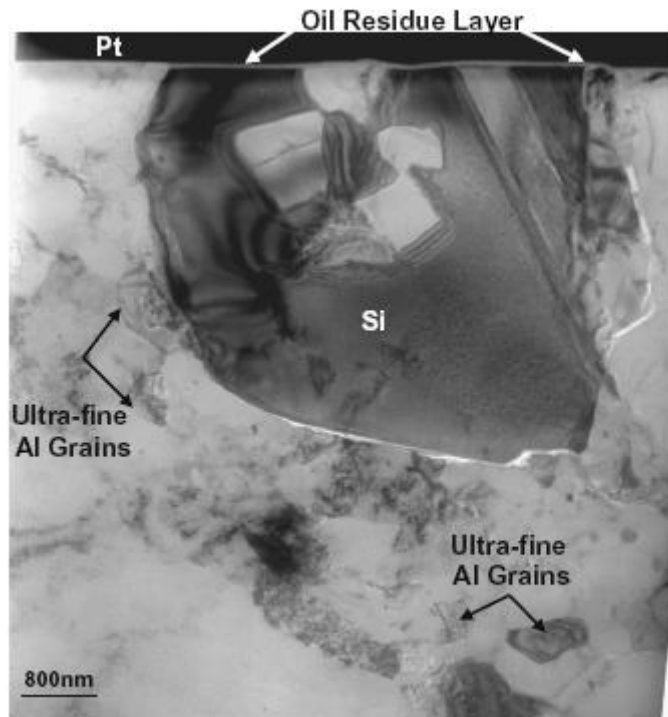


Fig.2.19. Cross-sectional TEM image of the microstructure of the material under the wear track showing ultra-fine aluminum grains around the silicon particle and the oil residue layer [11].

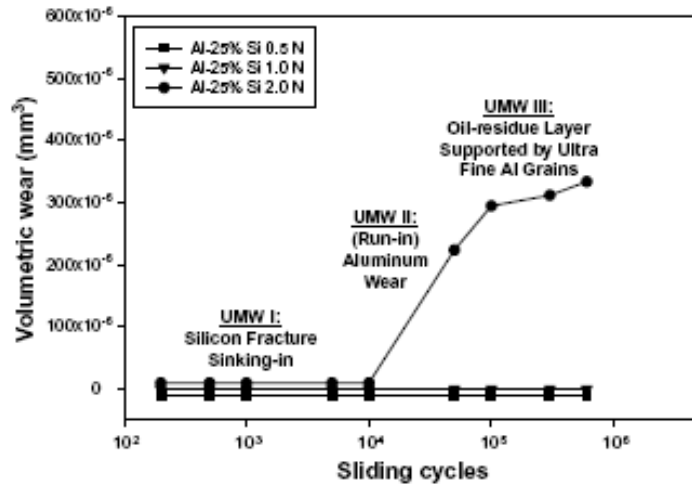


Fig.2.20. Variation of volumetric wear with sliding cycles in Al-11% Si in comparison with Al-25% Si indicating the three stages of UMW [11].

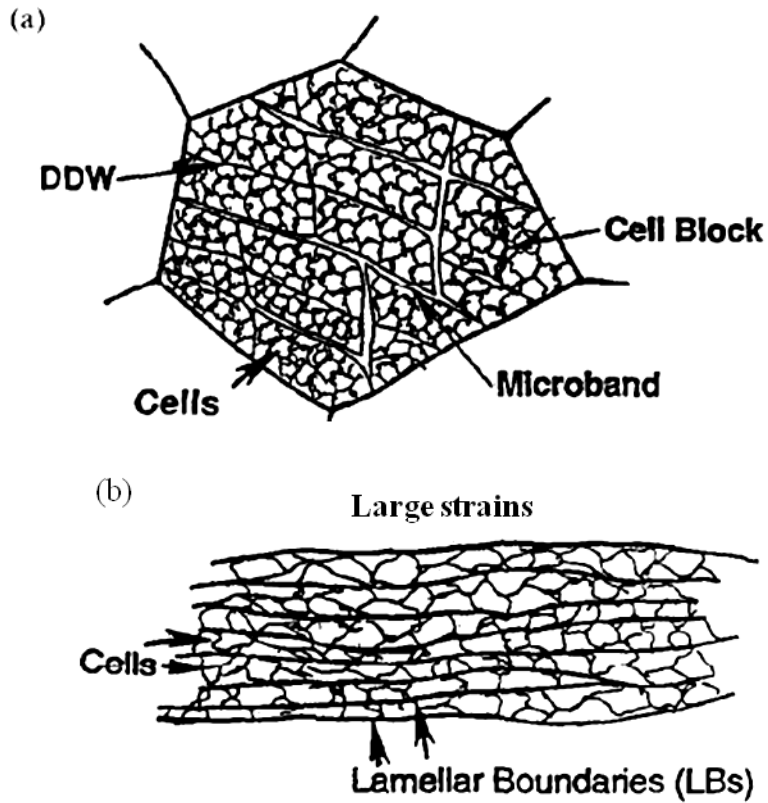


Fig.2.21. Schematic representation of deformation microstructures and grain subdivision process. (a) Small to medium strain deformation showing long microbands and dense dislocation walls surrounding groups of cells in cell blocks; (b) at large strain deformation, with lamellar boundaries parallel to the deformation direction, sandwiching in narrow slabs of cells or equiaxed subgrains [65].

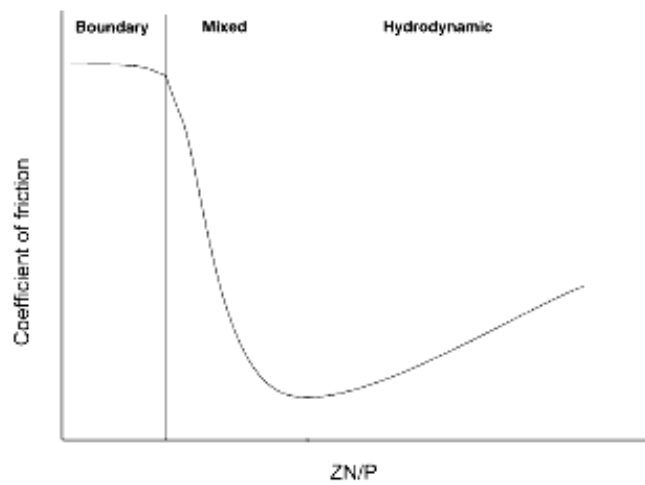


Fig.2.22. The Stribeck curve showing three lubricated regimes: boundary lubrication, mixed lubricated and hydrodynamic lubrication. Z=lubricant viscosity; N=sliding speed; P=applied load [77].

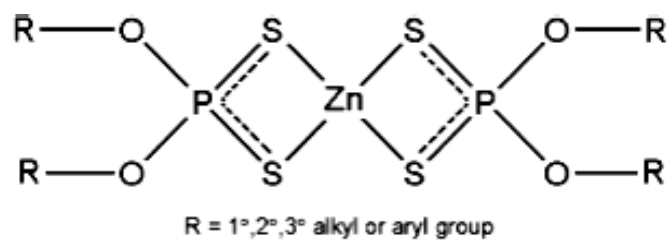


Fig.2.23 Structure of zinc dithiophosphate. The 'R' group indicates whether it's an alkyl or an aromatic dithiophosphate [78].

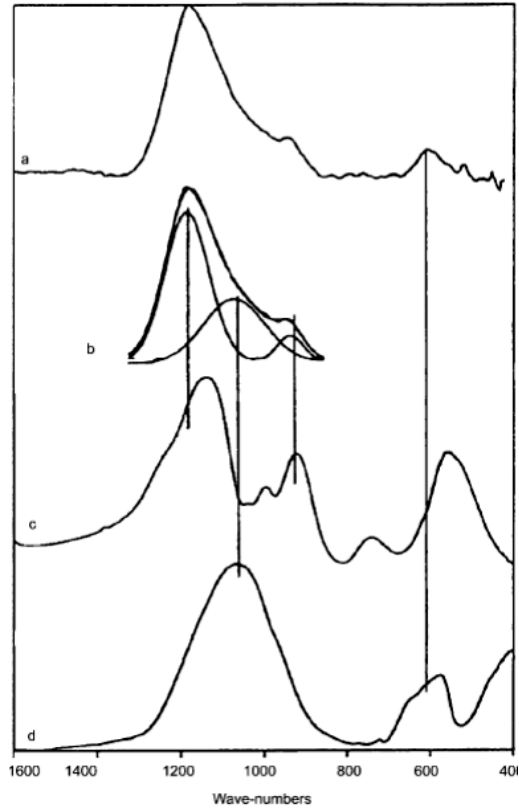


Fig.2.24. Infrared spectra for (a) tribologically derived ZDDP antiwear film; (b) a simulated spectrum of tribochemical film; (c) amorphous calcium pyrophosphate and (d) amorphous magnesium orthophosphate [79].



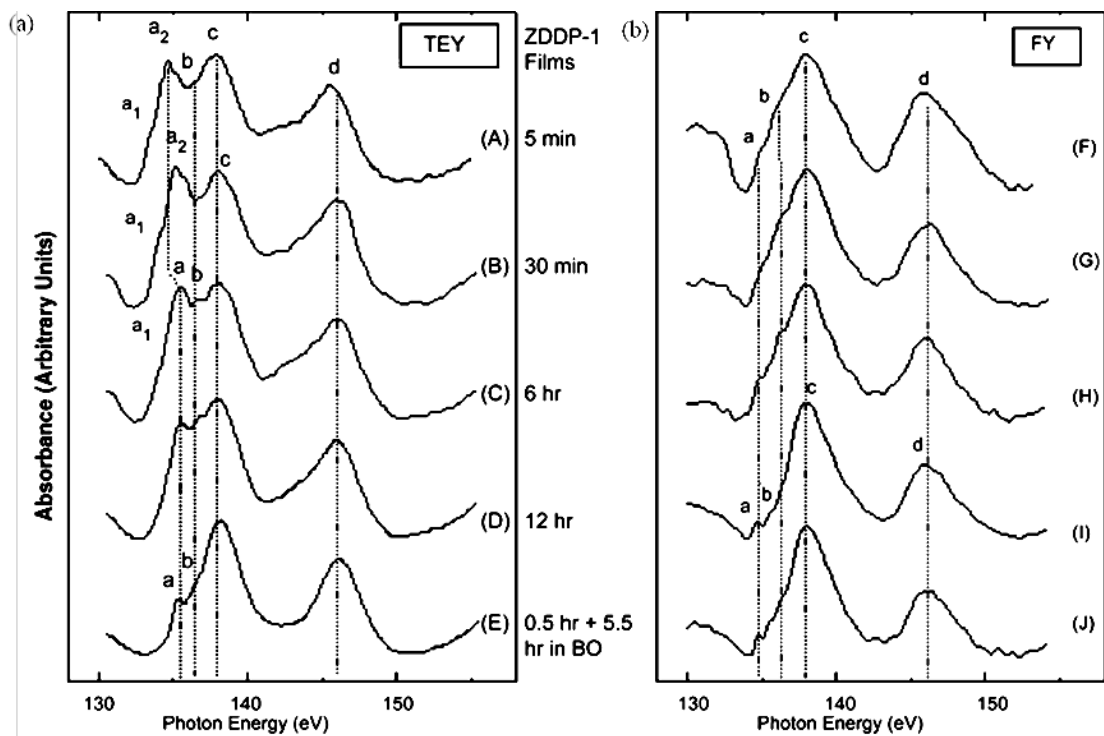


Fig.2.25. P L-edge spectra of ZDDP films generated under different rubbing times measured using (a) TEY and (b) FY modes. Differences in the polyphosphate chain-length can be observed between the surface (TEY) and the bulk (FY) of the film by comparing the a/c peak heights [72].

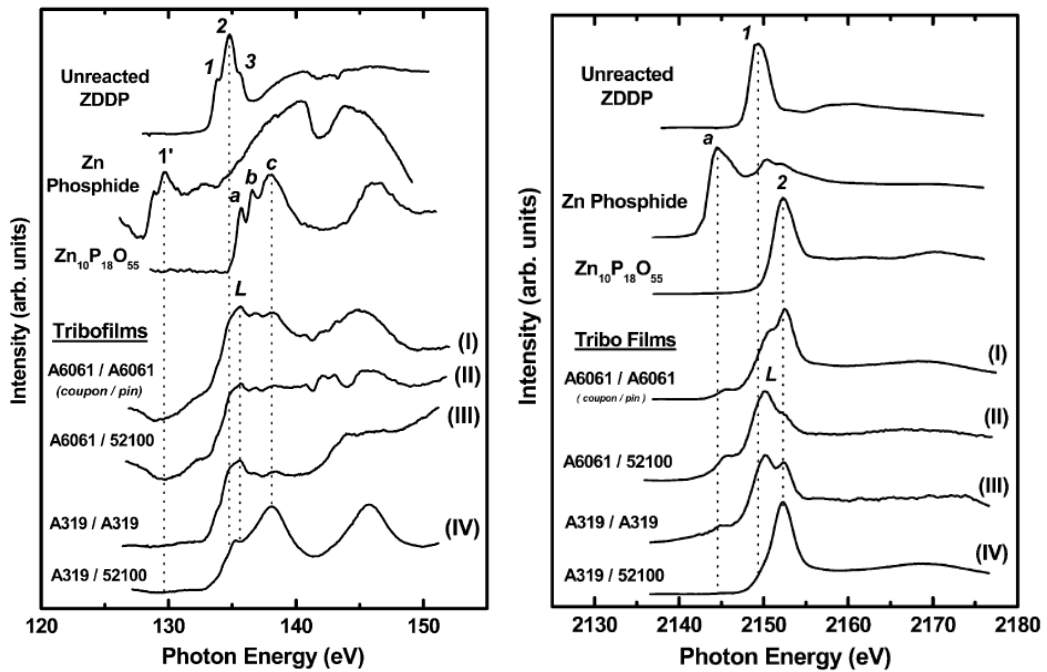


Fig.2.26. XANES spectra of model compounds and antiwear films formed on different Al-Si and steel couples. (a) P L-edge XANES spectra; (b) P K-edge XANES spectra [78].

## 2.4. Summary

Extensive studies have been conducted on the dry sliding wear of Al/Mg alloys and composites in which the dominant wear mechanisms and the factors affecting wear transition regimes have been discussed in detail. Comparatively fewer studies are found on the lubricated wear characteristics of lightweight metal-based alloys/composites. The understanding of ultra-mild wear of Al-Si alloys was a stepping stone towards the understanding of wear stabilization and the role of the tribolayer in the lubricated wear regime.

However, studies on the lubricated wear of Mg matrix composites are scanty in the literature. The understanding of ZDDP degradation in the Mg composites as a result of applied contact pressure and temperature during sliding wear is useful for the engine block-piston ring applications for which the current research is intended. Therefore the next few chapters outlining the current research will discuss:

- i) A squeeze casting technique for Mg composite and corresponding lubricated sliding wear test parameters,
- ii) A comparison of wear mechanisms of the matrix alloy and the Mg composite and the role of counterface,
- iii) The wear mechanisms and a description of the sequence of damage events,
- iv) Analyses and modeling the role of fibres and matrix on wear mechanisms.

## **Chapter 3: Experimental Methodology**

### **3.1. Introduction**

This chapter describes the experimental methodology used to fabricate composites and the experimental parameters employed to conduct sliding wear tests. The chapter starts with a description of the squeeze casting technique used to fabricate the Mg composites. This is followed by a section describing the parameters of pin-on-disk sliding wear tests. Finally, the different observation and quantification techniques used in this research have been described.

### **3.2. Description and Fabrication of Mg Matrix Composites**

The matrix alloy used for this study was squeeze cast AM60 with a composition (wt. %) Al: 5-6%, Zn: 0.2%, Mn: 0.4%, Si: 0.1%, Cu: 0.01% and balance Mg.  $\text{Al}_2\text{O}_3$  fibres and particles of varying volume percentages were incorporated in the alloy to prepare the composites. The reinforcement used was saffil fibres (97%  $\text{Al}_2\text{O}_3$ , 3%  $\text{SiO}_2$ ), obtained from Saffil Inc. and Thermal Ceramics Incorporation. These were prepared by collection of the as-spun gel fibre and passing it through a series of heat treatment stages to develop the crystalline microstructure. The presence of a small amount of silica (3 to 4 %) is effective in controlling crystal growth, allowing the gradual removal of porosity to optimize thermal mechanical properties.

The composites were prepared by a preform fabrication and squeeze casting method. The preform fabrication process consisted of converting the  $\text{Al}_2\text{O}_3$  fibres/particles into a powder form and flocculating this powder with a solution of polyacrylamide in water. The solution was stirred thoroughly overnight in water to break

down the fibre/particle clusters. The ceramic reinforcement was then dried and squeezed into a circular mold by application of load to prepare the preform (Fig.3.1). The preform volume percentage was determined by the following relation:

$$(Al_2O_3)_f \% = \frac{\rho_{\text{preform}}}{\rho_{Al_2O_3}} \quad (3.1)$$

where,  $\rho_{\text{preform}}$  and  $\rho_{\text{fibre}}$  are the densities of preform and the  $Al_2O_3$  fibres/particles constituting the preform respectively. The density of preform may be calculated by measuring the weight and volume of the preform. The dimensions of the preform were kept constant at 10 cm diameter (in sync with the lower die diameter) and 2.5 cm thickness. Increasing the  $Al_2O_3$  fibre content increased the weight of the preform and correspondingly a higher fibre volume percentage was obtained. Table 3-1 indicates the weights of preform corresponding to the different fibre volume percentages.

The fabricated preform was then dried and sintered at 300 °C to improve the compressive strength. Both the upper and the lower dies of the squeeze casting machine were preheated to 350 °C. The preform and the Mg alloy were heated to 450 °C and 750 °C respectively before pouring them into the lower die (Fig.3.2). The applied pressure in squeeze casting is an important variable that changes the microstructure and the mechanical properties of casting [80]. The solidification temperature of an alloy depends on the amount of pressure applied as determined by the Eqn.3.1, also known as the Clausius-Clapeyron equation [81], which relates the rate of change of melting point of a solid under pressure ( $dT/dP$ ) with its latent heat of fusion.

$$\frac{dT}{dP} = \frac{T_f (V_s - V_l)}{L_f} \quad (3.2)$$

where,  $T_f$  is the equilibrium solidification temperature,  $V_s$  and  $V_l$  are specific volumes of solid and liquid and  $L_f$  is the latent heat of solidification. The  $dT/dP$  of pure Mg has been calculated to be 0.0647 °C/MPa [81]. In this case, once the molten Mg was added to the die containing the  $Al_2O_3$  preform, the dies were closed by raising the lower die and fitting into the upper one. A constant pressure of 90 MPa was applied by the plunger into the die cavity to facilitate the infiltration of liquid Mg alloy in the gaps between the  $Al_2O_3$  preform. The applied pressure was maintained until the solidification of the casting was complete [34]. The resulting alumina reinforced fibre and fibre+particle reinforced composites were designated as AM60-x%  $(Al_2O_3)_f$  and AM60-(x%  $(Al_2O_3)_f$  + y%  $(Al_2O_3)_p$ ) where x and y are the volume of  $Al_2O_3$  fibre and particle added respectively. A schematic representation of the squeeze casting process is shown in Fig.3.3. The composites used to conduct sliding wear tests were AM60-9%  $(Al_2O_3)_f$ , AM60-11%  $(Al_2O_3)_f$  and AM60-26%  $(Al_2O_3)_f$  (Fig.3.4a-c). The alloy hardness was  $48.9 \pm 3.2$  HV or  $479.6 \pm 31.4$  MPa (1 HV=9.8 MPa) and the matrix hardness of the composites is reported in Table 3-2. In the composites, the  $Al_2O_3$  fibres in the composite had an average length of  $13.92 \pm 9.91$   $\mu m$  and a mean width of  $3.72 \pm 0.75$   $\mu m$  (Fig.3.5). The aspect ratio was calculated as 3.55.

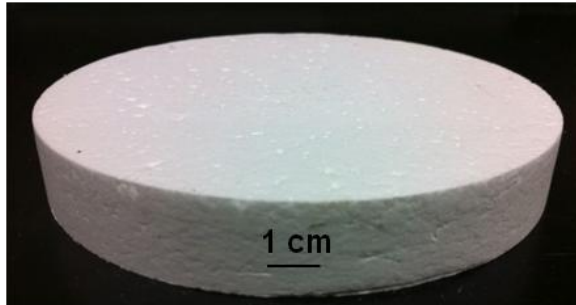


Fig.3.1. Al<sub>2</sub>O<sub>3</sub> fibre preform after compression and drying.

Table 3-1: Determination of preform volume percentage.

Weight of perform (g)	Volume of preform (cm <sup>3</sup> )	$\rho_{\text{preform}}$ (g/cm <sup>3</sup> )	$\rho_{\text{Al}_2\text{O}_3}$ [82] (g/cm <sup>3</sup> )	Al <sub>2</sub> O <sub>3</sub> fibre %
70.72	196.25	0.36	3.96	9.13
85.21	196.25	0.43	3.96	10.95
200.55	196.25	1.02	3.96	25.94

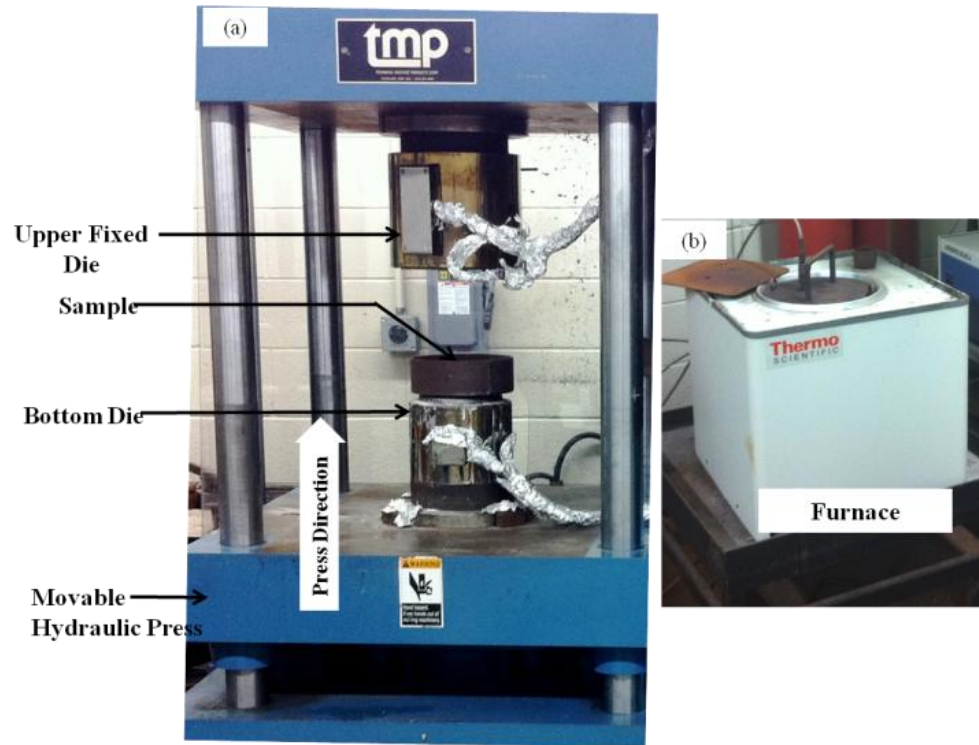


Fig.3.2.(a) The squeeze casting machine and (b) the furnace. The dies are closed by raising the lower die against the upper one by the hydraulic press. The magnesium alloy AM60 was melt at 750 °C in the furnace (b), and poured into the die.



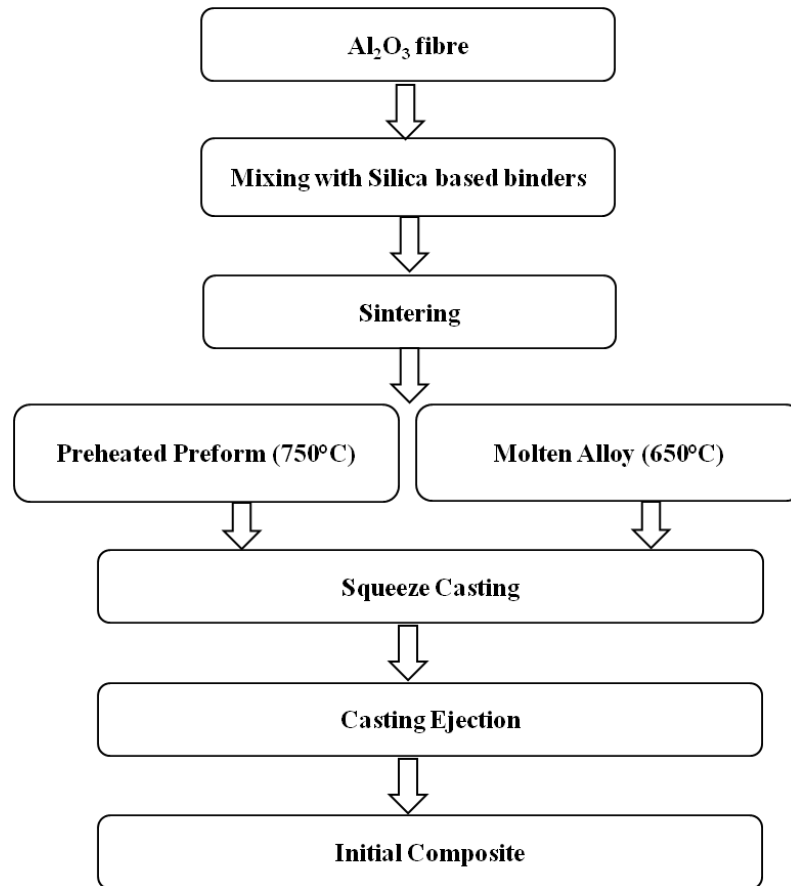


Fig.3.3. Flow diagram of the squeeze casting technique.

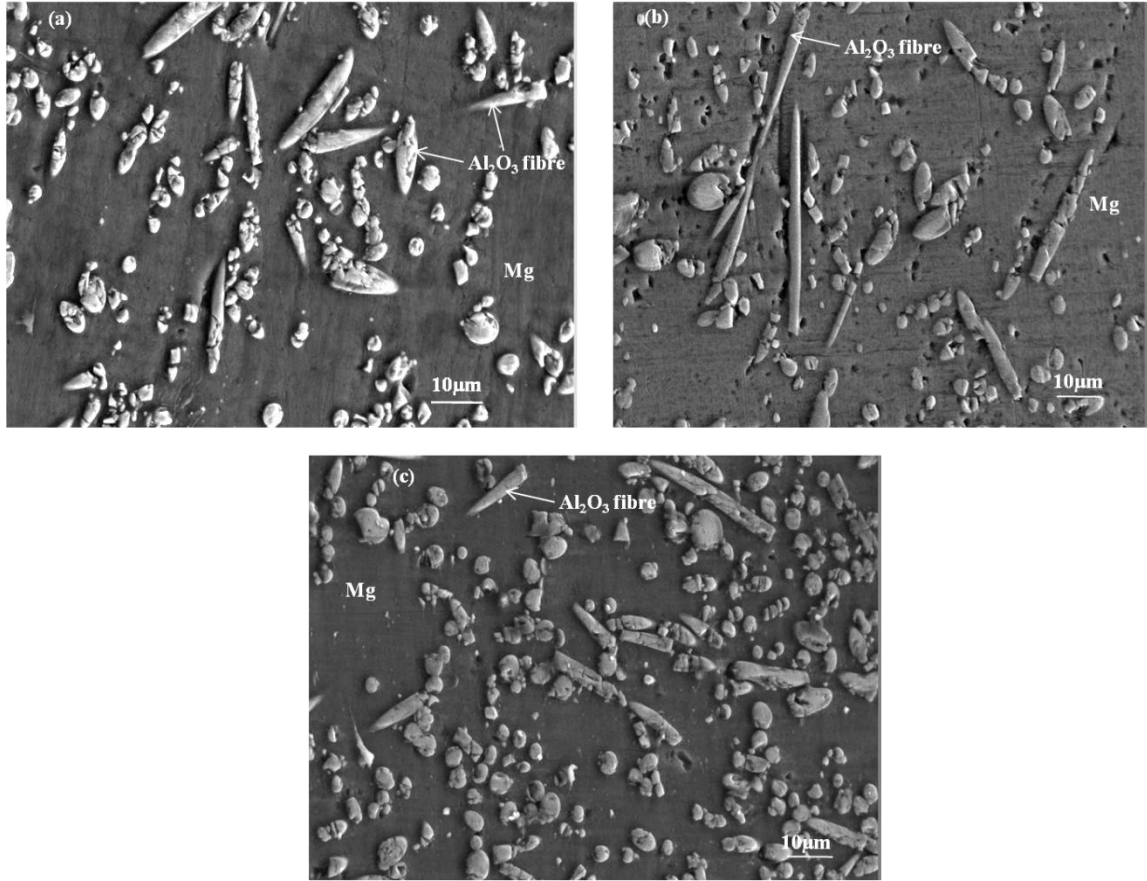


Fig.3.4. Secondary scanning electron micrograph showing the initial microstructures of (a) AM60-9% ( $\text{Al}_2\text{O}_3$ )<sub>f</sub>; (b) AM60-11% ( $\text{Al}_2\text{O}_3$ )<sub>f</sub>; (c) AM60-26% ( $\text{Al}_2\text{O}_3$ )<sub>f</sub>.

Table 3-2: Indentation hardness values AM60 alloy and fibre reinforced Mg composites.

	AM60	AM60-9% (Al <sub>2</sub> O <sub>3</sub> ) <sub>f</sub>	AM60-11% (Al <sub>2</sub> O <sub>3</sub> ) <sub>f</sub>	AM60-26% (Al <sub>2</sub> O <sub>3</sub> ) <sub>f</sub>
Hardness (MPa)	503±63	890± 47	1006±28	1390±53

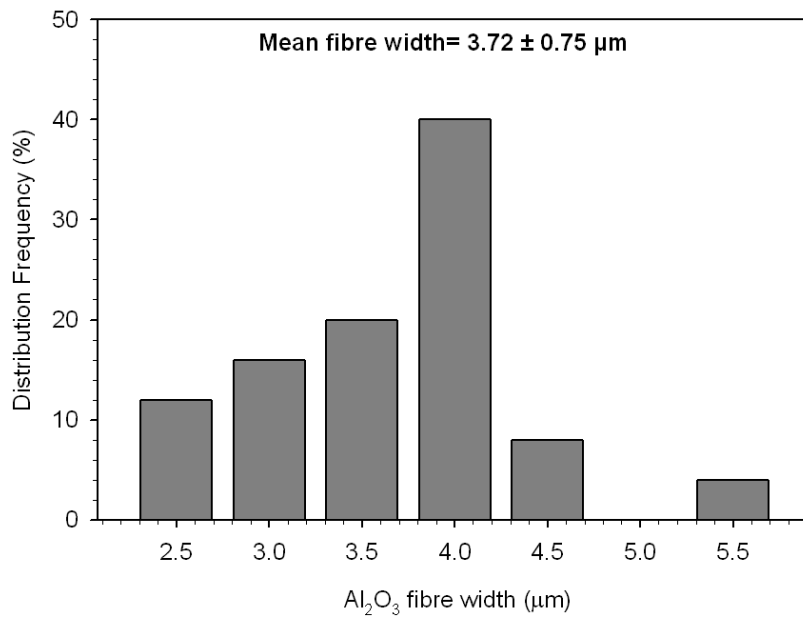
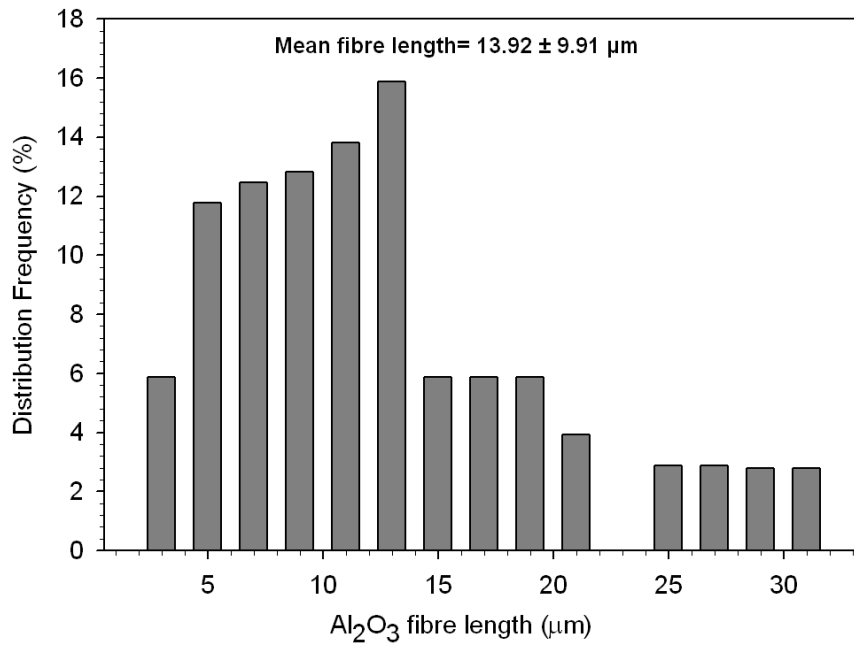


Fig.3.5. Al<sub>2</sub>O<sub>3</sub> fibre length and width distribution in AM60-9% (Al<sub>2</sub>O<sub>3</sub>)<sub>f</sub>.

### 3.3. Sliding Wear Tests

A pin-on-disk type tribometer (Fig. 3.5) was used to perform lubricated sliding wear tests on AM60-x% (Al<sub>2</sub>O<sub>3</sub>)<sub>f</sub> (where x=9%, 11%, 26%) and AM60-(9% (Al<sub>2</sub>O<sub>3</sub>)<sub>f</sub> + 4% (Al<sub>2</sub>O<sub>3</sub>)<sub>p</sub>) against 6 mm diameter AISI 52100 grade steel balls (700 HV) under 1.0-5.0 N loads, between 2.5×10<sup>4</sup>-1.0×10<sup>6</sup> sliding cycles and at a constant sliding velocity of 0.05 m/s. Wear tests were performed on the Mg composite AM60-9% (Al<sub>2</sub>O<sub>3</sub>)<sub>f</sub> at 25 °C and at 100 °C for comparison. The contact surfaces of all the specimens subjected to sliding wear tests were prepared using conventional grinding and mechanical polishing procedures to a final polish of 1 μm using a diamond suspension. The initial Al<sub>2</sub>O<sub>3</sub> fiber height protrusion above the Mg matrix was found to be 1.8±0.2 μm using an optical surface profilometer (WYKO NT-1100).

All wear tests were conducted under boundary lubricated conditions using synthetic oil SAE 5W-30. The lubrication regime was evaluated by calculating the ratio (λ) of minimum lubrication thickness (h<sub>min</sub>) and the r.m.s. roughness (r\*) of the surfaces in contact [69] using Eqn.3.3 and the parameters listed in Table 3-3.

$$h_{\min} = 1.79R^{0.47} \alpha^{0.49} \eta_0^{0.68} U^{0.68} (E^*)^{-0.12} P^{-0.07} \quad (3.3)$$

where, R=radius of the counterface (ball); U=sliding velocity; P=normal load; E\*=composite elastic modulus of the Mg-composites (discussed in section 5.2); α,η<sub>0</sub>=viscosity constants of the lubricating oil. The r.m.s roughness (r\*) of the two surfaces in contact is given by Eqn.3.3.

$$r^* = \sqrt{r_{\text{Mg-Al}_2\text{O}_3}^2 + r_{\text{ball}}^2} \quad (3.4)$$

where,  $r_{Mg-Al_2O_3}$  and  $r_{ball}$  are the r.m.s roughness of the  $Al_2O_3$  fibres and particles and the counterface steel ball determined by optical profilometry measurements. Thus the value of  $\lambda$  was calculated to be 0.25, 0.24 and 0.22 at 1.0 N, 2.0 N and 5.0 N loads respectively. The value of  $\lambda$  was calculated to be 0.058 under 2.0 N load at 100 °C. As  $\lambda < 1$  for all experimental conditions, the sliding wear tests satisfied the boundary lubrication regime.

### 3.4. Observation of worn surfaces

The wear features were quantified using an optical surface profilometer (WYKO NT-1100). Wear of composites occurred in the UMW regime where wear losses were less than that could be measured by a balance with sensitivity of  $10^{-5}$  g. Hence, optical profilometry calculations were employed to determine the material removal rates in the composites according to the reference [11]. The amount of material removal associated with the groove formations along the wear track were detected in this way. The amount of material removed was obtained from an area, A, by calculating the cross-sectional area that fell below a reference position with respect to unworn Mg matrix. The worn area was calculated using optical profilometry observations, with four readings from each image (Fig.3.7a, b)- where the area beneath the reference line, marked by dotted line in Fig.3.7b was calculated to be the worn area. An average of 24 readings (from six different regions of the wear track) was taken as the worn area  $A_{ij}$  and was multiplied by the perimeter of the wear track, which gives the volumetric wear loss W (Table 3-4) according to the Eqn.3.4 [11]:

$$W = \frac{2}{n} \pi R w \left[ \sum_{i=1}^n \sum_{j=1}^k A_{ij} \right] \quad (3.5)$$

where,  $k$  is the number of grooves per section and  $n=24$ : the number of different sections along the wear track from which measurements were made.

The  $\text{Al}_2\text{O}_3$  fibre height decrease was quantified using the histogram (Fig.3.8) obtained from the optical profilometry image. In Fig.3.8, the first peak represents the Mg matrix with a higher height distribution frequency whereas the second peak represents the  $\text{Al}_2\text{O}_3$  fibres. The horizontal distance between the two peaks,  $1.8 \mu\text{m}$ , was the fibre elevation over the Mg matrix in the initial surface. At  $5.0 \text{ N}$  load and after  $2 \times 10^5$  cycles, it is noticeable that the second peak merged with the Mg peak indicating that the  $\text{Al}_2\text{O}_3$  fibres and the Mg matrix are at the same elevation.

The worn surfaces were observed using a scanning electron microscope (SEM), JEOL 6400, equipped with an energy dispersive spectrometer (EDS) using both the secondary electron and the backscattered modes. Cross-sectional samples were prepared by cutting two narrow trenches, parallel to each other and to the wear track, on either side of the area of interest using focused ion beam (FIB) milling (Zeiss NVision 40), and a lift out technique. The  $\text{Ga}^+$  ion beam during the milling process was operated at  $30 \text{ kV}$ . The thin membrane between the two trenches was then removed using a lift-out device with an end effector and cleaned with a  $5 \text{ kV}$  followed by a  $1 \text{ kV}$  beam to reduce amorphization. The TEM samples thus prepared using FIB lift out technique were then examined using the Philips CM12 and JEOL 2010 transmission electron microscope operated at  $200 \text{ kV}$ .

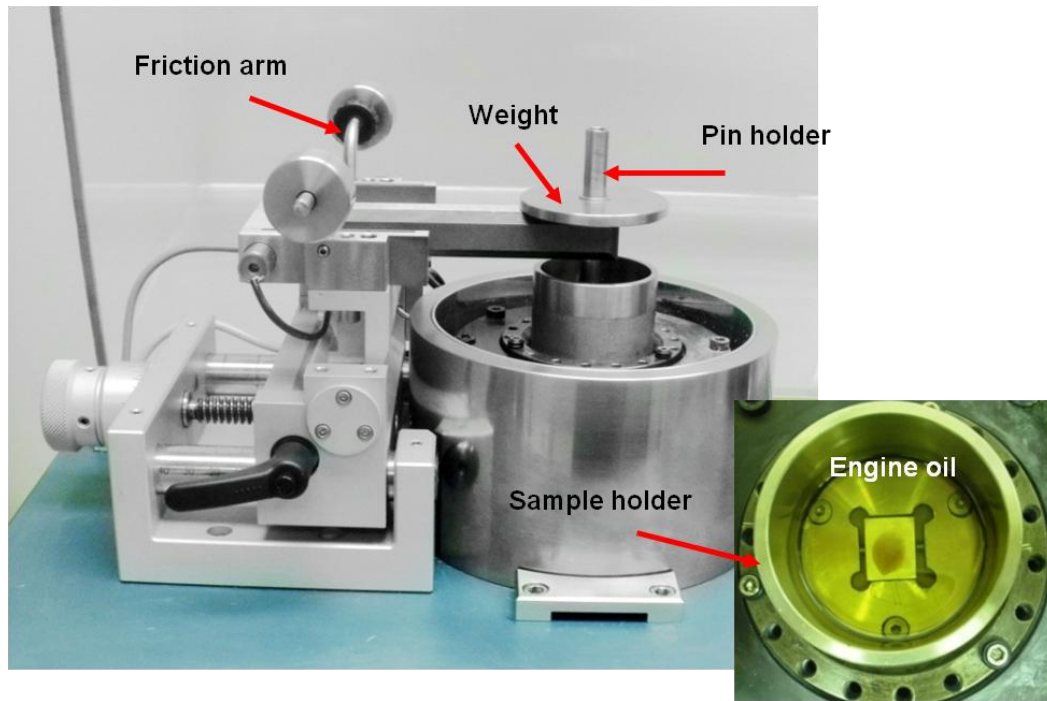


Fig.3.6. Pin-on-disk tribometer used to conduct lubricated sliding wear tests on Mg composites.



Table 3-3: Parameters for calculation of lubrication conditions.

R (m)	$\eta_0$ (PaS)	$\alpha$	U (m/s)	$E^*$ (GPa)	W (N)	$h_{\min}$ ( $\mu\text{m}$ )	$r^*$ ( $\mu\text{m}$ )	$\lambda$
0.003	0.052	$2.25 \times 10^{-08}$	0.05	42.11	5.0	0.0173	0.0758	0.22

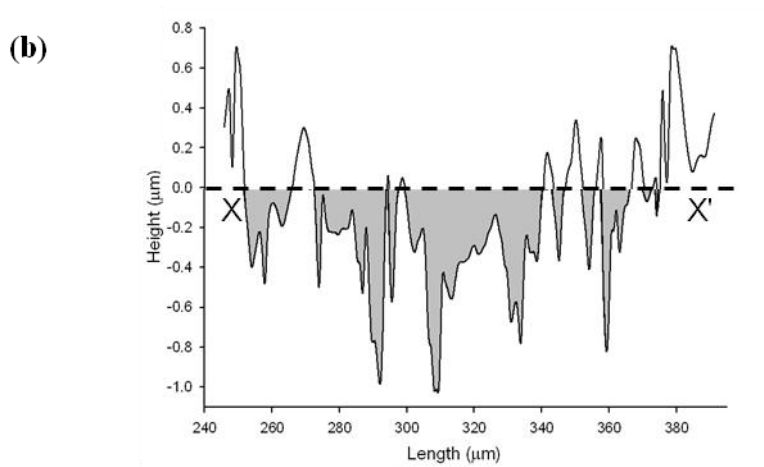
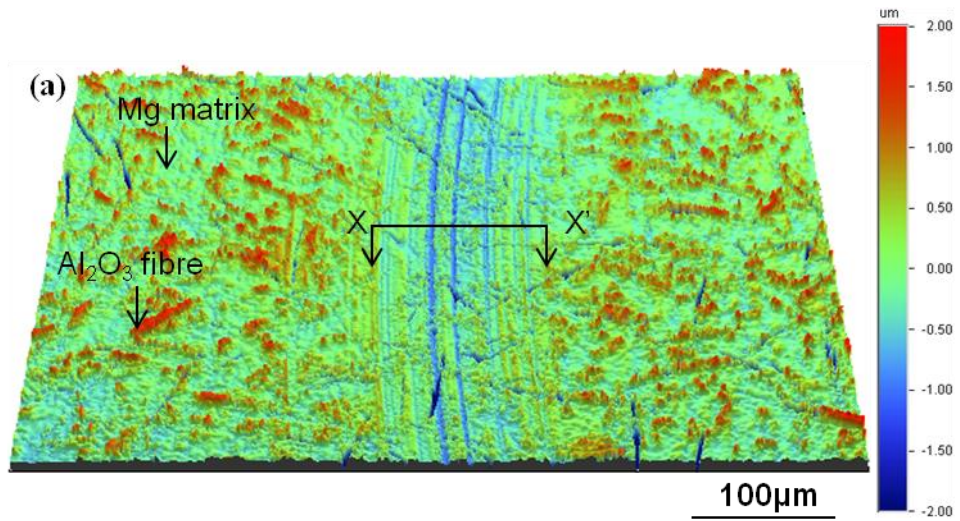


Fig.3.7. (a) Optical profilometry image used to calculate the worn area. (b) 2D-profile plot obtained from the marked X-X' region of image (a).

Table 3-4: The average volumetric wear loss calculated from the individual worn area loss calculated from different portions of the wear track.

Area ( $\mu\text{m}^2$ )	Volume ( $\times 10^{-3} \text{ mm}^3$ )
44.30	0.56
48.68	0.61
29.11	0.37
48.00	0.60
63.03	0.79
52.59	0.66
46.02	0.58
40.92	0.51
48.93	0.61
41.77	0.52
46.53	0.58
43.91	0.55
51.75	0.65
43.62	0.54
43.21	0.54
44.50	0.55
41.90	0.52
46.05	0.58
41.00	0.51
48.95	0.61
43.18	0.54
41.25	0.52
40.32	0.51

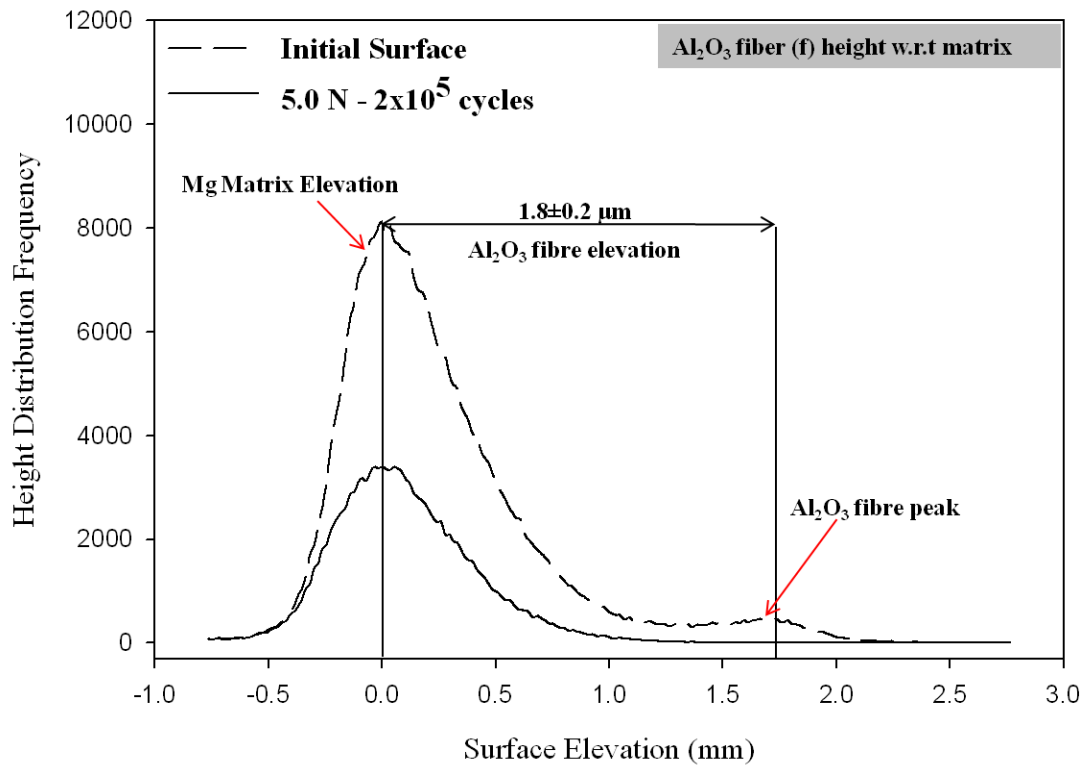


Fig.3.8. Histogram representing the decrease in the Al<sub>2</sub>O<sub>3</sub> fibre height from the initial surface after 2×10<sup>5</sup> sliding cycles. The horizontal distance between the two peaks is the Al<sub>2</sub>O<sub>3</sub> fibre elevation.

## Chapter 4: Results

### 4.1. Introduction

This chapter presents the results obtained from the wear tests conducted on Mg composites, describing the wear mechanisms in each case. The chapter starts with the description of the wear results of the matrix alloy AM60 along with a comparison with the composite. This is followed by the description of the results and wear mechanisms of the particle and fibre reinforced composite AM60-(9%  $(\text{Al}_2\text{O}_3)_f$ +4%  $(\text{Al}_2\text{O}_3)_p$ ) and AM60-9%  $(\text{Al}_2\text{O}_3)_f$ . The factors affecting the delay in the Mg matrix damage process are presented by describing the wear results of composites reinforced with different volume percentages of  $\text{Al}_2\text{O}_3$  fibre and also by comparing the wear results of AM60-9%  $(\text{Al}_2\text{O}_3)_f$  at room temperature and at elevated temperature.

### 4.2. Wear of Unreinforced Alloy AM60

Scanning electron micrographs (in the secondary electron mode) of the worn surfaces of the AM60 alloy (Fig. 4.1a), tested at 1.0 N load, indicate the prevalent wear features at low sliding cycles (i.e., for  $<1.0 \times 10^5$  cycles). The damage was observed in the form of wear grooves parallel to the sliding direction due to plastic deformation of the contact surface. Fig. 4.1b indicates that at higher sliding cycles, evidence for oxidative wear was found in addition to the matrix surface deformation. Presence of MgO was detected in the form of wear debris (Fig. 4.1c) on the wear track and also in the material transferred to the counterface (Fig.4.2). Therefore at higher sliding cycles the wear mechanisms consisted of oxidative type wear (Fig.4.2) along with transfer of material to the counterface.

The two different damage mechanisms detected at initial and longer sliding cycles is summarized in Fig. 4.3 which shows the wear losses of the AM60 alloy under 1.0 N load plotted as a function of sliding cycles. The plot showed a transition from  $4.05 \times 10^{-4} \text{ mm}^3/\text{m}$  to  $6.15 \times 10^{-4} \text{ mm}^3/\text{m}$  at  $\geq 3 \times 10^5$  cycles, the predominant wear mechanism being oxidative type wear and transfer of material to the counterface. However, within these two subregimes, the volume loss due to sliding wear increased linearly with the sliding distance, indicating that wear progressed under the steady state (i.e. constant wear rate) conditions.

Fig. 4.4a shows the SEM micrograph of wear track of the AM60 alloy at 1.0 N for  $2.5 \times 10^4$  sliding cycles and Fig. 4.4b shows the wear track of AM60-9%  $(\text{Al}_2\text{O}_3)_f$  at 2.0 N for  $6.0 \times 10^5$  sliding cycles. The greater extent of wear (width of wear track:  $0.73 \pm 0.08$  mm) for the AM60 alloy at 1.0 N in comparison to the composite AM60-9%  $(\text{Al}_2\text{O}_3)_f$  (width of wear track:  $0.35 \pm 0.02$  mm) is evident despite being worn at a higher load and for longer sliding cycles. This is further reflected in the comparison of the volumetric wear loss plot (Fig.4.5) between the alloy and the composite whereby the volumetric wear loss from the surface of AM60 alloy was  $10^2$  times higher than that of AM60-9%  $(\text{Al}_2\text{O}_3)_f$  despite the fact that the wear losses for the composite reported in this plot were measured at 5.0 N load.

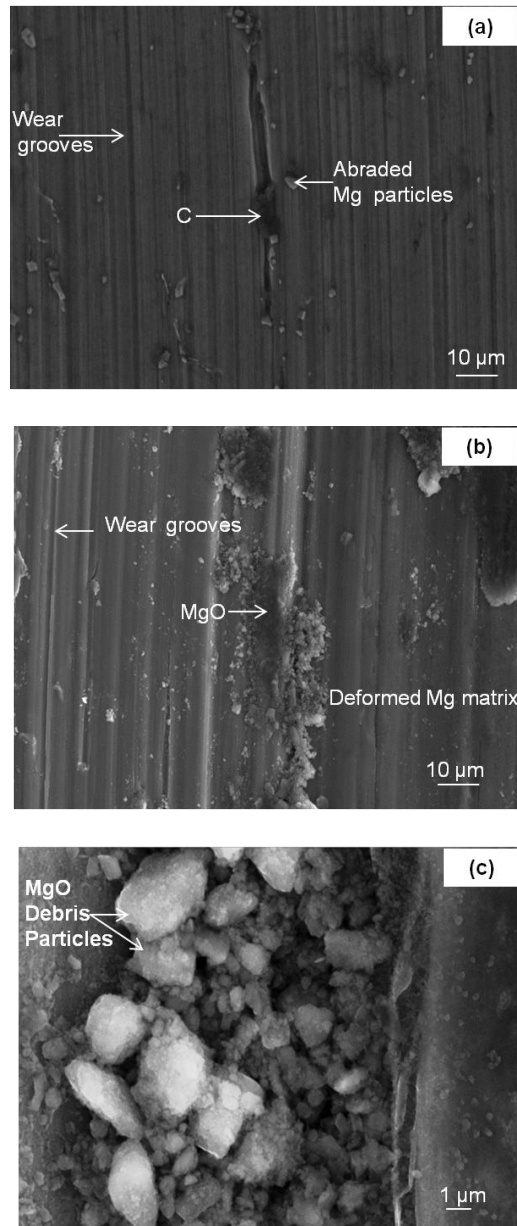


Fig.4.1. SEM micrographs (secondary electron mode) of worn AM60 alloy tested at 1.0 N load. (a) wear grooves observed at  $7.5 \times 10^4$  sliding cycles; (b) worn surface oxidation at  $4.0 \times 10^5$  sliding cycles; (c) MgO debris particles.

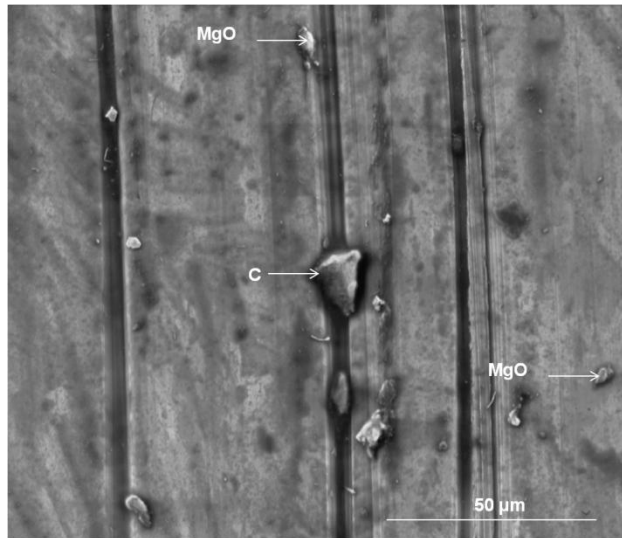


Fig.4.2. SEM micrograph of counterface AISI 52100 worn against AM60 matrix alloy, at 1.0 N load and for  $4 \times 10^5$  cycles, indicating the presence of MgO debris particles transferred from the worn composite surface and carbon (C) from the lubricating oil. This serves as evidence that at higher sliding cycles ( $\geq 2 \times 10^5$  cycles) oxidation and adhesion type wear occurred.



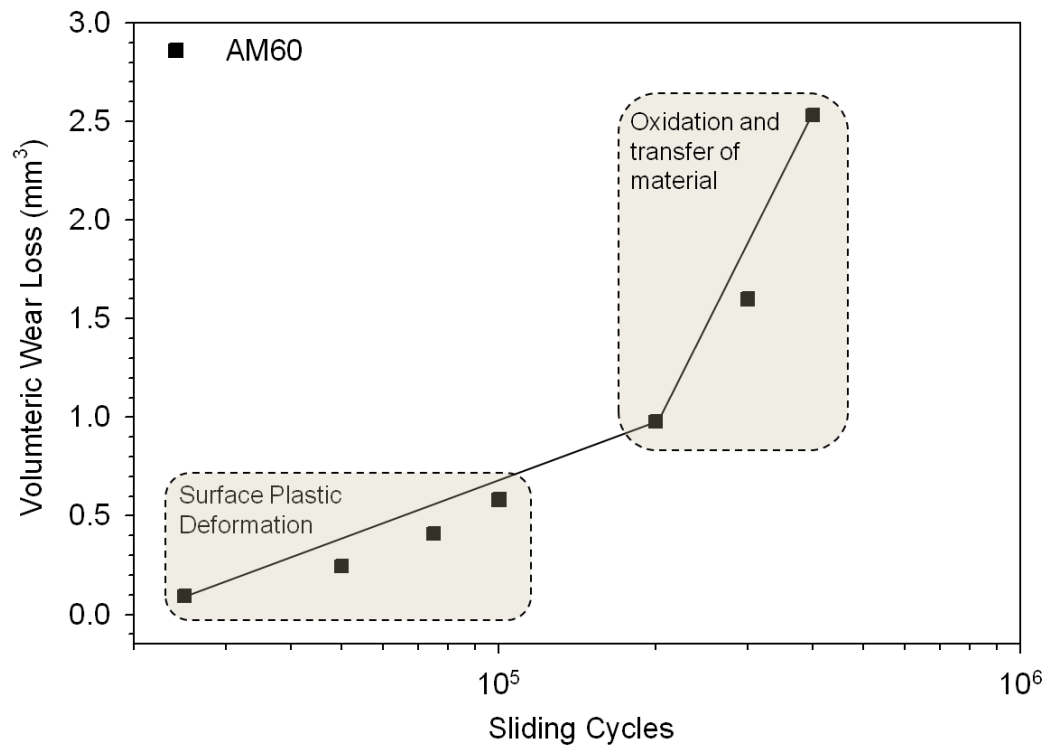


Fig.4.3. Volumetric wear loss vs. sliding cycles plot for AM60 alloy at 1.0 N load indicating presence of two wear regimes: wear by surface plastic deformation and wear by oxidation and adhesion.

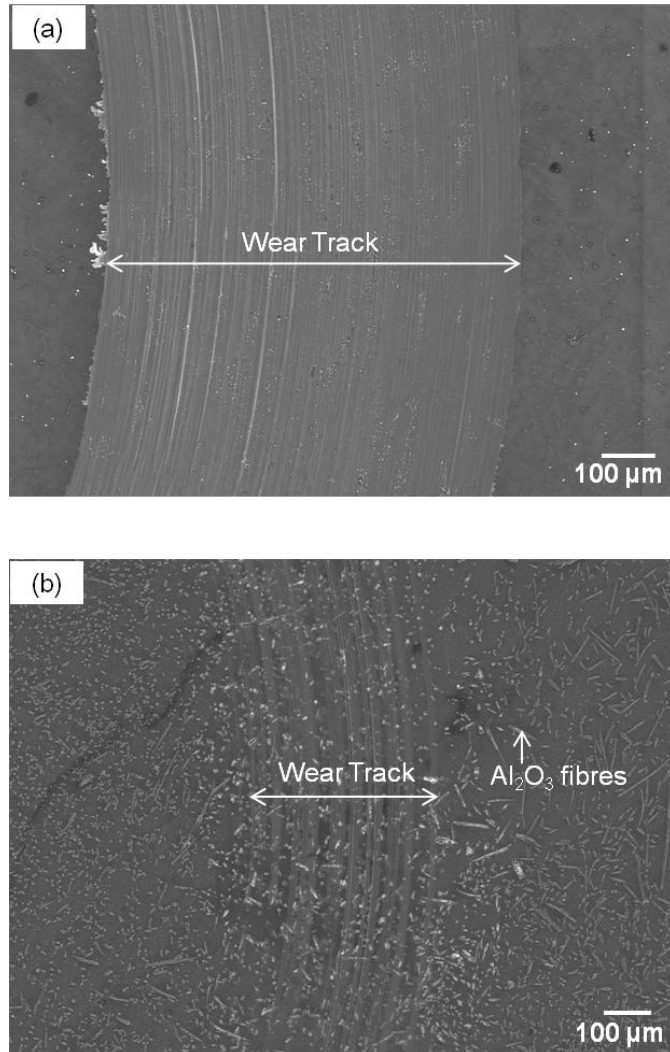


Fig.4.4. SEM micrographs showing the difference in the width of wear tracks of (a) AM60 alloy at 1.0 N and  $2.5 \times 10^4$  cycles and (b) AM60-9%  $(\text{Al}_2\text{O}_3)_f$  at 2.0 N and  $6 \times 10^5$  cycles indicating the wear resistance of the ceramic reinforced composite is higher than the alloy.

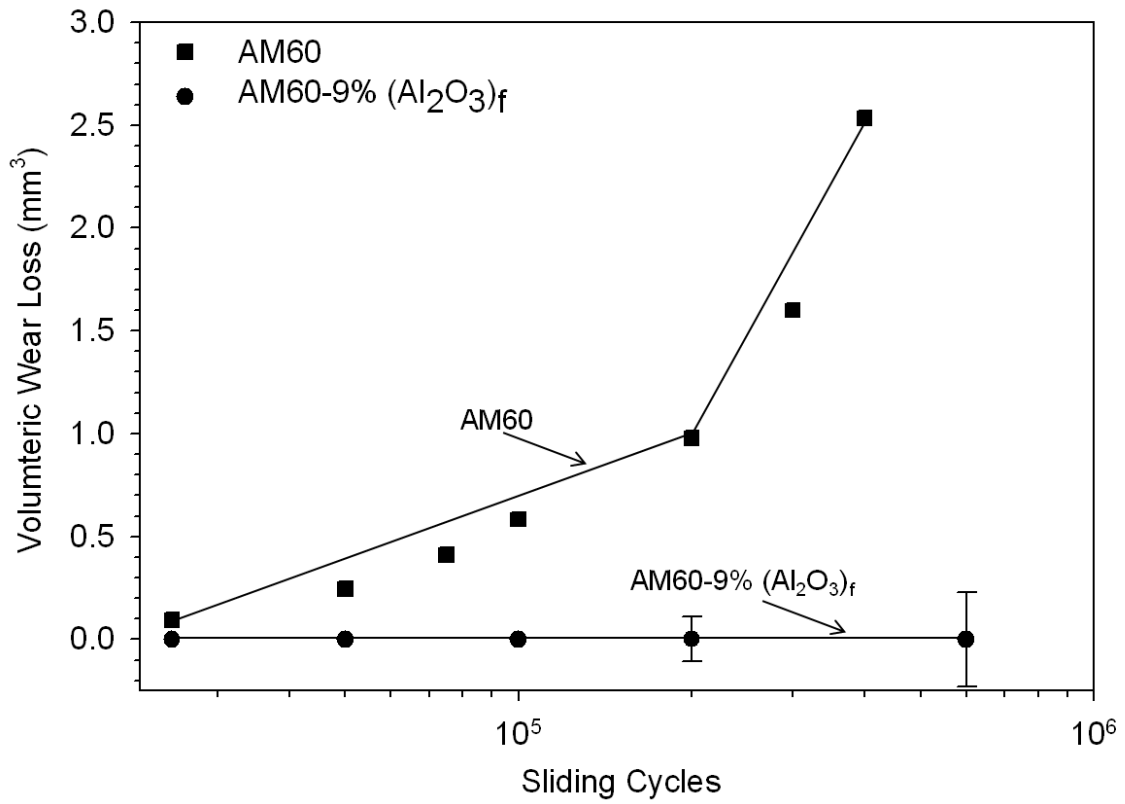


Fig.4.5. Volumetric wear loss vs. sliding cycles plot for AM60 alloy and AM60-9% (Al<sub>2</sub>O<sub>3</sub>)<sub>f</sub>. The wear loss of the composite is 10<sup>2</sup> times lower than that of the matrix alloy. Note the wear of the composite was shown at 5.0 N and the matrix at 1.0 N load in order to emphasize the higher wear resistance of the composite AM60-9% (Al<sub>2</sub>O<sub>3</sub>)<sub>f</sub> compared to AM60 alloy.

### 4.3. Comparison of Wear of AM60-(9% (Al<sub>2</sub>O<sub>3</sub>)<sub>f</sub> + 4% (Al<sub>2</sub>O<sub>3</sub>)<sub>p</sub>) and AM60-9% (Al<sub>2</sub>O<sub>3</sub>)<sub>f</sub>

Prior to the wear tests, contact surfaces of AM60-(9% (Al<sub>2</sub>O<sub>3</sub>)<sub>f</sub> + 4% (Al<sub>2</sub>O<sub>3</sub>)<sub>p</sub>) and AM60-9% (Al<sub>2</sub>O<sub>3</sub>)<sub>f</sub> were chemically etched (2% nital solution for 60 s) to expose the Al<sub>2</sub>O<sub>3</sub> fibres (2.79±0.12 µm) above the Mg matrix. Sliding wear on AM60-(9% (Al<sub>2</sub>O<sub>3</sub>)<sub>f</sub> + 4% (Al<sub>2</sub>O<sub>3</sub>)<sub>p</sub>) and AM60-9% (Al<sub>2</sub>O<sub>3</sub>)<sub>f</sub> at 1.0 N revealed no damage to the contact surfaces as the Mg matrix was protected by the exposed Al<sub>2</sub>O<sub>3</sub> fibres. At 2.0 N load and upto 1.0×10<sup>5</sup> sliding cycles, no volumetric wear loss (by optical profilometry measurements) could be detected from the AM60-(9% (Al<sub>2</sub>O<sub>3</sub>)<sub>f</sub> + 4% (Al<sub>2</sub>O<sub>3</sub>)<sub>p</sub>) or AM60-9% (Al<sub>2</sub>O<sub>3</sub>)<sub>f</sub> as the counterface made no contact with the Mg matrix. Effects of wear could be identified only in the form of scratches on the tops of Al<sub>2</sub>O<sub>3</sub> particles and fibres.

At 5.0 N load both AM60-(9% (Al<sub>2</sub>O<sub>3</sub>)<sub>f</sub> + 4% (Al<sub>2</sub>O<sub>3</sub>)<sub>p</sub>) and AM60-9% (Al<sub>2</sub>O<sub>3</sub>)<sub>f</sub> showed zero volumetric loss up to 5.0×10<sup>4</sup> cycles. Surface damage occurred in the following ways: i) Al<sub>2</sub>O<sub>3</sub> fibres underwent fracture and fragmentation while still attached to the matrix and ii) reduction in height of alumina particles and fibres with increasing sliding cycles due to Al<sub>2</sub>O<sub>3</sub> sinking in. The applied load was carried by the Al<sub>2</sub>O<sub>3</sub> particles and fragmented fibres, thus protecting the Mg-matrix from damage. However, after 1.0×10<sup>5</sup> sliding cycles and 5.0 N load, the AM60-9% (Al<sub>2</sub>O<sub>3</sub>)<sub>f</sub> exhibited damage to the Mg-matrix in the form of wear grooves (Fig.4.6a) whereas AM60-(9% (Al<sub>2</sub>O<sub>3</sub>)<sub>f</sub> + 4% (Al<sub>2</sub>O<sub>3</sub>)<sub>p</sub>) showed no damage to the matrix under the same conditions (Fig.4.6b).

At 5.0 N and after 1.0×10<sup>5</sup> sliding cycles, AM60-9% (Al<sub>2</sub>O<sub>3</sub>)<sub>f</sub> showed an increased amount of the volumetric loss (2.75×10<sup>-4</sup> mm<sup>3</sup>). Fig. 4.7 represents the method by which Al<sub>2</sub>O<sub>3</sub> elevation was determined. Fig.4.7a and b represent histograms, obtained

from optical profilometry measurements, indicating the reduction in  $\text{Al}_2\text{O}_3$  fibre and particle heights for wear of AM60-(9%  $(\text{Al}_2\text{O}_3)_f$  + 4%  $(\text{Al}_2\text{O}_3)_p$ ) and AM60-9%  $(\text{Al}_2\text{O}_3)_f$ . From Fig.4.7 it is observed that after  $1.0 \times 10^5$  cycles, the  $\text{Al}_2\text{O}_3$  elevation over the Mg matrix is by  $1.8 \pm 0.22 \mu\text{m}$  for AM60-(9%  $(\text{Al}_2\text{O}_3)_f$  + 4%  $(\text{Al}_2\text{O}_3)_p$ ) whereas the fibre and matrix elevation are the same for AM60-9%  $(\text{Al}_2\text{O}_3)_f$ . Fig.4.7c is the plot of the  $\text{Al}_2\text{O}_3$  height decrease with sliding cycles. The  $\text{Al}_2\text{O}_3$  fibre height diminished from  $2.8 \pm 0.20 \mu\text{m}$  to  $2.40 \pm 0.08 \mu\text{m}$  at the end of  $5.0 \times 10^4$  cycles and became the same as the Mg matrix height at the end of  $1.0 \times 10^5$  cycles (Fig.4.7) due to sinking in of the fragmented fibres. Once the fibre and the matrix were at the same elevation, the latter was exposed to damage by the counterface and wear occurred on both fibres and matrix resulting in a sudden increase in volumetric wear loss (Fig.4.8). On the other hand, AM60-(9%  $(\text{Al}_2\text{O}_3)_f$  + 4%  $(\text{Al}_2\text{O}_3)_p$ ) showed no damage to the matrix even after  $1.0 \times 10^5$  sliding cycles as the  $\text{Al}_2\text{O}_3$  fibres+particles, exposed by  $1.8 \pm 0.22 \mu\text{m}$  at the end of  $1.0 \times 10^5$  cycles (Fig.4.7), effectively protected the matrix from damage by counterface. The decrease in the height of the  $\text{Al}_2\text{O}_3$  fibres and particles with increasing sliding cycles and applied load leading to changes in the damage features is summarized by the plot of volumetric wear loss vs. sliding cycles (Fig.4.8). No matrix damage (zero volumetric loss) occurred as long as the fibre/fibre+ particle were elevated over the Mg-matrix.

In summary, wear at 1.0 N and 2.0 N, for both composites AM60-(9%  $(\text{Al}_2\text{O}_3)_f$  + 4%  $(\text{Al}_2\text{O}_3)_p$ ) and AM60-9%  $(\text{Al}_2\text{O}_3)_f$  exhibited zero volumetric wear loss for all the test cycles ( $\leq 2 \times 10^5$  cycles). At 5.0 N load AM60-(9%  $(\text{Al}_2\text{O}_3)_f$  + 4%  $(\text{Al}_2\text{O}_3)_p$ ) corresponded to zero volumetric wear loss whereas AM60-9%  $(\text{Al}_2\text{O}_3)_f$  resulted in an increased volumetric wear after  $1.0 \times 10^5$  sliding cycles. The damage features of these fibre

reinforced composites studied at longer sliding cycles and also at elevated temperature are presented in the following sections.

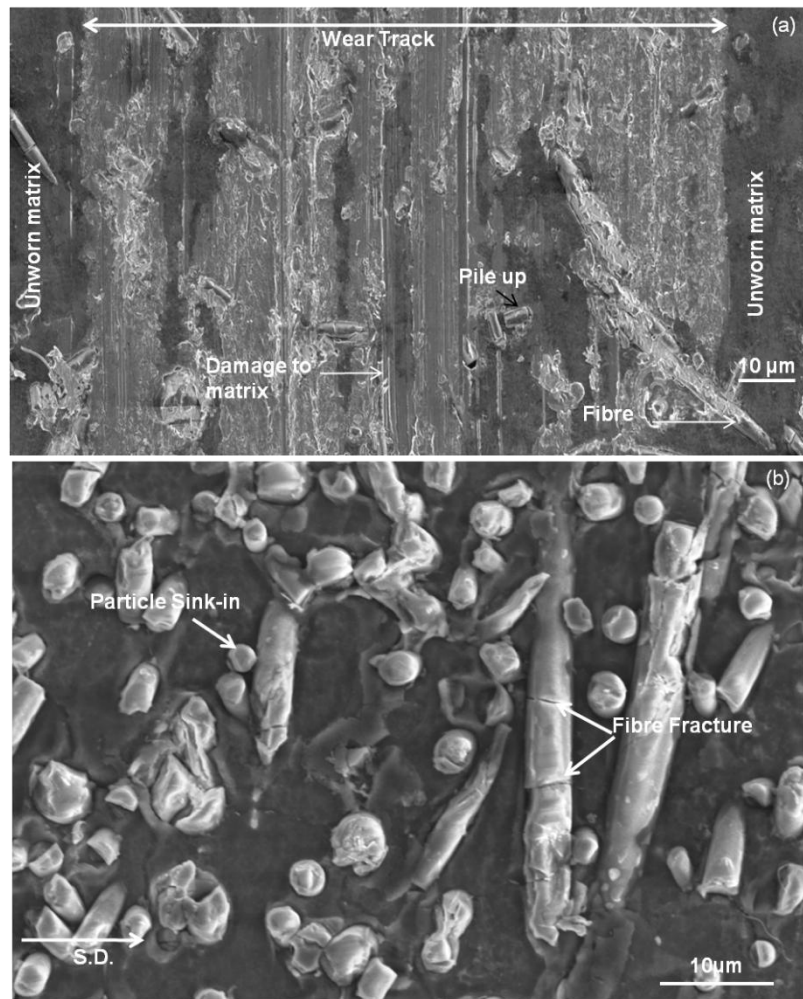
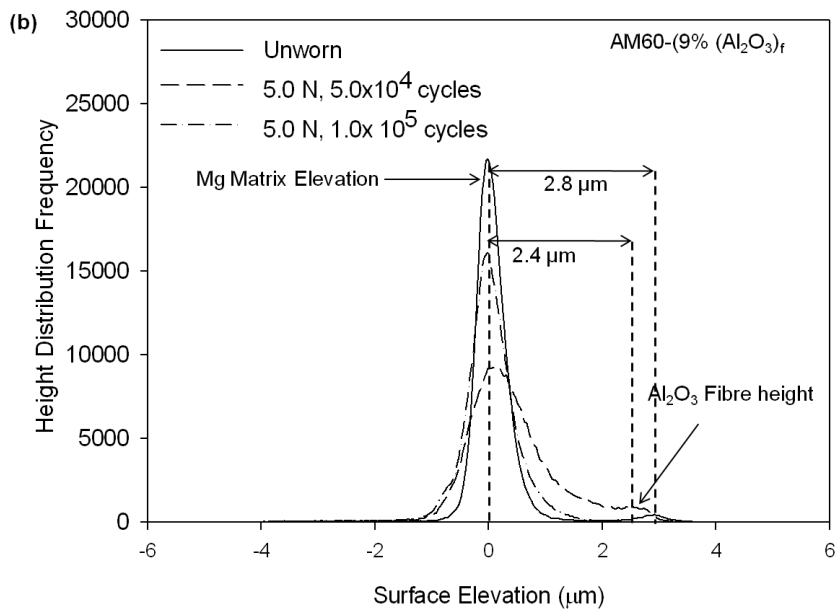
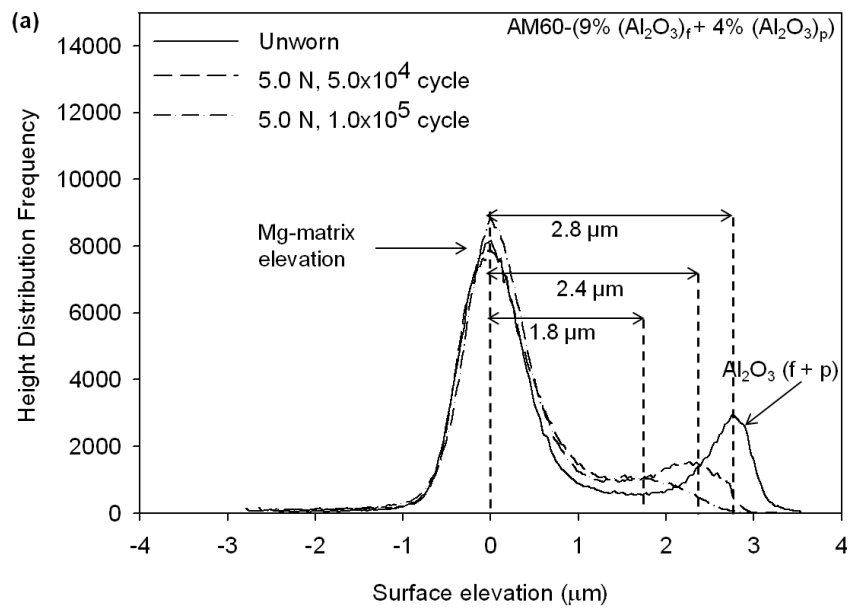


Fig.4.6. a) SEM micrograph at 500X magnification showing the morphology of worn surface AM60-9% (Al<sub>2</sub>O<sub>3</sub>)<sub>f</sub> after 1.0×10<sup>5</sup>cycles indicating presence of wear grooves; b) SEM micrograph at 1000X magnification showing morphology of worn surface of AM60-(9% (Al<sub>2</sub>O<sub>3</sub>)<sub>f</sub> + 4% (Al<sub>2</sub>O<sub>3</sub>)<sub>p</sub>) after 1.0×10<sup>5</sup>cycles indicating no damage to Mg matrix.



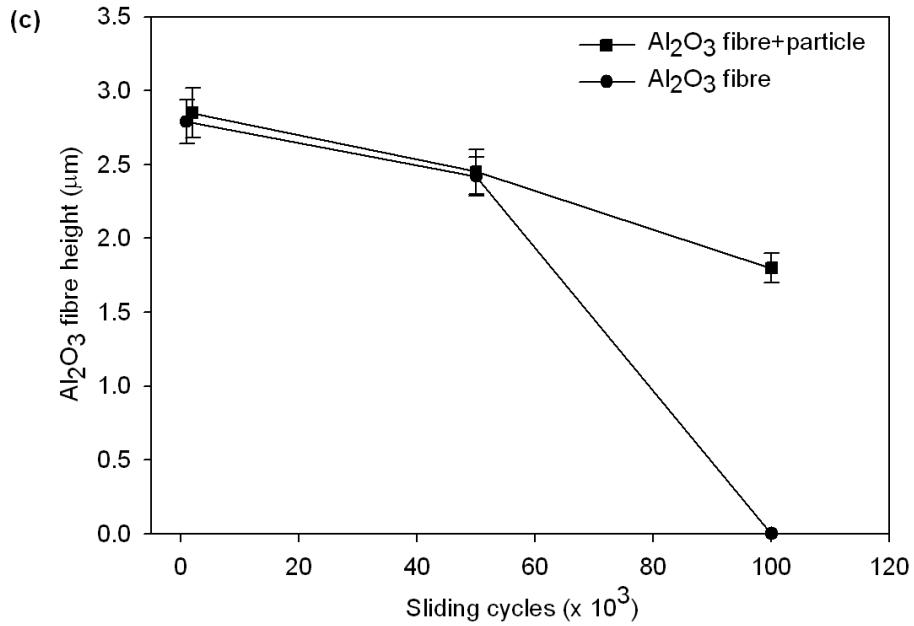


Fig.4.7. (a) and (b) represent histogram plot for AM60-(9% (Al<sub>2</sub>O<sub>3</sub>)<sub>f</sub> + 4% (Al<sub>2</sub>O<sub>3</sub>)<sub>p</sub>) and AM60-9% (Al<sub>2</sub>O<sub>3</sub>)<sub>f</sub> respectively under etched conditions with an initial elevation of Al<sub>2</sub>O<sub>3</sub> by 2.8±0.20 µm, obtained from optical profilometry measurements. It is shown that after 1.0×10<sup>5</sup> sliding cycles the Al<sub>2</sub>O<sub>3</sub> fibres+particles (f+p) were exposed by 1.8±0.22 µm for AM60-(9% (Al<sub>2</sub>O<sub>3</sub>)<sub>f</sub> + 4% (Al<sub>2</sub>O<sub>3</sub>)<sub>p</sub>) while the Al<sub>2</sub>O<sub>3</sub> fibres were at the same elevation as that of the Mg matrix for AM60-9% (Al<sub>2</sub>O<sub>3</sub>)<sub>f</sub>. (c) is the plot of fibre height decrease against number of sliding cycles at 5.0 N load.



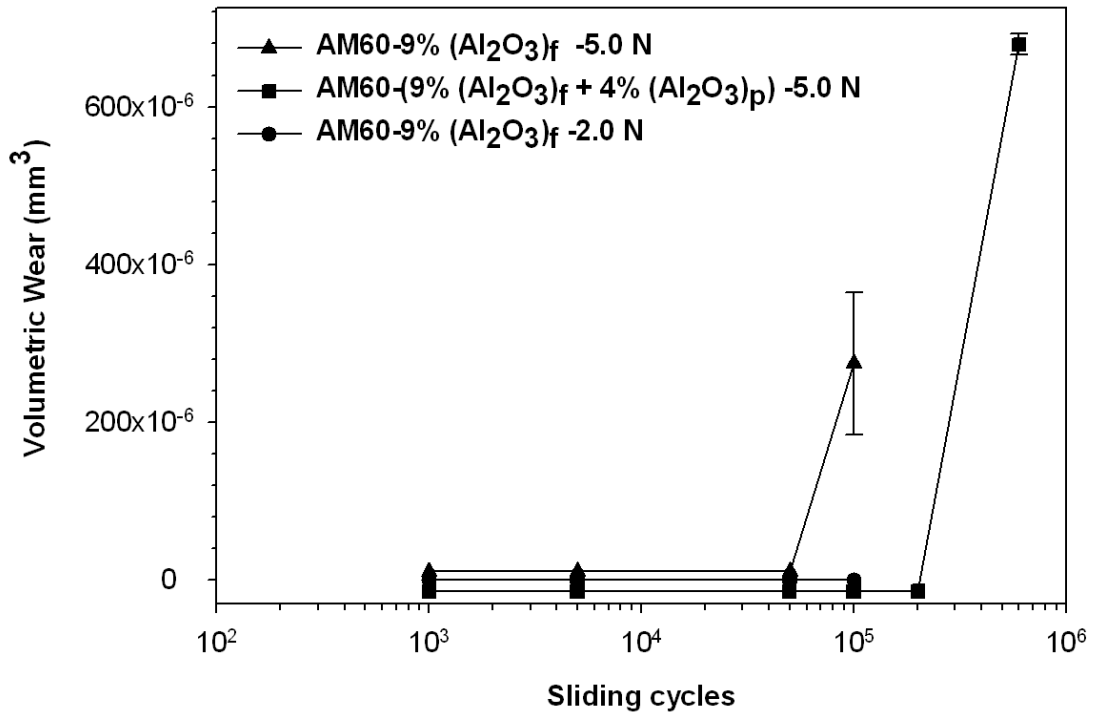


Fig.4.8. Plot of volumetric wear of AM60-9% (Al<sub>2</sub>O<sub>3</sub>)<sub>f</sub> and AM60-(9% (Al<sub>2</sub>O<sub>3</sub>)<sub>f</sub> + 4% (Al<sub>2</sub>O<sub>3</sub>)<sub>p</sub>) with increasing sliding cycles. In case of AM60-9% (Al<sub>2</sub>O<sub>3</sub>)<sub>f</sub> it is evident that at 2.0 N load the transition to higher volumetric wear loss occurs at 2.0x10<sup>5</sup> sliding cycles while at 5.0 N load it occurs after 1.0x10<sup>5</sup> cycles. However, for AM60-(9% (Al<sub>2</sub>O<sub>3</sub>)<sub>f</sub> + 4% (Al<sub>2</sub>O<sub>3</sub>)<sub>p</sub>) zero volumetric wear loss is observed after 1.0x10<sup>5</sup> cycles at 1.0 N load indicating higher wear resistance compared to AM60-9% (Al<sub>2</sub>O<sub>3</sub>)<sub>f</sub>.

#### 4.4. Wear of Mg composites reinforced with different volume percentages of Al<sub>2</sub>O<sub>3</sub> fibres

In order to further the understanding of wear mechanisms of fibre reinforced Mg composites, pin-on-disk wear tests were performed on Mg composites reinforced with 9 vol%, 11 vol% and 26 vol% Al<sub>2</sub>O<sub>3</sub> fibres.

The wear of AM60-9% (Al<sub>2</sub>O<sub>3</sub>)<sub>f</sub> was limited to the tops of the Al<sub>2</sub>O<sub>3</sub> fibres without any damage to the matrix for up to  $6 \times 10^5$  sliding cycles. For sliding cycles  $\geq 6 \times 10^5$ , the damage to the Mg matrix was observed in the form of surface plastic deformation and formation of wear grooves (Fig.4.9a). For AM60-11% (Al<sub>2</sub>O<sub>3</sub>)<sub>f</sub>, wear was observed in the form of damage to the matrix by wear groove formation (Fig.4.9b). However, damage to the Mg matrix and subsequent material loss in AM60-11% (Al<sub>2</sub>O<sub>3</sub>)<sub>f</sub> was approximately 2.8 times less when compared with the damage observed in the case of AM60-9% (Al<sub>2</sub>O<sub>3</sub>)<sub>f</sub> after  $6 \times 10^5$  sliding cycles. For AM60-26% (Al<sub>2</sub>O<sub>3</sub>)<sub>f</sub> almost no damage to the Mg matrix was detected after testing for  $6 \times 10^5$  sliding cycles. Damage features consisted of Al<sub>2</sub>O<sub>3</sub> fibre fracture, fibre height decrease due to the wear of the tops of fibres and magnesium pile up formation adjacent to the fibres. An increase in the volumetric wear loss of AM60-26% (Al<sub>2</sub>O<sub>3</sub>)<sub>f</sub> from 0 to  $2.3 \times 10^{-4}$  mm<sup>3</sup> was observed (Fig.4.10) after  $1 \times 10^6$  sliding cycles due to damage of the Mg matrix and wear groove formation (Fig.4.9c).

Fig.4.10 shows that the transition to a high rate of material loss was deferred from  $6.0 \times 10^5$  cycles to  $\geq 8.0 \times 10^5$  cycles and  $\geq 1.0 \times 10^6$  cycles as the fibre volume percentage was increased from 9% to 11% and 26% respectively. This might be attributed to the smaller average reduction in Al<sub>2</sub>O<sub>3</sub> fibre height, with increasing the fibre volume fraction

as indicated in Table 4-1. The  $\text{Al}_2\text{O}_3$  fibres, initially protruded over the Mg matrix by  $1.80 \pm 0.18 \mu\text{m}$ , and acted as load bearing elements, protecting the Mg matrix from damage. As the fibre height decreased with increasing sliding cycles (Table 4-1) the damage to the Mg matrix and the subsequent rate of material loss increased (Fig.4.10). The decrease in  $\text{Al}_2\text{O}_3$  fibre elevation was delayed for AM60-26%  $(\text{Al}_2\text{O}_3)_f$  as compared to AM60-9%  $(\text{Al}_2\text{O}_3)_f$  and AM60-11%  $(\text{Al}_2\text{O}_3)_f$ , as indicated in Table 4-1 resulting in reduced volumetric wear loss (Fig.4.10). The reduced rate of material of material loss in case of AM60-11%  $(\text{Al}_2\text{O}_3)_f$  as compared to AM60-9%  $(\text{Al}_2\text{O}_3)_f$  after  $6 \times 10^5$  sliding cycle could be attributed to the higher matrix hardness of the former ( $102.60 \pm 2.9 \text{ HV}$ ) than the latter ( $90.8 \pm 4.8 \text{ HV}$ ). The higher hardness of AM60-11%  $(\text{Al}_2\text{O}_3)_f$  over AM60-9%  $(\text{Al}_2\text{O}_3)_f$  might be due to the greater amount of matrix hardening as a result of greater amount of  $\text{Al}_2\text{O}_3$  fibre reinforcement. This led to an increase in the dislocation density due to a geometrical and thermal mismatch between the matrix and reinforcement along with reduced grain size resulting in strengthening the Mg matrix.

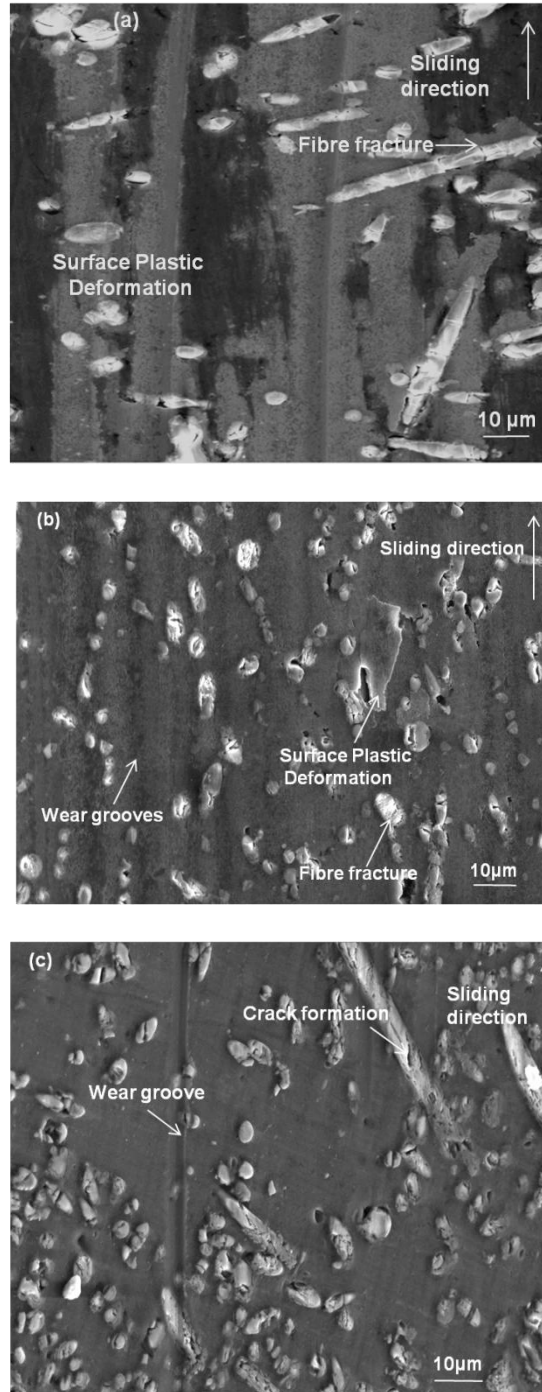


Fig.4.9. SEM micrographs in secondary electron mode illustrating the worn surfaces at 2.0 N and after  $1 \times 10^6$  cycles of (a) AM60-9% (Al<sub>2</sub>O<sub>3</sub>)<sub>f</sub> indicating fibre fracture and extensive plastic deformation of Mg matrix; (b) AM60-11% (Al<sub>2</sub>O<sub>3</sub>)<sub>f</sub> indicating damage in the form of wear grooves; (c) AM60-26% (Al<sub>2</sub>O<sub>3</sub>)<sub>f</sub> showing almost no damage to matrix.

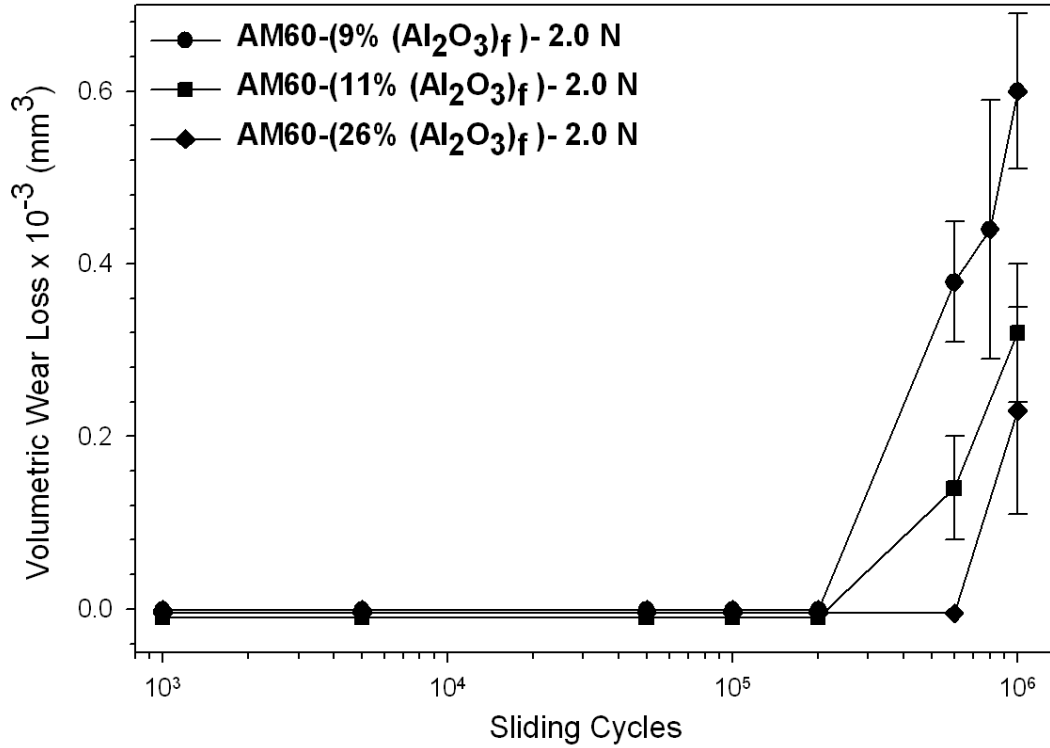


Fig. 4.10. Volumetric material loss vs. sliding cycles at 2.0 N load indicating the effect of  $Al_2O_3$  fibre volume percentage on the transition to higher rate of material removal of the composite. It is to be noted that the transition to higher volumetric wear loss was delayed to  $1 \times 10^6$  cycles for AM60-26%  $(Al_2O_3)_f$  as opposed to  $6 \times 10^5$  cycles for AM60-9%  $(Al_2O_3)_f$  and AM60-11%  $(Al_2O_3)_f$ .

Table 4-1: Al<sub>2</sub>O<sub>3</sub> fibre elevation over the Mg matrix for the composites after 6×10<sup>5</sup> sliding cycles.

	AM60-9% (Al <sub>2</sub> O <sub>3</sub> ) <sub>f</sub>	AM60-11% (Al <sub>2</sub> O <sub>3</sub> ) <sub>f</sub>	AM60-26% (Al <sub>2</sub> O <sub>3</sub> ) <sub>f</sub>
Average fibre elevation (μm)	0.48±0.08	0.58±0.12	0.70±0.02

#### 4.5. Wear of Composite: AM60-9% (Al<sub>2</sub>O<sub>3</sub>)<sub>f</sub> at 25 °C and 100 °C

##### 4.5.1 Decrease in height of Al<sub>2</sub>O<sub>3</sub> fibres at 25 °C and 100 °C

The fibre height decrease was determined using optical profilometry measurements caused by sinking in of the comminuted fibres. The fibre height decrease data are summarized in Fig.4.11. It is evident that fibre height decreases with increasing sliding cycles from the initial  $1.80 \pm 0.18 \mu\text{m}$  to  $0.8 \pm 0.1 \mu\text{m}$  at 1.0 N load and after  $1 \times 10^6$  sliding cycles. The fibre height reduction was delayed at a lower load of 2.0 N compared to 5.0 N where the Al<sub>2</sub>O<sub>3</sub> fibre reached the same height as that of the Mg matrix as early as  $1 \times 10^5$  sliding cycles.

A comparative plot (Fig.4.12) of the Al<sub>2</sub>O<sub>3</sub> fibre height decrease at 2.0 N and at 25 °C and 100 °C shows that, after sliding for  $8 \times 10^5$  cycles, the Al<sub>2</sub>O<sub>3</sub> fibres elevation was  $0.6 \pm 0.2 \mu\text{m}$  at 100 °C whereas at 25 °C it reached the same elevation as that of the Mg matrix. Thus at elevated temperature Al<sub>2</sub>O<sub>3</sub> fibres height decrease was delayed to longer sliding cycles.

##### 4.5.2. Comparison of damage features of AM60-9% (Al<sub>2</sub>O<sub>3</sub>)<sub>f</sub> at 25 °C and 100 °C

In the engine running conditions, the operating temperature is 100 °C; it is at this temperature that the viscosity of premium Mobil oil is also determined. Thus it would be useful to evaluate the wear behaviour of the Mg composite AM60-9% (Al<sub>2</sub>O<sub>3</sub>)<sub>f</sub> at 100 °C and compare it with that of the room temperature results.

At 1.0 N load and at 25 °C, the Al<sub>2</sub>O<sub>3</sub> fibres protruded over the Mg matrix by  $0.8 \mu\text{m}$  after  $1 \times 10^6$  sliding cycles as indicated in Fig.4.11. The wear was limited to the tops of the Al<sub>2</sub>O<sub>3</sub> fibres (Fig.4.13a) without any damage to the matrix. The Al<sub>2</sub>O<sub>3</sub> fibres thus protected the Mg matrix from damage by the counterface for up to the longest

sliding cycle ( $1 \times 10^6$ ). Hence, under 1.0 N load the material removal from the Mg matrix was essentially nil for all sliding cycles which was reflected as zero wear rate in the volumetric wear loss plot (Fig. 4.14). A high magnification image of the worn surfaces at 1.0 N load indicates the fibre sinking in and corresponding Mg matrix pile up. Similar features were observed at 2.0 N load for upto  $2 \times 10^5$  sliding cycles. For cycles  $\geq 6 \times 10^5$ , wear damage to the matrix surface was observed in the form of wear grooves (Fig.4.13c). Consequently, at this point the wear rate increased from 0 to  $1.35 \times 10^{-7}$  mm<sup>3</sup>/m as shown in Fig. 4.12. At 5.0 N load the Mg matrix damage incurred as early as  $1 \times 10^5$  sliding cycles. Fig.4.13d shows fibre fracture and decohesion from the matrix on the Mg matrix by the counterface after  $1 \times 10^5$  sliding cycles and 5.0 N load. Fig. 4.15 indicates the damage features observed during wear of AM60-9% (Al<sub>2</sub>O<sub>3</sub>)<sub>f</sub> at 25°C and under 2.0 N load. Fig. 4.15a and b indicates worn surface of AM60-9% (Al<sub>2</sub>O<sub>3</sub>)<sub>f</sub> after  $2 \times 10^5$  sliding cycles at 2.0 N load. In Fig. 4.15a the damage features comprise of fragmented Al<sub>2</sub>O<sub>3</sub> fibres, sunk in fibres and corresponding pile up of the Mg matrix; the fibre elevation being  $1.50 \pm 0.08$  μm. Fig. 4.15b represents the worn surface after  $6 \times 10^5$  sliding cycles where, in addition to fibre fragmentation and sink in, surface plastic deformation is also observed- the fibre elevation being  $0.50 \pm 0.02$  μm.

The plot of volumetric wear loss against the sliding cycles at three different loads (Fig. 4.14) helped explain the material removal rates and the damage features at each load when examined together with the SEM images (Fig.4.13) of worn contact surfaces and the Al<sub>2</sub>O<sub>3</sub> fibres height decrease plot (Fig.4.11). At higher loads and sliding cycles, the material removal rate was considerably high and the wear rate was found to increase cumulatively. At 2.0 N load the fibre height decreased from 1.8 to 0.5 μm after  $6 \times 10^5$



sliding cycles, causing wear of the Mg matrix which matched the increased rate of material removal indicated in Fig.4.14. Thus Fig.4.11 provides a way of predicting the onset of damage to the Mg matrix for the composite AM60-9% (Al<sub>2</sub>O<sub>3</sub>)<sub>f</sub> as represented in Fig.4.16. In Fig.4.16 it can be seen that the decrease in fibre height after 6×10<sup>5</sup> cycles corresponds to the increase in volumetric wear loss. Once damage to the Mg matrix was initiated the counterface abraded the relatively softer Mg matrix causing plastic deformation of the surface.

In the case of wear tests performed at 100 °C, at 1.0 N load there was no damage to matrix after 1×10<sup>6</sup> sliding cycles akin to the results obtained for the room temperature tests. However, the decrease in fibre height was less compared to that at room temperature after 1×10<sup>6</sup> sliding cycles; at 100 °C and 1.0 N load the fibre height decreased from the initial 1.8 μm to 1.0±0.2 μm after 1×10<sup>6</sup> sliding cycles. Electron microscopic analyses of the worn surfaces indicated the formation of a tribofilm on top of the worn Al<sub>2</sub>O<sub>3</sub> fibres (Fig.4.17a). This tribofilm consisted of Zn, S, P and Ca (Fig.4.17b) all of which originated from the additives present in the lubricating oil used. The formation of similar tribofilm has been previously reported in study of UMW of Al-Si alloys at elevated temperature [62]. At 2.0 N load, damage to the matrix occurred not before 8.0×10<sup>5</sup> cycles where the Al<sub>2</sub>O<sub>3</sub> fibre elevation was 0.6 μm over the Mg matrix. However, at 25 °C as the cycles extended to 8.0×10<sup>5</sup>, the Al<sub>2</sub>O<sub>3</sub> fibre elevation decreased to the same level.

For the tests conducted at 2.0 N load and at 100 °C, the formation of the protective tribofilm, also termed as the Oil Residue layer (ORL) [11], was not restricted to tops of worn fibres. At this load, the tribolayer formation was detected throughout the

wear track (Fig.4.17c). Fig.4.18 compared the volumetric wear loss from AM60-9%  $(Al_2O_3)_f$  under 2.0 N load at 25 °C and 100 °C. The plot showed that the rate of material loss from AM60-9%  $(Al_2O_3)_f$  at high temperature was lower than that at room temperature which might be attributed to the formation of a tribolayer initially on the tops of fibres and eventually on the worn Mg matrix. The backscattered SEM images (Fig.4.19) indicated that the ORL formation was only detected at high temperature while no such layer could be observed on the worn surfaces of composites tested at room temperature. The ORL formation is thus responsible for reducing and postponing the damage to the Mg matrix for the composites tested at 100 °C as compared to those tested at 25 °C. Note that the ORL formed on the worn surfaces is derived from the additives present in the lubricant Mobil Oil 5W-30 and is thus specific to the lubricant that is being used. If the test lubricant was to be changed to base oil (without additives), the wear results are expected to change.

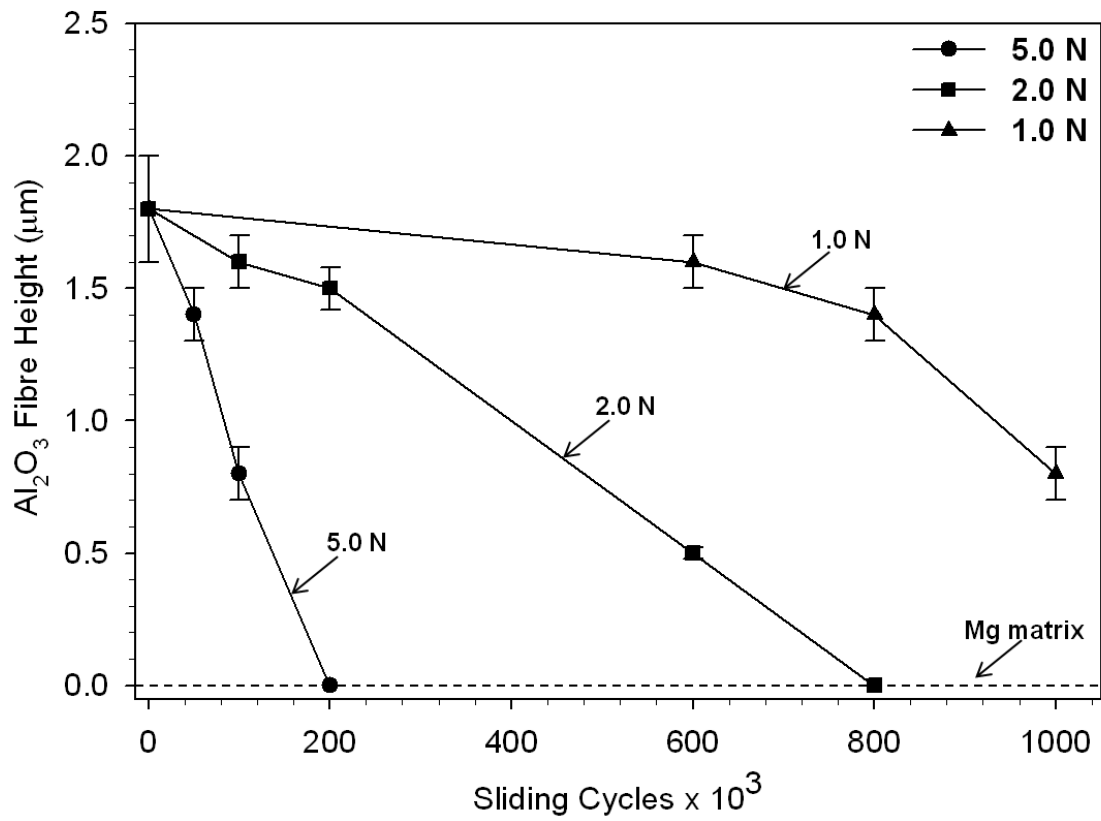


Fig.4.11. Plot of variation of Al<sub>2</sub>O<sub>3</sub> fibre height with sliding cycles at 1.0 N, 2.0 N and 5.0 N for AM60-9% (Al<sub>2</sub>O<sub>3</sub>)<sub>f</sub> composite at 25 °C. The fiber height reduction was delayed with decreasing load.

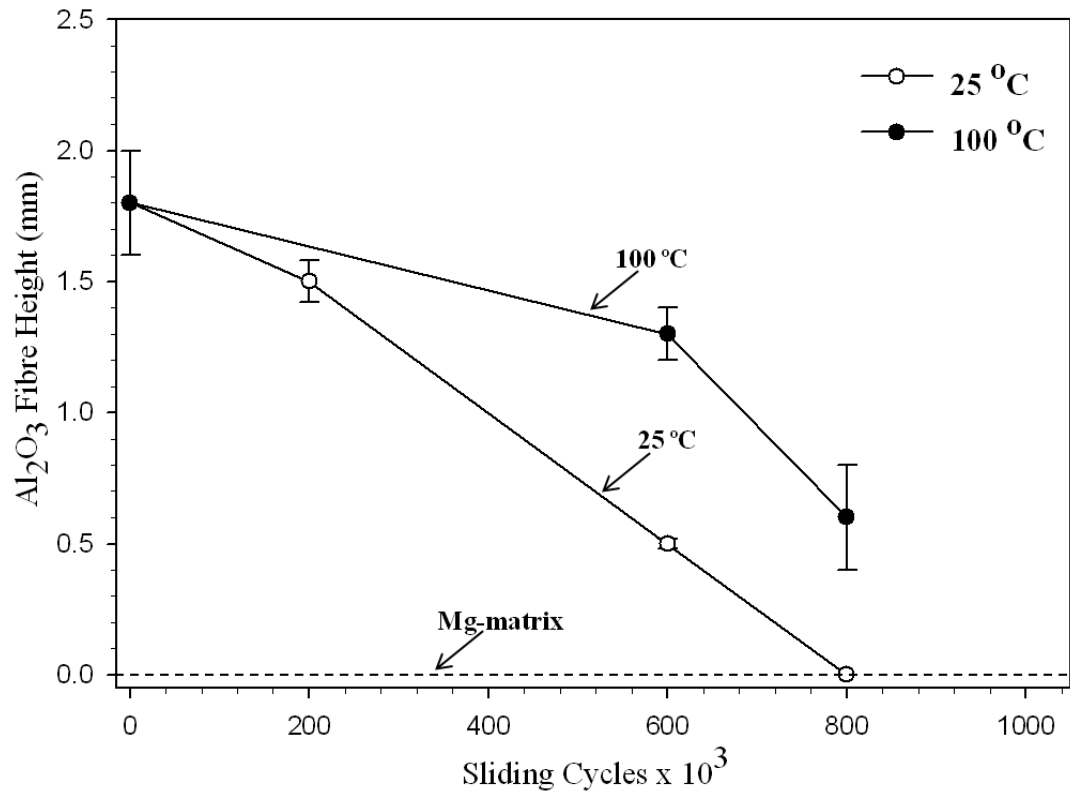
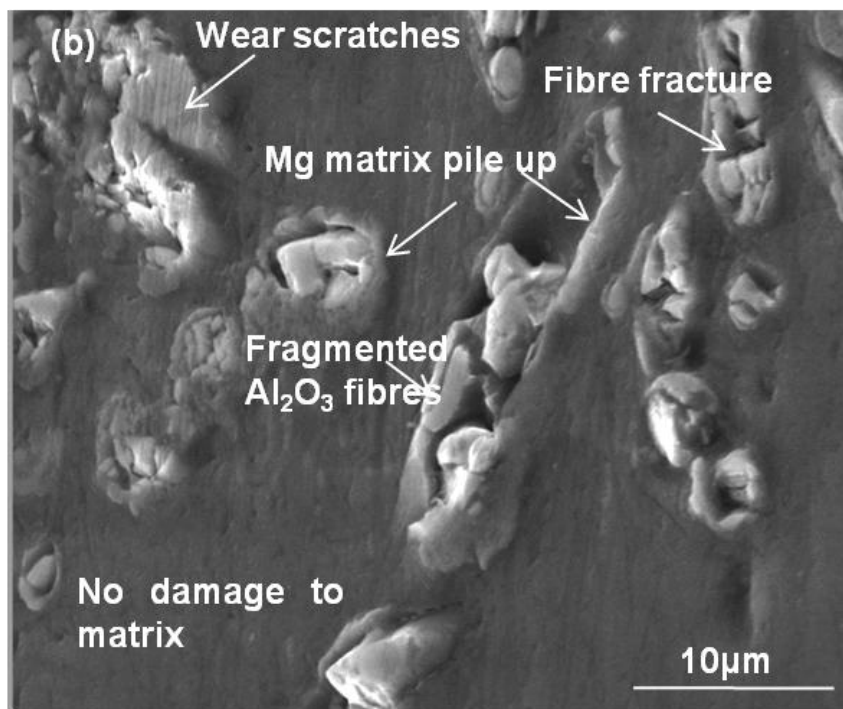
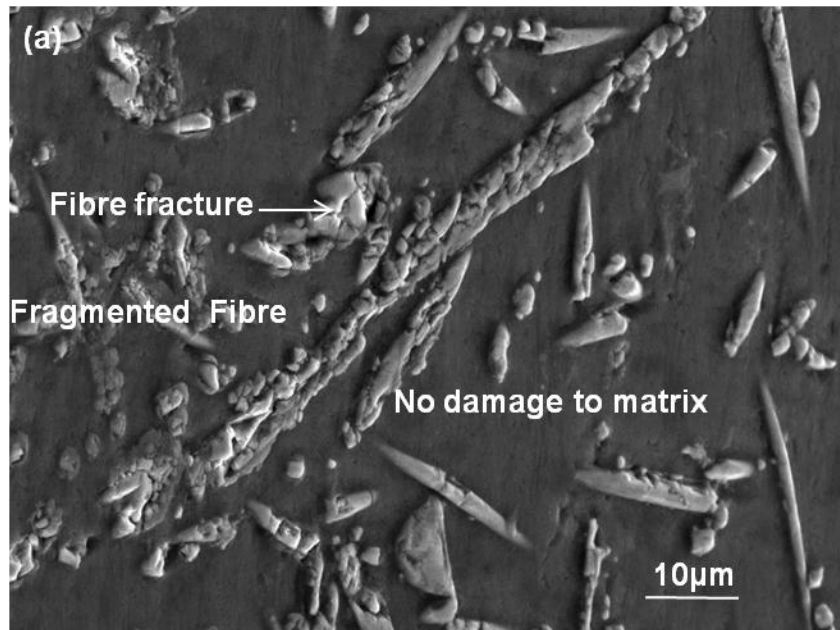


Fig.4.12. Plot of variation of Al<sub>2</sub>O<sub>3</sub> fibre height with sliding cycles at 25 °C and 100 °C under 2.0 N load for AM60-9% (Al<sub>2</sub>O<sub>3</sub>)<sub>f</sub> composite. The fiber height reduction is less in case of elevated temperature tests.



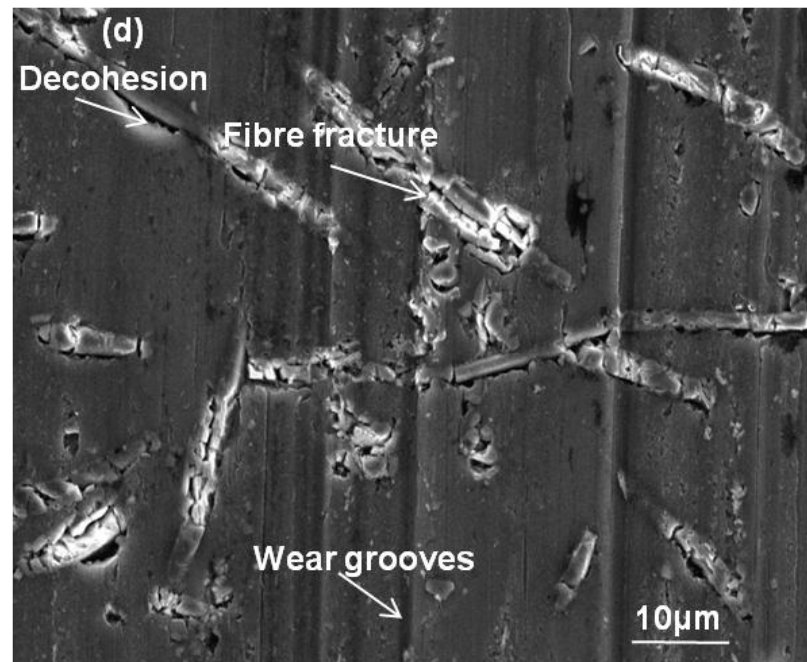
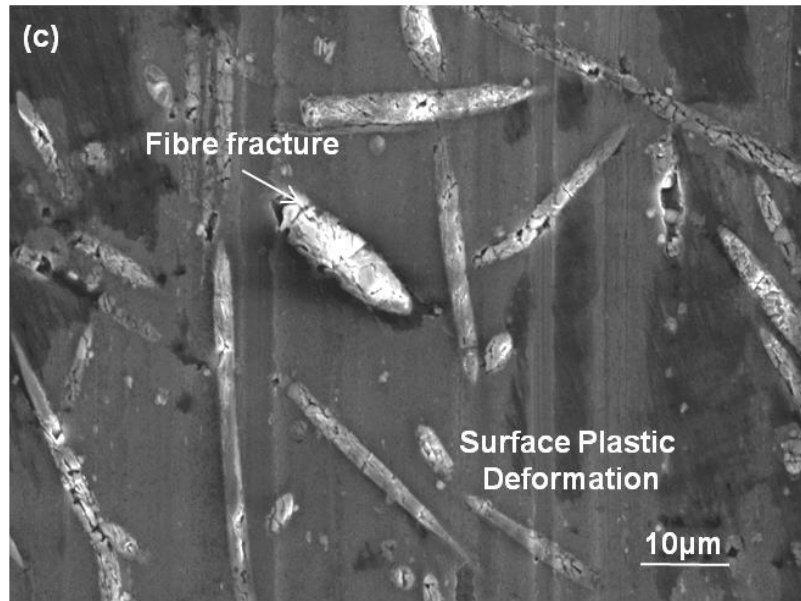


Fig.4.13. SEM micrographs of AM60-9% (Al<sub>2</sub>O<sub>3</sub>)<sub>f</sub> at room temperature and at 1.0 N, 2.0 N and 5.0 N. (a) No damage to matrix after 8.0×10<sup>5</sup> cycles under 1.0 N load; (b) High magnification image at 1.0 N load and 8.0×10<sup>5</sup> cycles indicating: i) fibre fracture and fragmentation ii) sinking in of the fragmented fibres iii) pile up of the adjacent Mg matrix without any damage to matrix; (c) Damage to the matrix in the form of wear grooves along with deformation of the Mg matrix at 2.0 N and after 8.0×10<sup>5</sup> cycles; (d) Damage to Mg matrix in the form of wear grooves as early as 1×10<sup>5</sup> cycles at 5.0 N load.

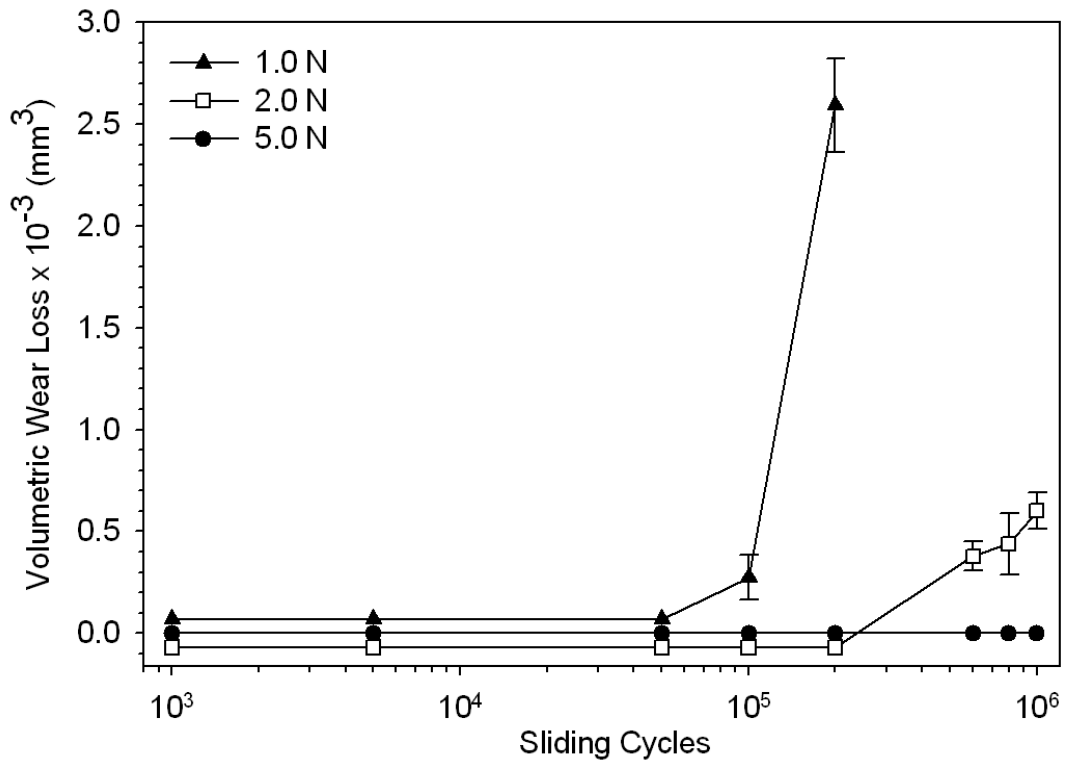
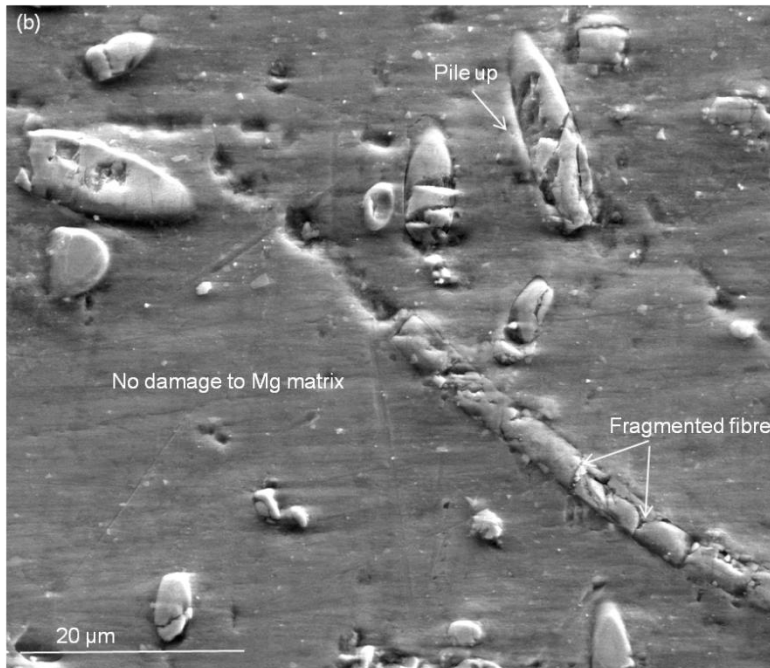
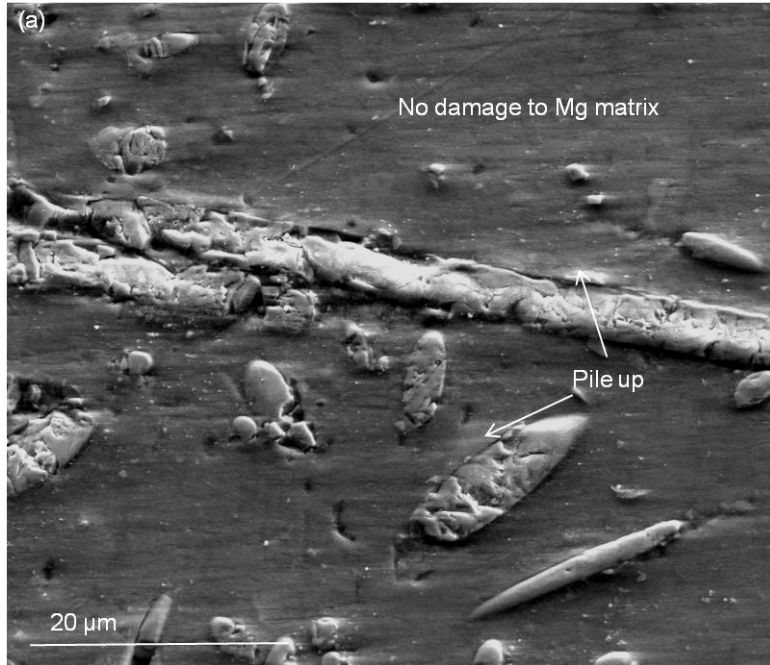


Fig.4.14. Volumetric wear loss vs. sliding cycles plot of AM60-9% (Al<sub>2</sub>O<sub>3</sub>)<sub>f</sub> at 1.0 N, 2.0 N and 5.0 N load at 25 °C. The transition to higher volumetric wear loss was delayed as the applied load was reduced- at 5.0 N the transition occurred at 1×10<sup>5</sup> cycles, at 2.0 N the transition occurred at 6×10<sup>5</sup> cycles while at 1.0 N zero volumetric wear continued for the highest sliding cycles tested 1×10<sup>6</sup> cycles. In the initial cycles fiber fracture preceded sinking in with no damage to the matrix. At higher sliding cycles damage to the Mg matrix by the counterface was observed.





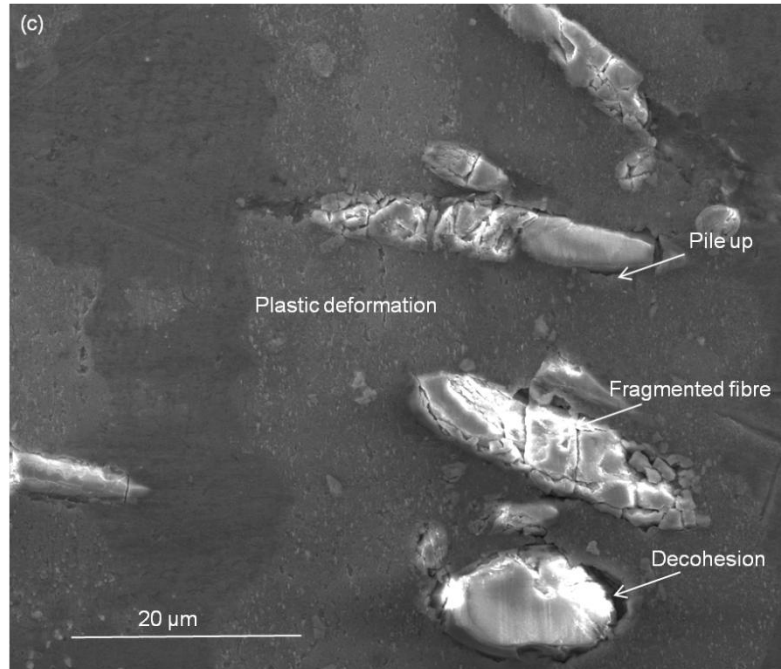


Fig.4.15. SEM micrographs (secondary electron mode) of worn surface of AM60-9%  $(Al_2O_3)_f$  at 2.0 N load. (a) and (b) represents worn surfaces after  $2 \times 10^5$  cycles showing damage features including fibre fragmentation, sink in and Mg matrix pile up- without damage to matrix. (c) represents worn surface after  $6 \times 10^5$  cycles indicating damage to the matrix in form of plastic deformation.

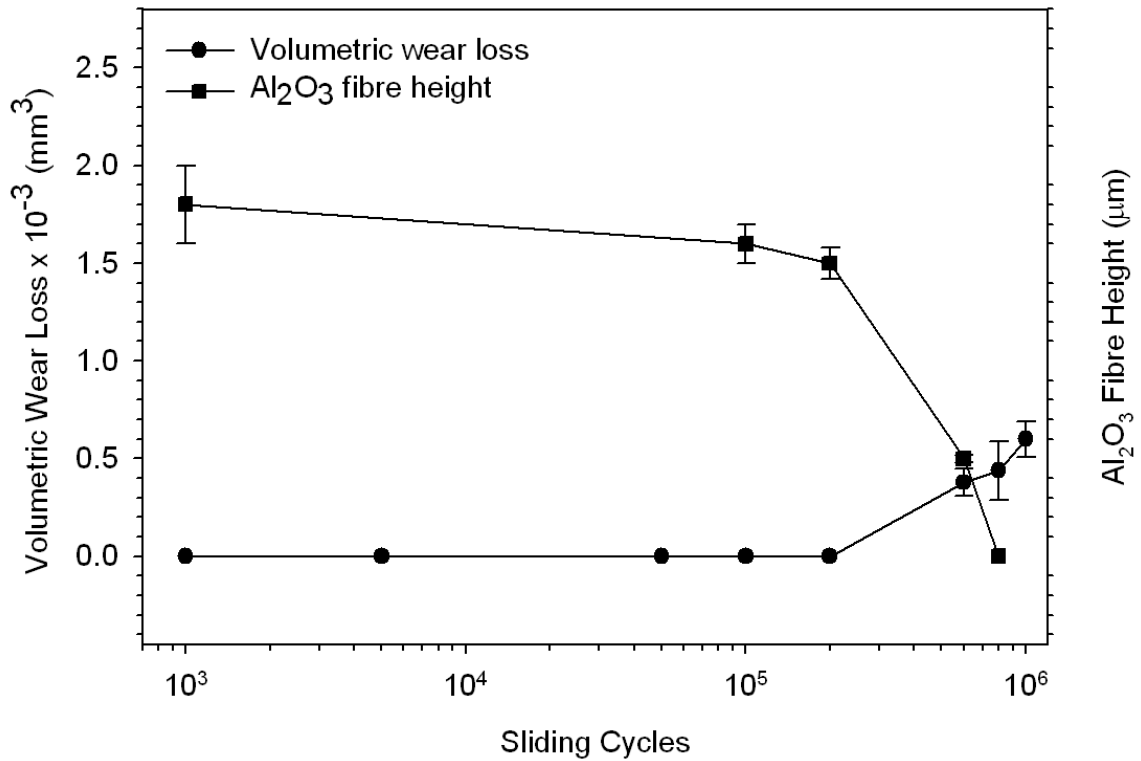
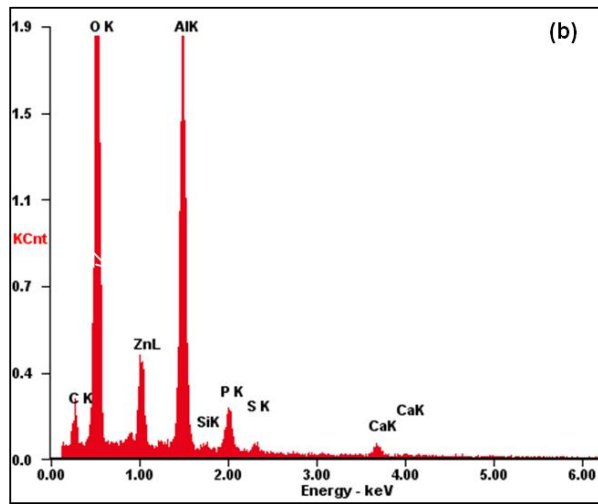
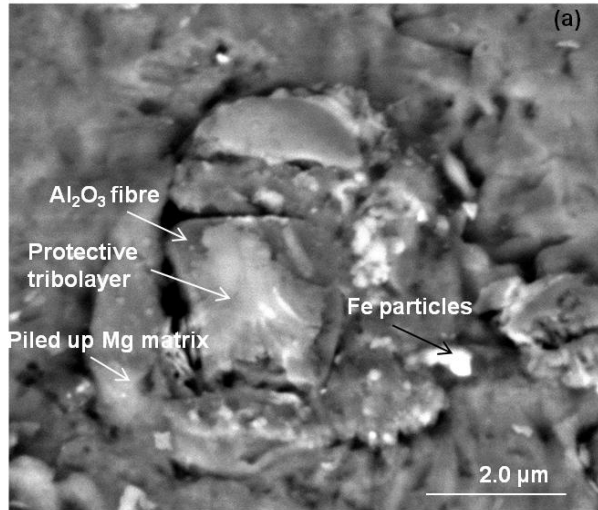


Fig.4.16. Plot of fibre height decrease and volumetric wear loss at 2.0 N load with increasing sliding cycles. After  $6 \times 10^5$  cycles, the  $\text{Al}_2\text{O}_3$  fibre height decreased to  $0.50 \pm 0.02 \mu\text{m}$  which corresponds to the increase in volumetric wear loss from 0.00-0.38 ( $\times 10^{-3}$ )  $\text{mm}^3$ . Thus damage to Mg matrix can be predicted by quantifying the fibre height decrease.



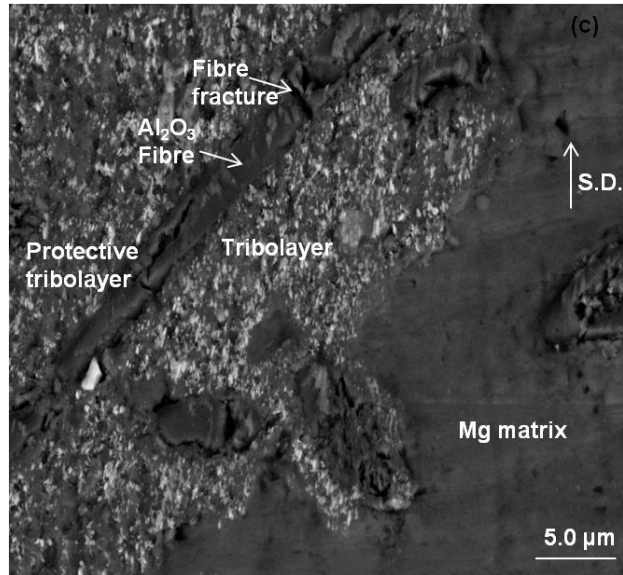


Fig.4.17. Back-scattered SEM micrographs of worn AM60-9%  $(\text{Al}_2\text{O}_3)_f$  at 100 °C. (a) Tribofilm formation on top of  $\text{Al}_2\text{O}_3$  fibre at 1.0 N load after  $1.0 \times 10^6$  cycles; (b) EDS analysis revealed that the tribofilm consisted of Zn, S, Ca and P; (c) Formation of tribofilm on top of  $\text{Al}_2\text{O}_3$  fibre and on the Mg matrix at 2.0 N load after  $1.0 \times 10^6$  cycles.

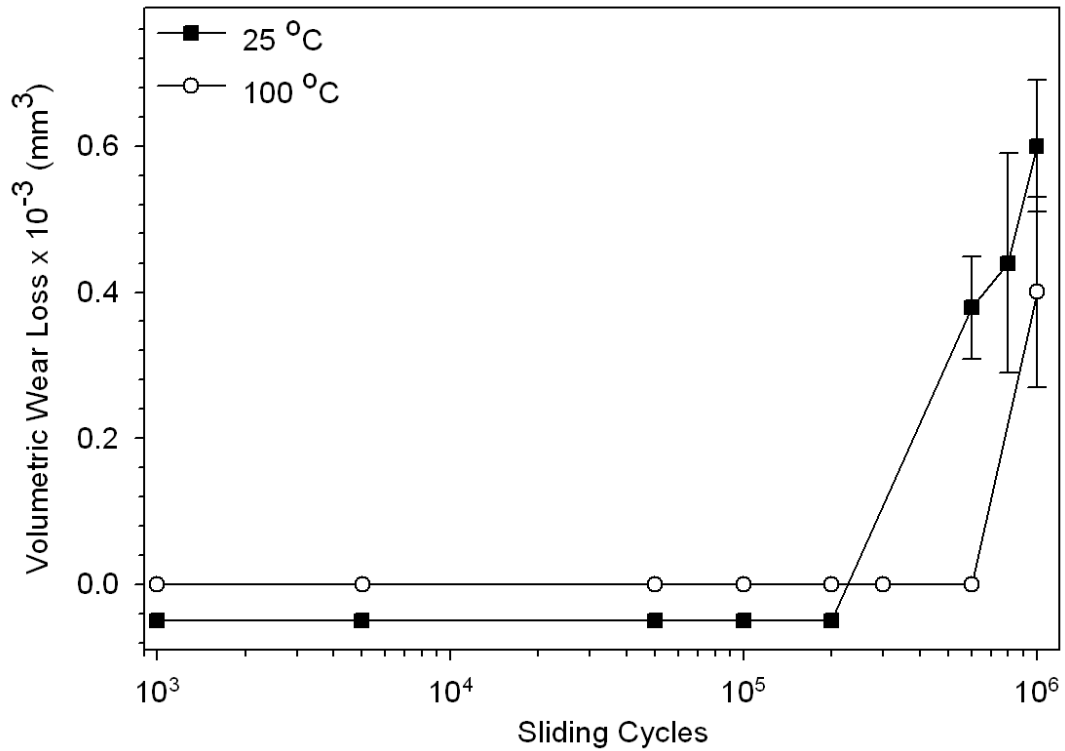


Fig.4.18. Comparison of volumetric wear loss vs. sliding cycles plot of AM60-9% (Al<sub>2</sub>O<sub>3</sub>)<sub>f</sub> at 100 °C and at 25 °C under 2.0 N load. The plot indicates that under the same conditions the wear rate was lower in case of tests conducted at 100 °C than at 25 °C. The transition to higher volumetric wear loss occurred after 6×10<sup>5</sup> cycles at 25 °C while at 100 °C the transition is postponed till after 8×10<sup>5</sup> cycles.

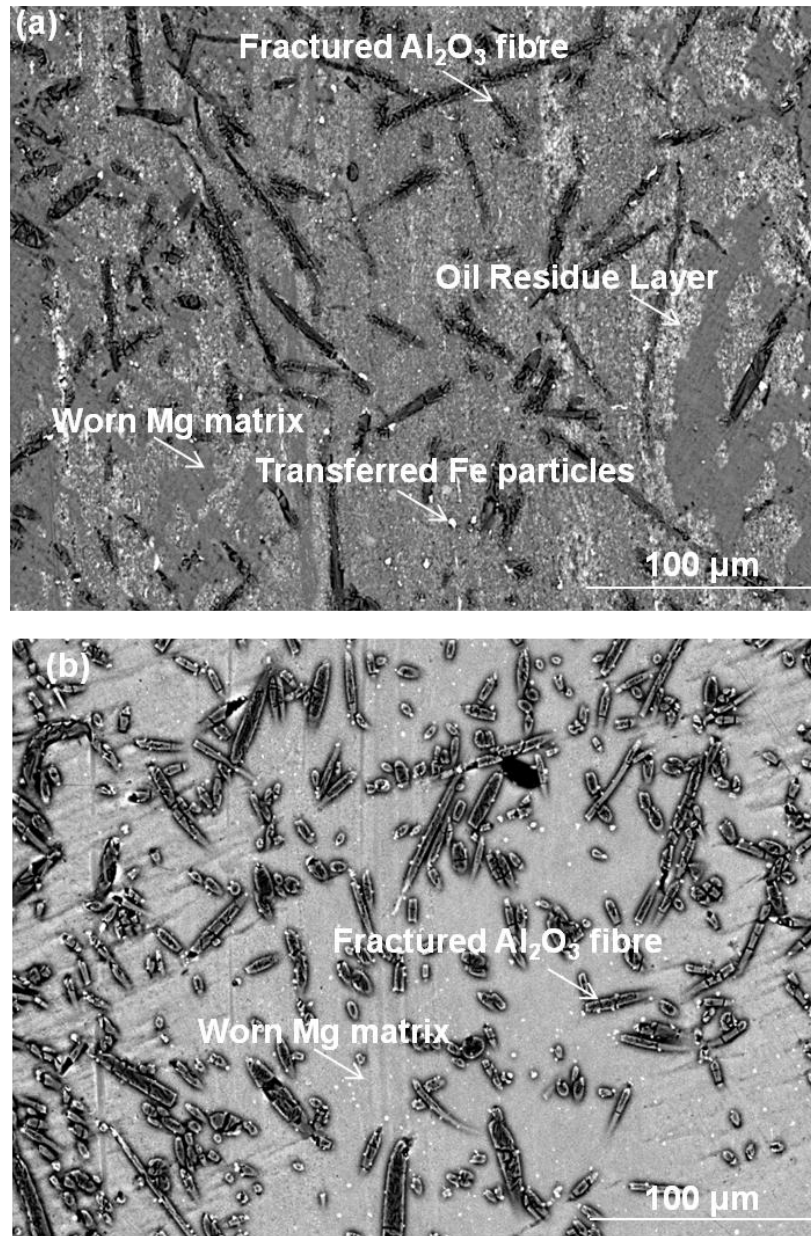


Fig.4.19. Back-scattered SEM micrographs of worn AM60-9%  $(\text{Al}_2\text{O}_3)_f$  and 2.0 N load at (a) 100 °C and (b) 25 °C. For tests conducted at 2.0 N load and 100 °C formation of the oil residue layer could be detected whereas at 25 °C the oil residue layer was not found.

#### 4.6. Damage to the counterface: AISI 52100 ball

The abrasion of hard  $\text{Al}_2\text{O}_3$  reinforcement phase against the relatively softer AISI 52100 steel balls led to severe damage to the counterface observed in the form of wear grooves (Fig.4.20). The material removal was quantified using a spherical cap volume loss model whereby the diameter of the wear track on the counterface material was used to calculate the amount of material removed.

At 25 °C sliding wear of AM60-9%  $(\text{Al}_2\text{O}_3)_f$  against AISI 52100 led to the transfer of Fe particles from the counterface onto the worn surface of the Mg composite. However, EDS analysis of the counterface indicated no material transfer between the composite and the counterface. Thus at 25 °C, the presence of  $\text{Al}_2\text{O}_3$  fibres in AM60-9%  $(\text{Al}_2\text{O}_3)_f$  composite proved to be detrimental for the wear of the counterface AISI 52100. Comparison of volumetric wear loss from the counterface surface against AM60-9%  $(\text{Al}_2\text{O}_3)_f$  and Al-18.5% Si is shown in Fig.4.21. It is evident from the plot that  $\text{Al}_2\text{O}_3$  fibres in AM60-9%  $(\text{Al}_2\text{O}_3)_f$  composite cause more damage to the counterface than caused by the Si particles in Al-18.5% Si alloy.

The volume loss from the counterface at 25 °C and after  $1 \times 10^6$  sliding cycles was calculated to be  $10.4 \times 10^{-4} \text{ mm}^3$  whereas at 100 °C the volume loss was  $7.1 \times 10^{-4} \text{ mm}^3$  indicating that the damage to the counterface was less for the sliding wear tests conducted at 100 °C. The reduced damage to the counterface might be attributed to the formation of the ORL on the worn surface of the counterface as indicated by EDS observations (Fig.4.22). Thus elevated temperature wear tests provided a way to reduce damage to the counterface as well. The average surface roughness of the counterface increased from the initial  $R_a=20.6 \text{ nm}$  to  $R_a=845.25 \text{ nm}$  at 100 °C after  $1 \times 10^6$  sliding cycles.

The effect of the increase of the  $\text{Al}_2\text{O}_3$  fibre volume fraction on the amount of material removal from the counterface was quantified. The calculation of the volume of material lost from AISI 52100 steel balls run against the Mg composites after  $1 \times 10^6$  sliding cycles indicated that an increase in the volume percentage of  $\text{Al}_2\text{O}_3$  fibres led to an increase in the counterface damage although the volumetric material loss from the composites decreased (Table 4-2). This observation indicates that the wear of both the mating surfaces should be considered during the design of sliding components made of these composites. Also, the damage induced on the counterface due to sliding against  $\text{Al}_2\text{O}_3$  fibres necessitates the study of alternate counterface material.

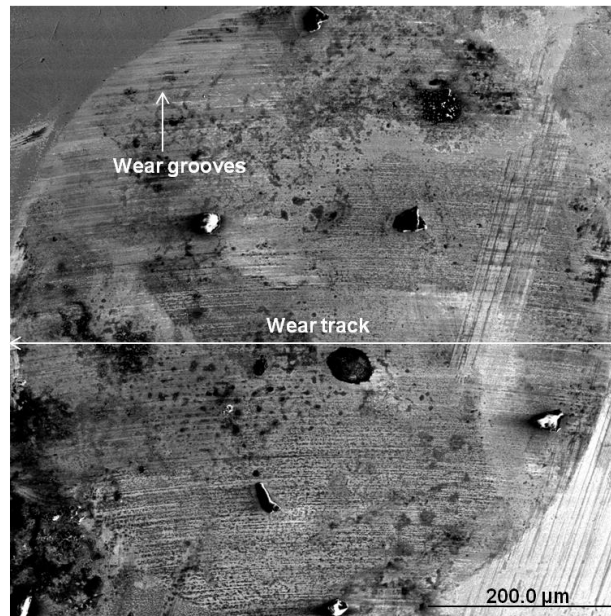


Fig.4.20. SEM image of the wear track on the counterface worn against AM60-9%  $(\text{Al}_2\text{O}_3)_f$  at 25 °C, after  $1 \times 10^6$  cycles, showing damage in the form of wear grooves.



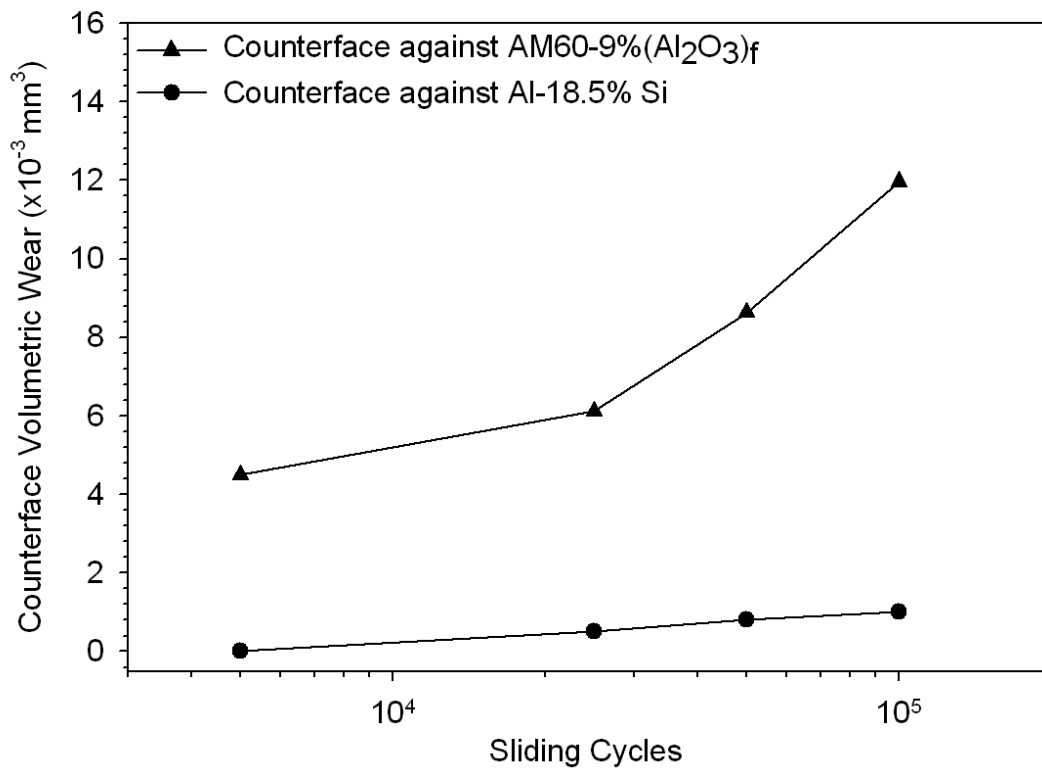


Fig.4.21. Plot of volumetric wear loss from the counterface against AM60-9% (Al<sub>2</sub>O<sub>3</sub>)<sub>f</sub> and Al-18.5% Si alloy at 5.0 N load. AM60-9% (Al<sub>2</sub>O<sub>3</sub>)<sub>f</sub> causes greater damage to the counterface than Al-18.5% Si alloy.

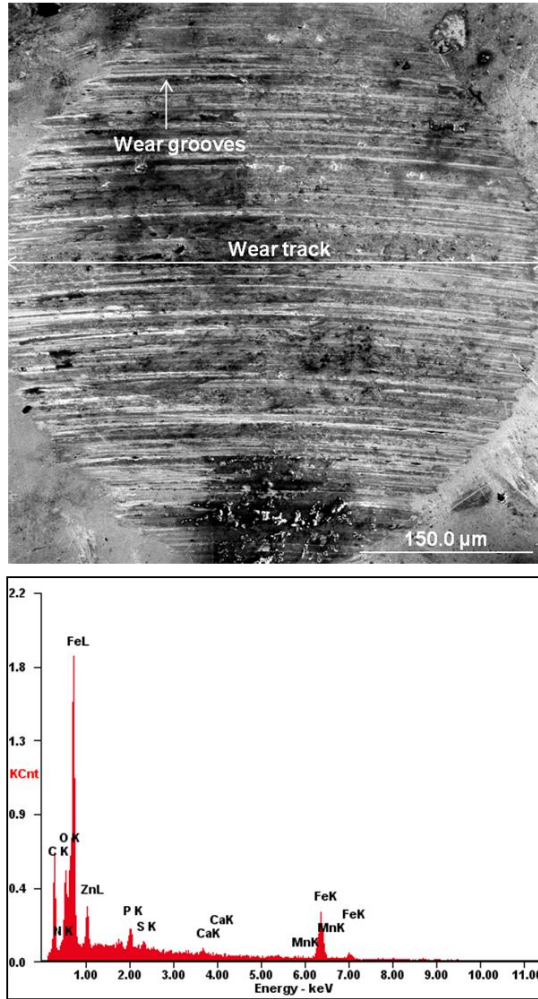


Fig.4.22. SEM micrograph and EDS result of the wear track on the counterface worn against AM60-9% (Al<sub>2</sub>O<sub>3</sub>)<sub>f</sub> at 100 °C and after 1×10<sup>6</sup> cycles. Presence of Zn, P, S and Ca on the worn counterface surface indicates formation of an oil residue layer on the counterface.

Table 4-2: Volume of material lost from AISI 52100 counterface and Mg matrix composites after  $1 \times 10^6$  sliding cycles.

	AM60-9% (Al <sub>2</sub> O <sub>3</sub> ) <sub>f</sub>	AM60-11% (Al <sub>2</sub> O <sub>3</sub> ) <sub>f</sub>	AM60-26% (Al <sub>2</sub> O <sub>3</sub> ) <sub>f</sub>
Volume of material lost from counterface (mm <sup>3</sup> )	$10.4 \times 10^{-4}$	$13.3 \times 10^{-4}$	$32.5 \times 10^{-4}$
Volume of material lost from composites (mm <sup>3</sup> )	$6.0 \times 10^{-4}$	$3.2 \times 10^{-4}$	$2.3 \times 10^{-4}$

## Chapter 5: Discussion

### 5.1. Introduction

The previous chapter described the damage features observed during sliding wear of the Mg composites AM60-9%  $(\text{Al}_2\text{O}_3)_f$ , AM60-11%  $(\text{Al}_2\text{O}_3)_f$  and AM60-26%  $(\text{Al}_2\text{O}_3)_f$ . The damage to the Mg matrix could be predicted by way of measuring the  $\text{Al}_2\text{O}_3$  fibre height decrease with increasing sliding cycles. Under all loading conditions fibre fracture and fragmentation was detected. Increasing the fibre volume percentage from 9% to 26% decreased the volumetric wear loss by 63%, but increased the damage to the counterface twice as much.

This chapter discusses the various factors which help to rationalize the damage features observed during the wear tests. A contact pressure analysis, adapted from the Greenwood-Tripp analysis [86], is implemented to estimate the amount of pressure exerted on the  $\text{Al}_2\text{O}_3$  fibres. This is followed by two sections discussing first strengthening of the Mg matrix due to mismatch of coefficient of thermal expansion between the Mg matrix and the  $\text{Al}_2\text{O}_3$  fibre followed by the effect of  $\text{Al}_2\text{O}_3$  fibre morphology on the fracture behaviour and corresponding wear mechanisms. A schematic representation of the sequence of damage events is presented. The chapter ends with a discussion of the role of the oil residue layer in delaying the wear of Mg composite at elevated temperature.

## 5.2. Contact Pressure Analysis

The original analysis of deformation and pressure at the contact between two elastic solids was performed by Hertz [83, 84]. In the Hertzian stress analysis, the following assumptions are considered: i) surfaces are continuous, smooth and non-conforming; ii) strains are small; iii) surfaces are frictionless.

The Hertzian pressure distribution is given by:

$$p(r) = p_0 \left\{ 1 - \left( \frac{r}{a} \right)^2 \right\}^{1/2} \quad (5.1)$$

where,  $p_0$  is the maximum contact pressure given by:

$$p_0 = \frac{3W}{2\pi a^2} = \left( \frac{6WE^*}{\pi^3 R^2} \right)^{1/3} \quad (5.2)$$

where,  $W$  is the normal load and  $E^*$  is the composite elastic modulus given by:

$$\frac{1}{E^*} = \frac{1 - \nu_1^2}{E_1} + \frac{1 - \nu_2^2}{E_2} \quad (5.3)$$

where,  $\nu$  and  $E$  are the Poisson's ratio and Young's modulus respectively; subscript 1 and 2 refers to the two bodies. In this case  $\nu_1$  and  $E_1$  refers to the Poisson's ratio and Young's modulus for AM60-9%  $(Al_2O_3)_f$  while  $\nu_2$  and  $E_2$  refers to the Poisson's ratio and Young's modulus for steel counterface. Using these values (Table 5-1), the  $E^*$  was calculated to be 51.7 GPa.

The contact radius  $a$  is given by:

$$a = \left( \frac{3WR}{4E^*} \right)^{1/3}$$

(5.4)

where, R is the effective composite curvature and is given by:

$$\frac{1}{R} = \frac{1}{R_1} + \frac{1}{R_2} \quad (5.5)$$

In this case,  $R_1=3$  mm (radius of the counterface) while  $R_2$  is assumed to be flat. Using the values listed in Table 5-2 the maximum contact pressure  $p_0$  was calculated to be 620.9 MPa and correspondingly the Hertzian pressure distribution  $p(r)$  was determined (Fig.5.2a). From Fig.5.2a it is evident that the calculated maximum apparent contact pressure applied on the  $Al_2O_3$  fibres was lower than the matrix hardness (converted from HV to MPa according to the relation mentioned in section 3.2). Thus it was necessary to calculate the real contact pressure on a surface with asperities.

Table 5-1. Parameters used to calculate the composite elastic modulus  $E^*$ .

Elastic modulus of AM60-9% ( $Al_2O_3$ ) <sub>f</sub> ( $E_1$ , GPa)	Elastic modulus of AISI 52100 ( $E_2$ ,GPa) [85]	Poisson's ratio of AM60, $\nu_1$ [85]	Poisson's ratio of AISI 52100 $\nu_2$ [85]
52.20	210.00	0.35	0.3

Table 5-2. Parameters used to calculate the Hertzian pressure distribution.

Composite elastic modulus of AM60-9% $(Al_2O_3)_f$ and 52100 steel; ( $E^*$ ,GPa)	Normal load; (W,N)	Effective composite curvature; (R, m)	Contact radius (a, $\mu m$ )
47.2	5.0	0.003	60.1

The Hertzian analysis assumes the contact surfaces to be smooth and thus excludes applicability to all real solids. Real solid surfaces are rough, comprising of asperities or high spots where contact is made at isolated points only. An estimation of the contact stresses exerted on rough surfaces is achievable using Greenwood-Tripp (G-T) contact model [86]. The G-T model is an extension of the Hertzian model for the case where one of the mating surfaces was assumed to consist of spherical asperities (peaks) following a Gaussian height distribution. In this work, the G-T model was employed to calculate the contact pressure distribution on the  $Al_2O_3$  fibres of length  $R_f$ , considered as asperities against the steel counterface, protruding above the Mg matrix by  $1.8 \pm 0.2 \mu m$ . These  $Al_2O_3$  fibres, considered as asperities, were fitted to two Gaussian profiles (Fig.5.1) where the first peak, representing the Mg matrix, was adjusted to the zero position on the x-axis, while the second peak represented the  $Al_2O_3$  fibre elevation. From the nature of

the Gaussian curve fittings the contact stress on  $\text{Al}_2\text{O}_3$  fibres were calculated using the G-T model.

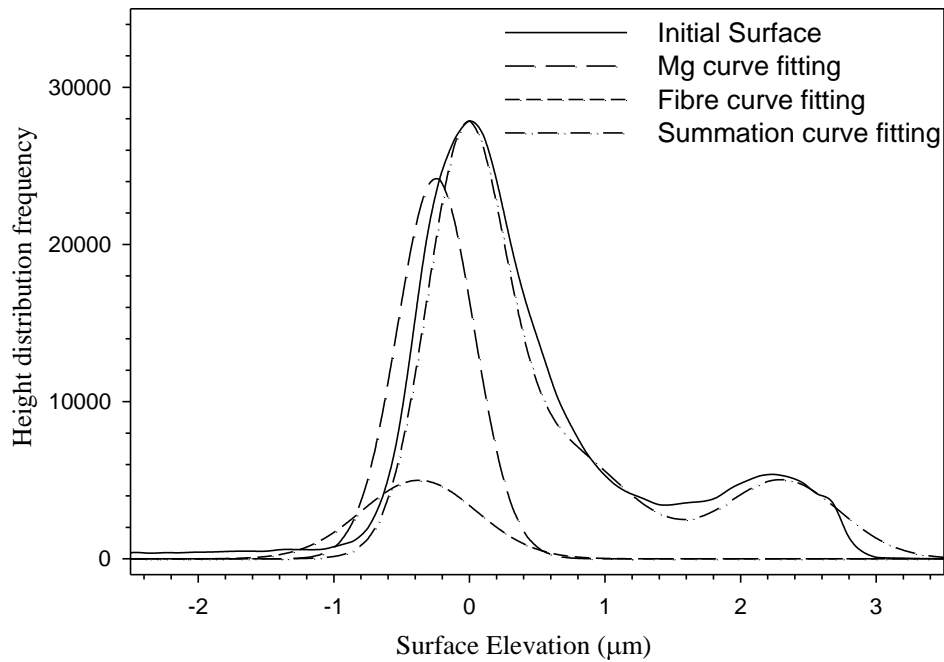


Fig.5.1. Histogram of the initial surface of AM60-9%  $(\text{Al}_2\text{O}_3)_f$  under unetched conditions with 3 other curves fitted to the Mg peak,  $\text{Al}_2\text{O}_3$  fibre peak and summation of all the curve fittings respectively.

According to the G-T model, if the separation between the nominal surfaces at the position of a particular  $\text{Al}_2\text{O}_3$  fibre is considered to be 'u' then contact ensued under the condition of asperity height  $z > u$ . Thus probability of contact is thus:

$$\text{prob}(z > u) = \int_u^{\infty} \phi(z) dz \quad (5.6)$$



where  $\phi(z)$  is the probability density function of the  $\text{Al}_2\text{O}_3$  fibre height distribution. Considering  $\eta$  as the density of  $\text{Al}_2\text{O}_3$  fibres (asperities) and a surface element  $d\psi$ , the expected number of contacts  $dN$  and real area of contact  $dA_r$  are given by equations (5.7) and (5.8) respectively.

$$dN = \eta d\psi \int_u^{\infty} \phi(z) dz \quad (5.7)$$

$$dA_r = \pi \eta R_f d\psi \int_u^{\infty} (z-u) \phi(z) dz \quad (5.8)$$

where  $R_f$  is the  $\text{Al}_2\text{O}_3$  fibre length. The magnitude of contact pressure,  $P_r$ , on the asperities is determined by the following equation:

$$P_r = \frac{4}{3} E^* R_f^{1/2} (z-u)^{3/2} \phi(z) dz$$

(5.9)

The applied load  $dP$  is given by:

$$dP = \frac{4}{3} \eta E^* R_f^{1/2} d\psi \int_u^{\infty} (z-u)^{3/2} \phi(z) dz \quad (5.10)$$

It is convenient to introduce standardized variables and describe the asperity heights in terms of  $\sigma$ , the standard deviation of asperity height distribution. The standard deviation of asperity height  $\sigma$  was determined from the curve fitting of the peak for  $\text{Al}_2\text{O}_3$  fibres as shown in Fig.5.1. The two peaks of the histogram in Fig.5.1 represent the peak for Mg matrix (peak with higher frequency) and  $\text{Al}_2\text{O}_3$  fibre. These were assumed to follow a Gaussian distribution, represented by Eqn.5.11.

$$f(x) = A \exp \left( \frac{-(x - b_1)^2}{c_1^2} \right) \quad (5.11)$$

where, A is the height of the peak of the curves,  $b_1$  is the position of the centre of the peak and  $c_1$  represents width of the bell. Eqn. 5.11 was used to calculate the curve fittings for the individual peaks for the Mg matrix and  $Al_2O_3$  fibre and finally the summation curve for both the peaks. Eqn. 5.11 was compared to the general relation for Gaussian distribution given by:

$$f(x) = \frac{1}{\sqrt{2\pi}\sigma} \exp(-(x-a)^2/2\sigma^2) \quad (5.12)$$

Therefore, the value was  $\sigma$  was determined from the curve fitting for  $Al_2O_3$  fibre as follows:

$$\sigma = \frac{c_1}{\sqrt{2}} \quad (5.13)$$

Thus equations (5.7), (5.8) and (5.10) can be rewritten in the following ways:

$$dN = \eta d\psi F_0(h) \quad (5.14)$$

$$dA_r = \pi \eta R_f \sigma d\psi F_1(h) \quad (5.15)$$

$$dP = \frac{4}{3} E * \eta (R_f \sigma)^{1/2} \sigma d\psi F_{3/2}(h) \quad (5.16)$$

where,  $h=u/\sigma$  ; for Gaussian distribution of fibre heights:

$$F_n(h) = \left[ \frac{1}{(2\pi)^{1/2}} \right] \int_u^\infty (s-h)^n \exp(-\frac{1}{2}s^2) ds \quad (5.17)$$

where  $s$  is the dimensionless asperity height that corresponds to  $Al_2O_3$  fiber height of the polished surface in the Mg composite.

The term  $\eta(R_f\sigma)$  was assumed to represent the area density of the  $Al_2O_3$  fibres measured using quantitative metallography (using ImageJ software), while standard

deviation of fibre heights ( $\sigma$ ) was obtained by Gaussian curve fitting the fibre height distribution frequency in the histogram of represented in Fig.5.1. Considering the applied load  $dP$  on the surface area  $d\psi$  equivalent to a uniform pressure  $p(r)$  as follows

$$p(r) = \frac{dP}{d\psi} = E * \eta(R_f \sigma)^{1/2} \sigma F_{3/2}(h) \quad (5.18)$$

The maximum real contact pressure occurs at the center of the contact area, at  $r=0$ :

$$p_{r=0} = \frac{dP}{dA_r} = \left(\frac{4}{3\pi}\right) E * \left(\frac{\sigma}{R_f}\right)^{1/2} \frac{F_{3/2}(h)}{F_1(h)} \quad (5.19)$$

Using the parameters enlisted in Table 5-3 the contact pressure distribution and the maximum contact pressure on the  $Al_2O_3$  fibres was calculated by solving Eqn.5.18 and 5.19 respectively and plotted against radial distance (Fig.5.2a). The calculated contact pressure at the centre of the wear track was as high as 2.825 GPa at 1.0 N which increased to 3.124 GPa at 5.0 N. The calculated Hertzian pressure under 5.0 N load was found to be approximately 81% less than the real contact pressure.

It is established [87, 88] that indentation on a rigid plastic material induces plain strain plastic deformation. Tabor [88] derived from a plot of mean indentation pressure vs.  $d/D$ , where  $d$  is the diameter of the spherical indentation and  $D$  is the diameter of the indenter ball, the value of constraint factor  $C=2.89$  in the equation  $P=CY$ , which was the ratio between the mean contact pressure  $P$  and the uniaxial yield stress ( $Y$ ). The sinking-in of the  $Al_2O_3$  fibres may be compared to the plain strain deformation of the Mg matrix. Thus the yield pressure required for indentation of the Mg matrix with  $Al_2O_3$  fibres may be considered to be approximately equal to the Mg matrix hardness  $90.8 \pm 4.7$  HV or 892 MPa. The calculated contact stress (3.12 GPa at 5.0 N load) peaked at the centre of

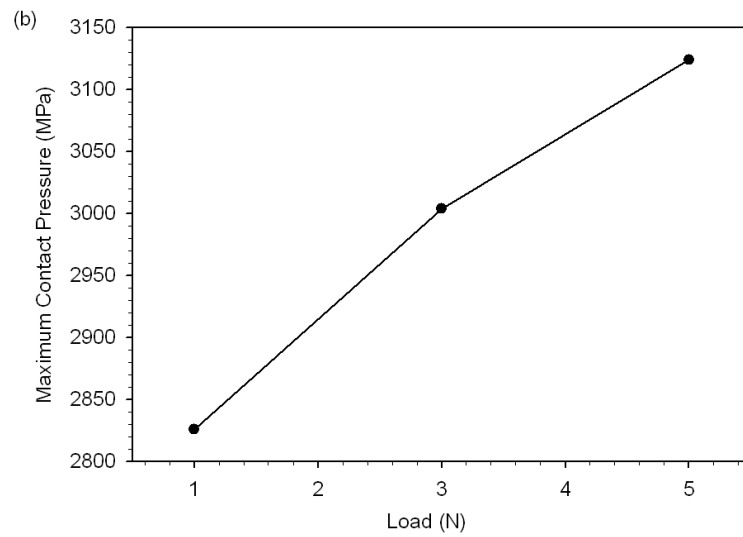
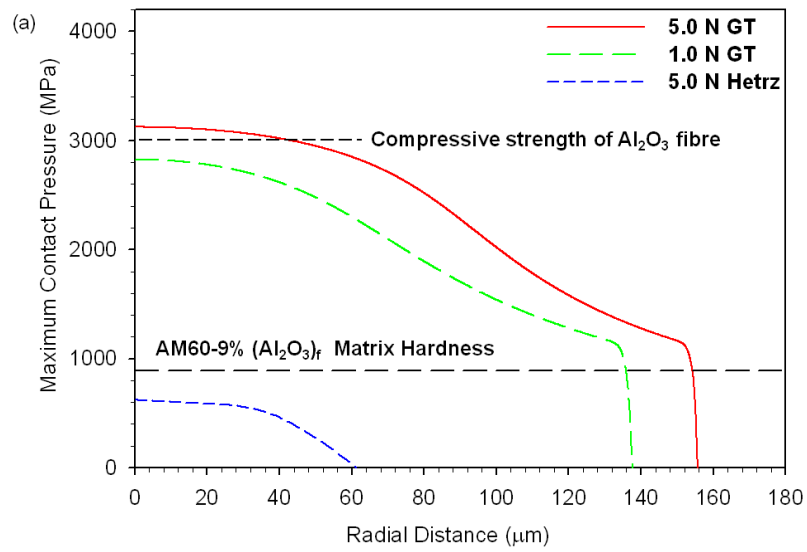
the wear track and exceeded the Mg matrix hardness. The contact pressure at both 1.0 N and 5.0 N load were comparable to the compressive strength of Al<sub>2</sub>O<sub>3</sub> fibre (=3GPa [89]). The important implications of the estimated contact pressure represented in Fig.5.2a are i) Al<sub>2</sub>O<sub>3</sub> fibre fracture and ii) surface plastic deformation of the Mg matrix under all loading conditions-both of which were experimentally verified. The G-T contact pressure was maximum at radial distance  $r=0$  indicating occurrence of maximum damage at the centre of the wear track which was in good agreement with the experimental findings (Fig.5.2c). The radial distance at which the real contact stresses became zero was approximately equal to the width of the wear track ( $260\pm 15.5 \mu\text{m}$ ) confirming the agreement of theoretically calculated values of real contact stress with the experimental findings.

It is to be noted that the modified G-T model adapted to calculate the contact pressure on Al<sub>2</sub>O<sub>3</sub> fibres has several shortcomings worth considering. The original Greenwood-Tripp model was proposed for asperities of monolithic materials whereas here a composite surface with Al<sub>2</sub>O<sub>3</sub> fibres has been considered. The G-T model assumed spherical particles which were distributed according to the Gaussian relation-however, in the present composite the needle shaped cylindrical fibres and the Mg matrix showed a bimodal height distribution. Also the contact stress calculated using the G-T model only estimates the applied stress on the Al<sub>2</sub>O<sub>3</sub> fibres at the very beginning of the sliding process. The change in fibre length  $R_f$ , due to fibre fragmentation, would increase the G-T stress. Further, the damage to the counterface caused by the Al<sub>2</sub>O<sub>3</sub> fibres results in an increase in the average surface roughness of counterface AISI 52100 from the initial  $R_a=20.6 \text{ nm}$  to  $R_a=616.52 \text{ nm}$  at 25 °C after  $1\times 10^6$  sliding cycles. Thus with increasing sliding cycles the G-T contact pressure would change. Despite these discrepancies, the

adapted static contact stress model explains the fibre fracture and Mg deformation even at low applied load of 1.0 N.

Table 5-3. Parameters used to calculate the Greenwood-Tripp contact pressure on  $\text{Al}_2\text{O}_3$  fibres.

Composite elastic modulus of AM60-9% $(\text{Al}_2\text{O}_3)_f$ and 52100 steel; ( $E^*$ ,GPa)	$\text{Al}_2\text{O}_3$ fibre length; ( $R_f$ , $\mu\text{m}$ )	Standard deviation of $\text{Al}_2\text{O}_3$ fibre height; ( $\sigma$ , $\mu\text{m}$ )	Area fraction of fibres;
47.2	15.78	0.28	0.09



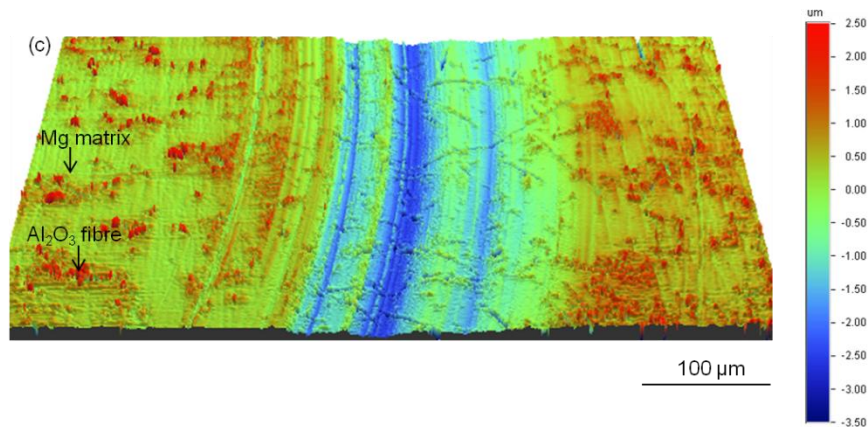


Fig.5.2. (a) The calculated G-T contact pressure distribution on the  $\text{Al}_2\text{O}_3$  fibres for AM60-9%  $(\text{Al}_2\text{O}_3)_f$  at 5.0 N and 1.0 N load. The Hertzian pressure distribution is also shown. (b) Plot of G-T stress with increasing load and (c) Optical profilometry image, at 5.0 N load and after  $1 \times 10^6$  cycles, indicating maximum damage at the centre of the wear track and the width of wear track ( $260 \pm 15.5 \mu\text{m}$ ) approximately equal to the width of wear track predicted by plot (a).

### 5.3. Effect of matrix hardness

The normal force applied during the sliding wear process was estimated using G-T and Hertz contact stress calculations outlined in the previous section. It will now be useful to discuss the force counterbalancing this normal force. As discussed in section 2.2.2.1, the phenomenon of strengthening in metal matrix composites reinforced with fibres can mainly be attributed to the load transfer from matrix to reinforcement and an increase in dislocation density due to thermal mismatch between the matrix and the reinforcement [39].

The increase in dislocation density due to the mismatch in coefficient of thermal expansion between  $\text{Al}_2\text{O}_3$  fibres may be calculated using the equation 5.20.

$$\rho_T = \frac{12V_p \Delta\alpha_T \Delta T}{(1 - V_p) b D} \quad (5.20)$$

where,  $V_p$  is the volume fraction of  $Al_2O_3$  fibre,  $\Delta\alpha$  is the difference in the coefficient of thermal expansion of the fibre and the Mg matrix,  $\Delta T$  is the temperature difference between the molten Mg and the perform ( $750-650=100\text{ K}^{-1}$ ),  $b$  is the dislocation density for Mg and  $D$  is the fibre width. Using the parameters enlisted in Table 5-4, the increase in dislocation density for three composites AM60-9%  $(Al_2O_3)_f$ , AM60-11%  $(Al_2O_3)_f$  and AM60-26%  $(Al_2O_3)_f$  were calculated to be  $1.6 \times 10^{13}$ ,  $2.0 \times 10^{13}$  and  $5.6 \times 10^{13}$ . Using a composite sphere model Ramakrishnan [90] combined the two factors of load transfer and the generation of new dislocations into Eqn. 5.13 to calculate the enhanced (compressive) strength ( $\sigma_e$ ) of the composite.

$$\sigma_e = \sigma_y (1 + f_d)(1 + f_1) \quad (5.21)$$

where,  $\sigma_y$  is the yield strength of the matrix alloy,  $f_1$  ( $=0.50$  [38]) is the improvement factor due to the load bearing effect of the matrix and  $f_d$  associated with dislocation strengthening can be represented as following:

$$f_d = \frac{k G_m b \sqrt{\rho}}{\sigma_y} \quad (5.22)$$

where  $k$  is a constant whose value is taken as 1.25 [90],  $G_m$  ( $=17.0\text{ GPa}$  [91]) is the shear modulus of the matrix,  $\rho$  is the dislocation density.

Eqn.5.21 was used to calculate the increase in yield strength due to addition of fibres in Mg composites and was further compared (Table 5-4) with the matrix hardness (three times the yield strength [88]). When  $V_p=0$  (for the AM60 alloy), the value of  $\rho_T$ ,  $f_d$



and  $f_1$  is 0 indicating  $\sigma_e = \sigma_y$  (according to Eqn.5.21), i.e. the yield strength of AM60 alloy. It is evident from Table 5-5 that for AM60-9%  $(Al_2O_3)_f$  and AM60-11%  $(Al_2O_3)_f$  the theoretically calculated values correlated well with the experimentally measured matrix indentation hardness. The mismatch in the theoretical and the experimental values in case of AM60-26%  $(Al_2O_3)_f$  can be attributed to the higher probability of the indenter hitting a subsurface  $Al_2O_3$  fibre during the micro-indentation experiments.

Table 5-4. Parameters used to calculate the increase in dislocation density in Mg composites AM60-9%  $(Al_2O_3)_f$ , AM60-11%  $(Al_2O_3)_f$  and AM60-26%  $(Al_2O_3)_f$ .

$V_p$	$\Delta\alpha$ ( $K^{-1}$ )[91]	$\Delta T$ (K)	$b$ (m) [92]	$D$ (m)	$\rho_T$
0.09	$3.9 \times 10^{-5}$	100	$0.28 \times 10^{-10}$	$3.72 \times 10^{-6}$	$3.54 \times 10^{12}$
0.11	$3.9 \times 10^{-5}$	100	$0.28 \times 10^{-10}$	$3.72 \times 10^{-6}$	$4.42 \times 10^{12}$
0.26	$3.9 \times 10^{-5}$	100	$0.28 \times 10^{-10}$	$3.72 \times 10^{-6}$	$1.25 \times 10^{13}$

Table 5-5. Comparison of calculated values of hardness with experimentally measured microindentation hardness results.

	$H=3\times\sigma_e$ (MPa)	Measured indentation hardness (MPa)
AM60	393	503±63
AM60-9% (Al <sub>2</sub> O <sub>3</sub> ) <sub>f</sub>	874	890±47
AM60-11% (Al <sub>2</sub> O <sub>3</sub> ) <sub>f</sub>	900	1006±28
AM60-26% (Al <sub>2</sub> O <sub>3</sub> ) <sub>f</sub>	951	1390±53

#### 5.4. Effect of Al<sub>2</sub>O<sub>3</sub> fibre morphology

Sliding wear comprises predominantly of two forces-a predominant normal force and lesser effective shear force. This section examines the effect of both normal and shear forces on Al<sub>2</sub>O<sub>3</sub> fibres and a critical length and aspect ratio has been determined for both the cases below in which fracture of fibres can be prevented.

##### 5.4.1 Critical fibre length under normal force

It is useful to consider the fibre orientations in the Mg composite with respect to the normal loading condition. Assuming the fibres to be cylindrical in shape, we consider two representative fibre orientations: fibre length parallel to the direction of loading

(Fig.5.3a) and fibre length normal to the direction of loading (Fig.5.3b). It should be noted that the developed model pertains to the orientation represented in Fig.5.3a and therefore has limited implications. Further development in the model in the future will subsequently include the other orientation thus completing the fibre fracture analysis.

The normal load applied on the fibres, acting as load bearing elements, is supported by the matrix beneath it (Fig.5.3a) with the load transfer agent being the matrix-fibre bond. Under the condition that the matrix supports the fibre without yielding and without fibre fracture the following forces can be considered to be in equilibrium:

$$\sigma_f \frac{\pi w^2}{4} = H_m \pi w \frac{L}{k} \quad (5.23)$$

The left hand side of the equation represents the normal force exerted on the fibre cross-section while the right hand side indicates the total force applied on the surface of the cylinder. Thus the critical fibre length  $L_c$ , below which fibre fracture will not occur may be determined by

$$L_c = \frac{L}{k} = \frac{\sigma_f w}{4H_m} \quad (5.24)$$

where,  $\sigma_f$  is the compressive strength of  $Al_2O_3$  fibres ( $\approx 3000$  MPa [89]),  $w$  is the width of the fibres,  $H_m$  is the matrix hardness of the composites AM60-9%  $(Al_2O_3)_f$ , AM60-11%  $(Al_2O_3)_f$  and AM60-26%  $(Al_2O_3)_f$  including the matrix strengthening effect caused by the increase in dislocation density and  $k$  is the number of fragments. Table 5-6 shows the critical fibre length for AM60-9%  $(Al_2O_3)_f$ , AM60-11%  $(Al_2O_3)_f$  and AM60-26%  $(Al_2O_3)_f$ . From Table 5-6 it can thus be concluded that under the load range the fibre, of an average initial length of  $13.92 \pm 9.91 \mu m$  will form fragments of size  $\geq 2.93 \mu m$ . The

propensity for fracture and fragmentation is found to increase (Table 5-6) with increase in matrix hardness caused by the addition of Al<sub>2</sub>O<sub>3</sub> fibre.

Rearranging Eqn.5.24 and making k, number of fragments, the subject of the equation, Eqn.5.25 is obtained. Eqn.5.25 can thus be used to predict the number of fragments that might be expected due to fracture of a fibre of initial length L. Fig.5.4 indicates the correlation between the experimentally measured number of fragments obtained from a particular initial fibre length with the number of fragments predicted from Eqn.5.25 from the same initial fibre length. It is evident that the predicted values from Eqn.5.25 are in good agreement with the experimental findings. The value of k=1 was set as a lower bound to the fibre fragmentation process. Any fibre of initial length L that produces a value of k<1(from Eqn.5.25) will not undergo fibre fracture (Fig.5.4).

$$k = \frac{4H_m L}{\sigma_f w} \quad (5.25)$$

It is useful to discuss the implications of Eqn.5.25. As the Al<sub>2</sub>O<sub>3</sub> fibre volume fraction is increased from 9% to 26% the matrix hardness (H<sub>m</sub>) increases due to increase in dislocation density as discussed in section 5.3. Thus from Eqn.5.25 it can be seen that increasing the fibre volume content leads to greater degree of fragmentation. Based on Eqn.5.25 it can be predicted that larger the fibre length greater would be the fracture and fragmentation process indicating that future designing of fibre reinforced composites should consider use of short fibres.

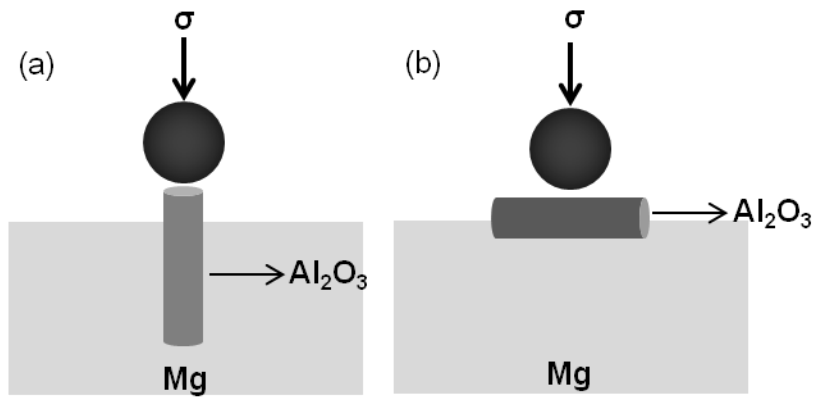


Fig.5.3. Representative fibre orientations (a) parallel and (b) perpendicular to the direction of applied normal load in the Mg composites. The model developed in section 5.4.1 considers only (a) where the fibre is parallel to the direction of loading.

Table 5-6. Calculation of average critical length of fragmented fibre.

Composite	Compressive strength of Al <sub>2</sub> O <sub>3</sub> fibres , $\sigma_f$ , MPa	Matrix hardness, H <sub>m</sub> , MPa	Average fibre width,w, $\mu\text{m}$	Critical Length (L <sub>c</sub> ), $\mu\text{m}$
AM60-9% (Al <sub>2</sub> O <sub>3</sub> ) <sub>f</sub>	3000	894.31	3.72±0.75	2.93
AM60-11% (Al <sub>2</sub> O <sub>3</sub> ) <sub>f</sub>	3000	900.40	3.72±0.75	2.61
AM60-26% (Al <sub>2</sub> O <sub>3</sub> ) <sub>f</sub>	3000	951.78	3.72±0.75	1.88

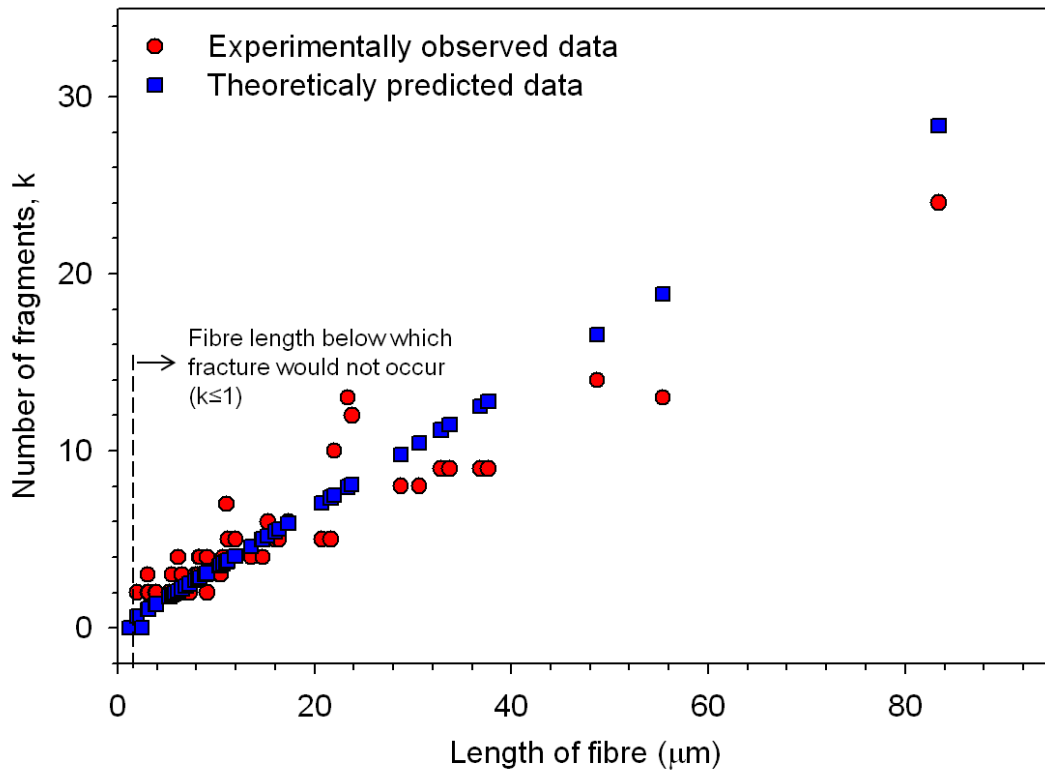


Fig.5.4. Correlation plot between number of fragments observed for an initial length  $L$  obtained from experimental observations and the values predicted from Eqn.5.25.

#### 5.4.2. Critical fibre aspect ratio during shear force

Single pass sliding contact tests conducted on AM60-9% (Al<sub>2</sub>O<sub>3</sub>)<sub>f</sub> helped elucidate the wear mechanisms and the effect of applied load on the Al<sub>2</sub>O<sub>3</sub> fibres during surface traction. Sliding contact tests conducted at 0.05 N indicated that the Al<sub>2</sub>O<sub>3</sub> fibres remained mostly intact without fracturing (Fig.5.5a). When the applied load was increased to 0.07 N load, the fibres underwent fracture and fragmentation with cracks initiating and propagating perpendicular to the sliding direction (Fig.5.5b). The fragmented fibres however did not sink into the Mg matrix. This indicates that an applied load as low as 0.07 N is sufficient to fracture the Al<sub>2</sub>O<sub>3</sub> fibres.

Fracture of fibres is largely dependent upon the fibre aspect ratio. Alpas [93] formulated Eqn.5.26 to predict the critical aspect ratio below which particles/fibres will fracture.

$$(t/l)_c = [\kappa \sqrt{P} h_f (\mu \frac{\sqrt{H_m}}{K_{IC}})]^{1/2}$$

(5.26)

where, t and l were the length and breadth of Al<sub>2</sub>O<sub>3</sub> fibres, applied load P=0.05-2.0 N, fibre elevation height  $h_f = 1.8 \times 10^{-6}$  m obtained by profilometric surface analyses, Mg matrix hardness of the composite AM60-9% (Al<sub>2</sub>O<sub>3</sub>)<sub>f</sub>  $H_m = 8.9 \times 10^2$  MPa, coefficient of friction  $\mu=0.35$  obtained from single pass sliding scratch tests, fracture toughness of Al<sub>2</sub>O<sub>3</sub> fibres  $K_{IC}=4.0$  MPa (m<sup>1/2</sup>) [85] and a constant  $\kappa=10^5$  m<sup>-3/4</sup> introduced to obtain a dimensionless quantity. Critical fibre aspect ratios calculated for the load range 0.05 N-5.0 N (Table 5-7), below which fibres are expected to fracture. The measured fibre aspect ratio in Mg composites was 3.42±5.85. As evident from Table 5-7, fibre should remain



unaffected at 0.05 N load while at 0.07 N load they should fracture as  $(t/l) < (t/l)_c$ , which correlates well with the experimental findings (Fig.5.5). Thus it is evident that the  $\text{Al}_2\text{O}_3$  fibres will fracture at all contact conditions during sliding wear (1.0-5.0 N load range).

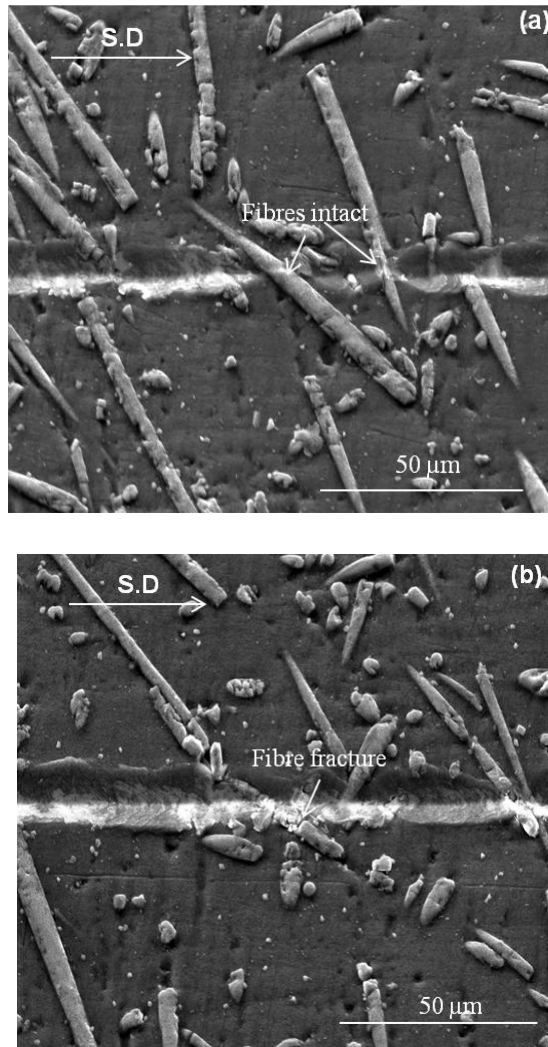


Fig.5.5. SEM micrographs indicating difference in damage features after single pass sliding contact tests performed at constant loads of (a) 0.05 N and (b) 0.07 N.

Table 5-7. Calculation of critical fibre aspect ratio. Fibres are expected to fracture when  $(t/l) < (t/l)_c$ .

Load (N)	$(t/l)_c$	$(t/l)$
0.05	3.24	3.55
0.07	3.59	
1.0	7.32	
2.0	8.71	
5.0	10.95	

## 5.5. Damage events

The matrix strengthening due to increase in fibre volume percentage eventually concedes the advantage gained by adding higher amount of reinforcement. The high matrix hardness does not allow the fibres to undergo sink-in process during sliding wear. As a result crack formation and propagation occurs in the  $\text{Al}_2\text{O}_3$  fibres, to accommodate the normal and the shear force applied during the pin-on-disk sliding wear process, eventually leading to fracture and fragmentation. This is quantitatively explained using Eqn.5.24/5.25-assuming constant normal load, with an increase in matrix hardness due to an increase in fibre volume fraction the critical size decreases leading to higher propensity for fragmentation. An increase in the fibre width would decrease the fibre fragmentation process-thus an  $\text{Al}_2\text{O}_3$  particle (average length of  $2.5\pm 2.2 \mu\text{m}$ ) should not undergo fragmentation. Fig.4.6b corroborates this fact where only fibre fracture and fragmentation is observed whereas particles are unaffected at 5.0 N load and after  $1\times 10^5$  cycles. The fibre fragmentation process is followed by a decrease in the fibre height due to the sinking in of the comminuted fibres.

The effect of matrix hardness on wear of the three composites AM60-9%  $(\text{Al}_2\text{O}_3)_f$ , AM60-11%  $(\text{Al}_2\text{O}_3)_f$  and AM60-26%  $(\text{Al}_2\text{O}_3)_f$  is represented in Fig.5.6. Note that although the matrix hardness of AM60-26%  $(\text{Al}_2\text{O}_3)_f$  is considerably higher than AM60-9%  $(\text{Al}_2\text{O}_3)_f$  and AM60-11%  $(\text{Al}_2\text{O}_3)_f$ , the volumetric wear loss is not mitigated to the same extent. This might be explained by Fig.5.7 which indicates that the maximum change in aspect ratio is observed in the case of AM60-26%  $(\text{Al}_2\text{O}_3)_f$  after  $6\times 10^5$  sliding cycles. This might be attributed to the high matrix hardness resulting in a higher

probability of fracture and fragmentation of the  $\text{Al}_2\text{O}_3$  fibres in the case of AM60-26%  $(\text{Al}_2\text{O}_3)_f$  causing a loss of wear resistance-as can be explained by Eqn.5.25.

The sequence of damage events might be understood from Fig.5.8 where it is evident that in the initial sliding cycles the decrease in fibre length, due to fibre fracture and fragmentation, is predominant. At higher sliding cycles the decrease in height due to sinking in of the comminuted fibres dominates. Thus fibre sinking in process is preceded by fracture and fragmentation. Comparing Fig.5.8 with Eqn.5.24 and Table 5-6 shows that the final length of the fragmented  $\text{Al}_2\text{O}_3$  fibre calculated from the theoretical considerations matches well with the experimental findings indicated in Fig.5.8.

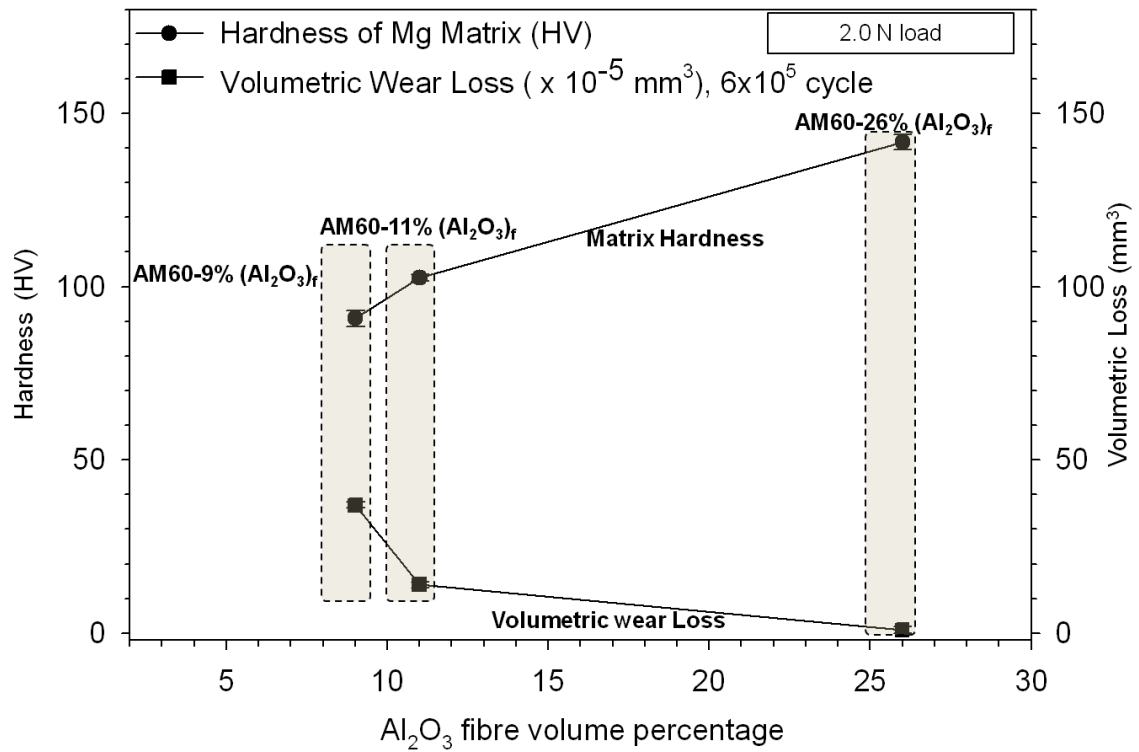


Fig.5.6. Plot of matrix hardness and volumetric wear loss after  $6 \times 10^5$  cycles at 2.0 N load for AM60-9% (Al<sub>2</sub>O<sub>3</sub>)<sub>f</sub>, AM60-11% (Al<sub>2</sub>O<sub>3</sub>)<sub>f</sub> and AM60-26% (Al<sub>2</sub>O<sub>3</sub>)<sub>f</sub>. The extent of wear resistance expected due to the high matrix hardness of AM60-26% (Al<sub>2</sub>O<sub>3</sub>)<sub>f</sub> is not observed.

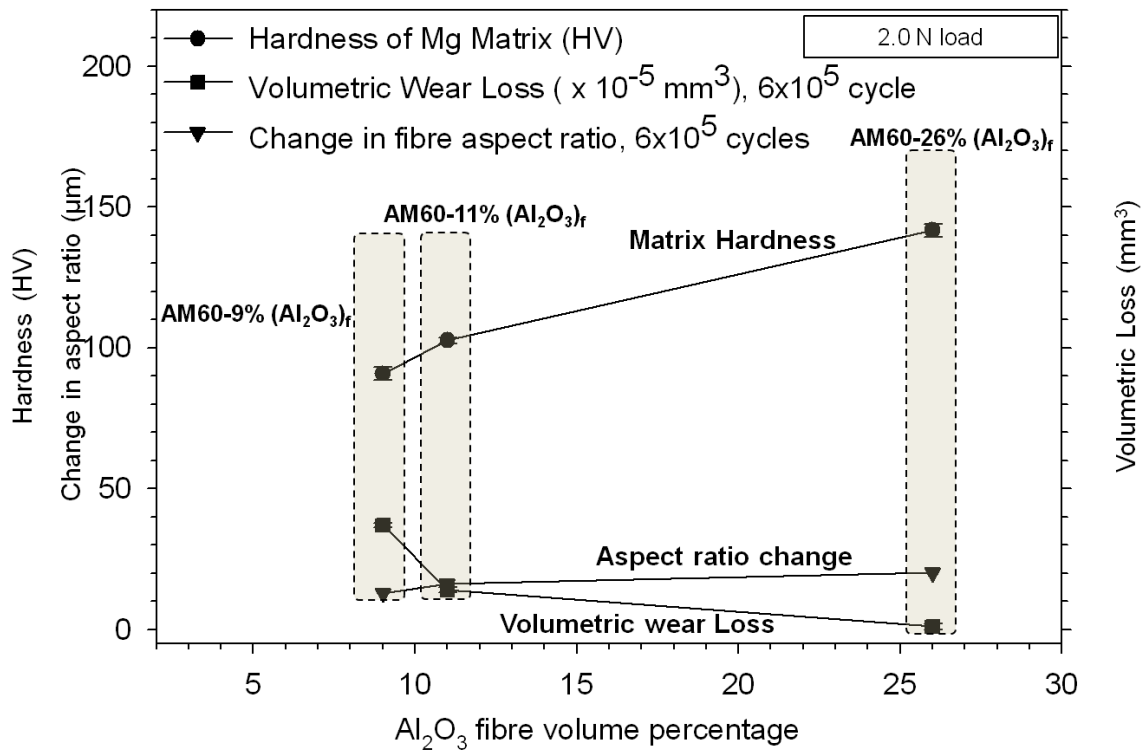


Fig.5.7. Plot of matrix hardness, volumetric wear loss (after  $6 \times 10^5$  cycles) and change in aspect ratio for AM60-9% ( $\text{Al}_2\text{O}_3$ )<sub>f</sub>, AM60-11% ( $\text{Al}_2\text{O}_3$ )<sub>f</sub> and AM60-26% ( $\text{Al}_2\text{O}_3$ )<sub>f</sub> after  $6 \times 10^5$  cycles at 2.0 N load. The low wear resistance of AM60-26% ( $\text{Al}_2\text{O}_3$ )<sub>f</sub> might be explained by highest change in aspect ratio due to fracture and fragmentation.

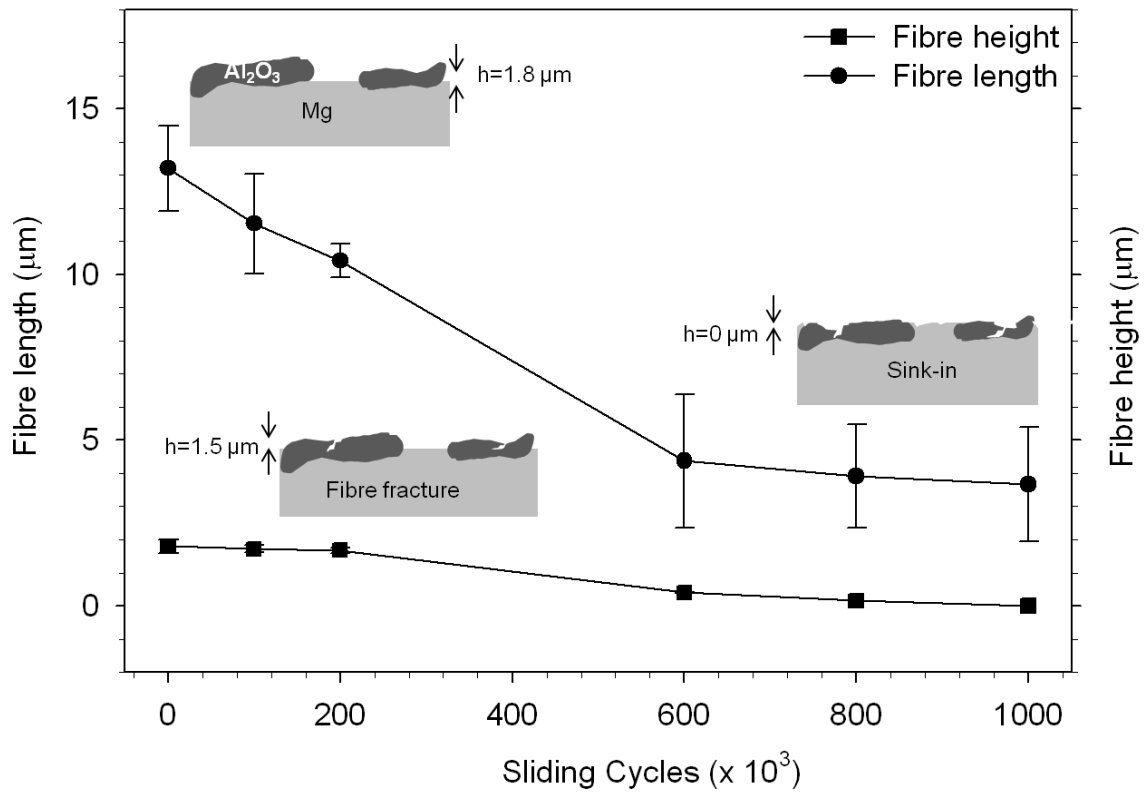


Fig.5.8. Plot of decrease of Al<sub>2</sub>O<sub>3</sub> fibre length and fibre height with sliding cycles for AM60-9% (Al<sub>2</sub>O<sub>3</sub>)<sub>f</sub> at 2.0 N load indicating the predominance of fracture and fragmentation in the initial sliding cycles; sinking in of the fragmented fibres is observed at higher sliding cycles; 'h' represents the Al<sub>2</sub>O<sub>3</sub> fibre elevation.



## 5.6. Comparison with Al-Si alloys and role of oil residue layer

It is essential to compare the wear performance of the Al-11% Si and Al-18.5% Si alloys with the Mg composites to understand the role of microstructure in the prevalent wear mechanisms. Both the eutectic Al-11% Si and hypereutectic Al-18.5% Si alloy are materials used for automotive engines and their wear mechanisms are well established. This comparison will be insightful in applications of Mg based composites in the engine powertrain system.

A comparison of the G-T plots of Al-18.5% Si alloy and AM60-9% (Al<sub>2</sub>O<sub>3</sub>)<sub>f</sub> is represented in Fig.5.9 where the maximum contact pressure on AM60-9% (Al<sub>2</sub>O<sub>3</sub>)<sub>f</sub> is higher than the Al-18.5% Si alloy by 65%. Fig.5.10 reveals that a higher maximum contact pressure on AM60-9% (Al<sub>2</sub>O<sub>3</sub>)<sub>f</sub> as compared to Al-18.5% Si alloy results in higher amount of material loss from the Mg composite. The contact pressure applied on Al-11% Si was also calculated using Eqn.5.18/5.19 and compared with those obtained for the Mg composite AM60-9% (Al<sub>2</sub>O<sub>3</sub>)<sub>f</sub>. Under the same load of 1.0 N the highest contact pressure on Al-11% Si was calculated to be approximately 2.5 GPa [11] which is 1.12 times lower than that on AM60-9% (Al<sub>2</sub>O<sub>3</sub>)<sub>f</sub>. Consequently volumetric wear loss from the AM60-9% (Al<sub>2</sub>O<sub>3</sub>)<sub>f</sub> is more than that detected in Al-11% Si (Fig.5.11). In the initial sliding cycles the Mg composite shows better wear performance than the Al-11% Si alloy. However, at longer sliding cycles, volumetric wear stabilizes for the Al-11% Si alloy due to the formation of the oil residue layer. No such protective tribofilm formation is observed for the Mg composite AM60-9% (Al<sub>2</sub>O<sub>3</sub>)<sub>f</sub> at room temperature.

However, tests conducted on AM60-9% (Al<sub>2</sub>O<sub>3</sub>)<sub>f</sub> at 100 °C indicated the presence of an oil residue layer (ORL). A cross-sectional TEM image of the worn AM60-

9%  $(\text{Al}_2\text{O}_3)_f$  surface at 100 °C and taken after sliding for  $1 \times 10^6$  cycles and 1.0 N load indicates the presence of the oil residue layer (Fig.5.12) on tops of  $\text{Al}_2\text{O}_3$  fibres. The composition of the oil residue layer is indicated in the corresponding EDS observations in Fig.5.12. The oil residue layer was  $54.8 \pm 6.6$  nm thick on the  $\text{Al}_2\text{O}_3$  fibre. At 1.0 N load no ORL formation was observed on the Mg matrix. Formation of ORL on top of the worn Mg matrix and the formation of ultrafine nano Mg grains in the immediate subsurface region was detected (Fig.5.13), from cross-sectional TEM image, on the worn AM60-9%  $(\text{Al}_2\text{O}_3)_f$  surface at 100 °C after  $1 \times 10^6$  cycles and 2.0 N load. The formation of the ultrafine Mg nano-grains, supporting the oil residue layer, might be attributed to deformation due to high subsurface strains prevalent under conditions when the Mg matrix is in contact with the counterface. An investigation into the formative mechanisms of the oil residue layer and its composition will be the next step for this research.

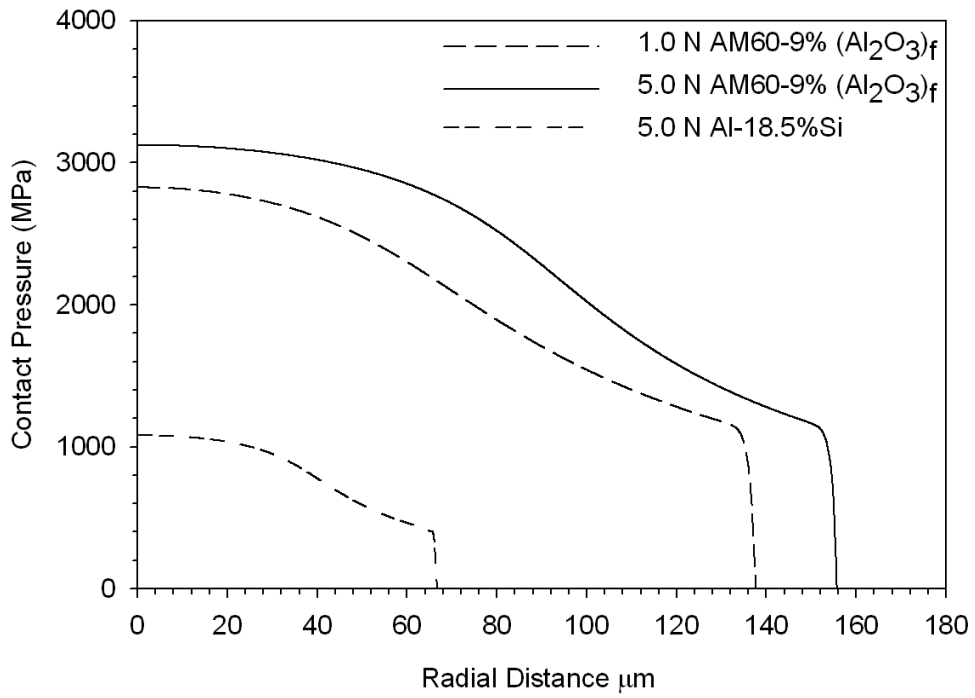


Fig.5.9. Comparison of Greenwood-Tripp plot for AM60-9% (Al<sub>2</sub>O<sub>3</sub>)<sub>f</sub> and Al-18.5% Si at 5.0 N load (25 °C) indicating the considerably higher applied contact pressure for the Mg composite compared AM60-9% (Al<sub>2</sub>O<sub>3</sub>)<sub>f</sub> to Al-18.5% Si under the same conditions.

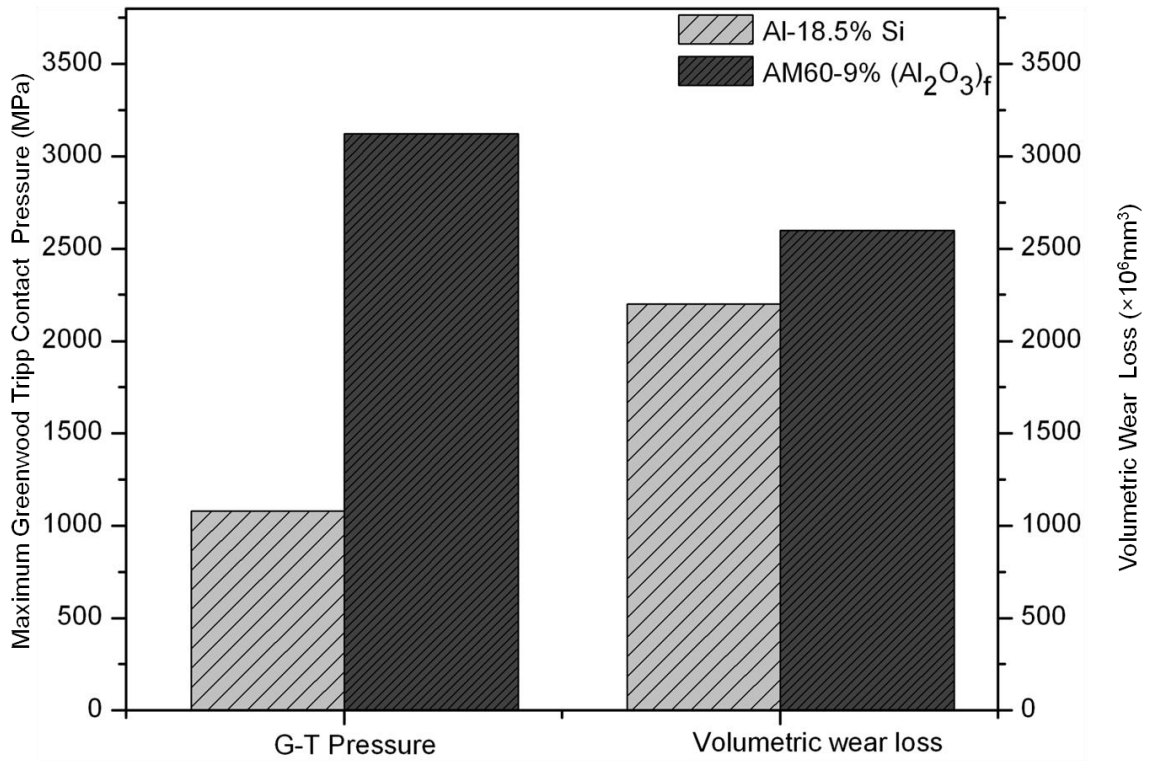


Fig.5.10. Comparison of the maximum G-T contact pressure and the corresponding volumetric wear loss at 5.0 N load and  $2 \times 10^5$  sliding cycles. AM60-9% ( $\text{Al}_2\text{O}_3$ )<sub>f</sub> shows a higher rate of material loss due to the higher maximum contact pressure on it compared to the Al-18.5% Si alloy.

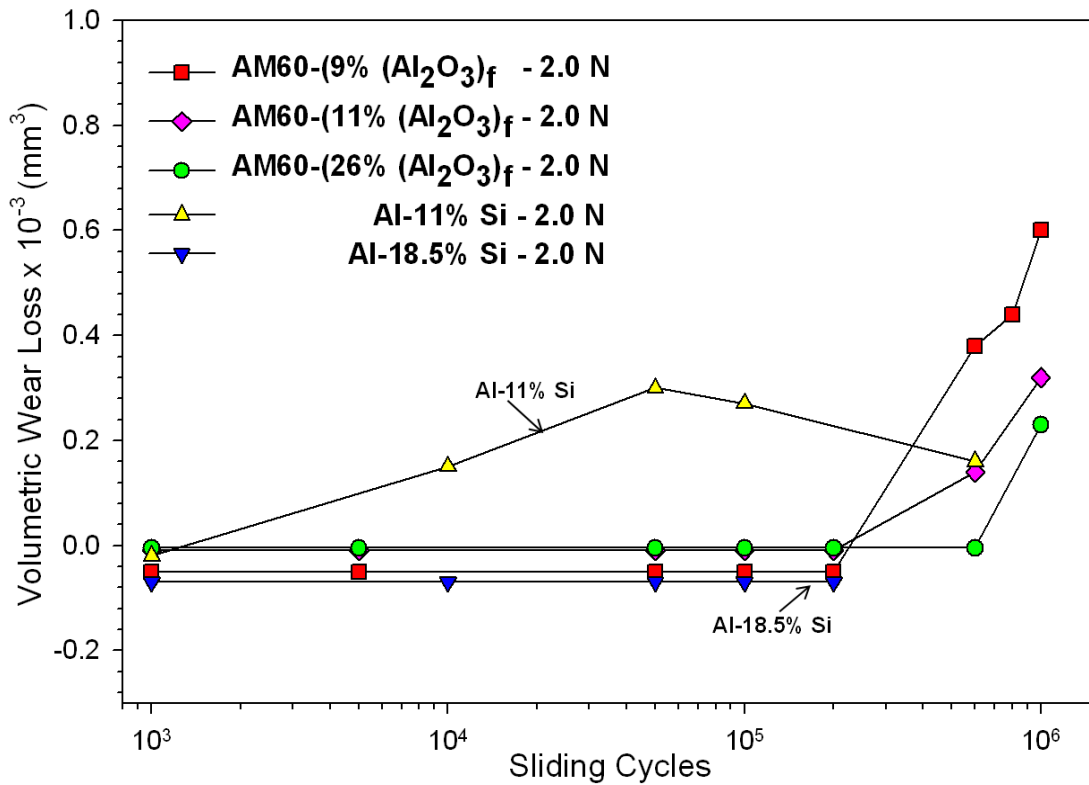


Fig.5.11. Comparison of the volumetric wear loss vs. sliding cycles (at 25 °C) plot for eutectic and hypereutectic Al-Si alloys with the Mg composites. It is to be noted that wear stabilization is observed in the case of Al-11% Si alloy due to the formation of the oil residue layer.

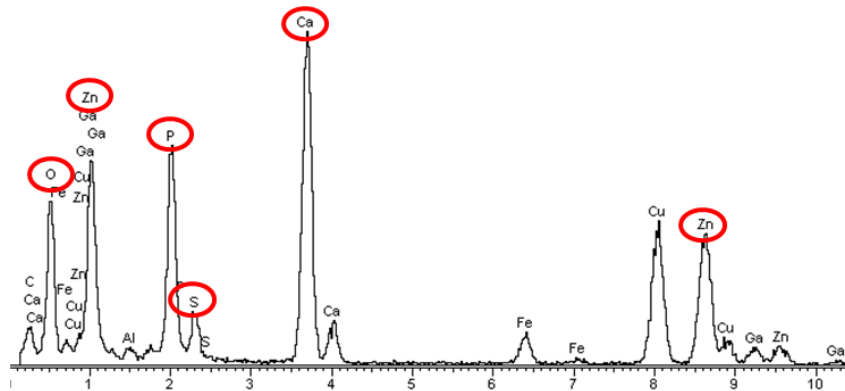
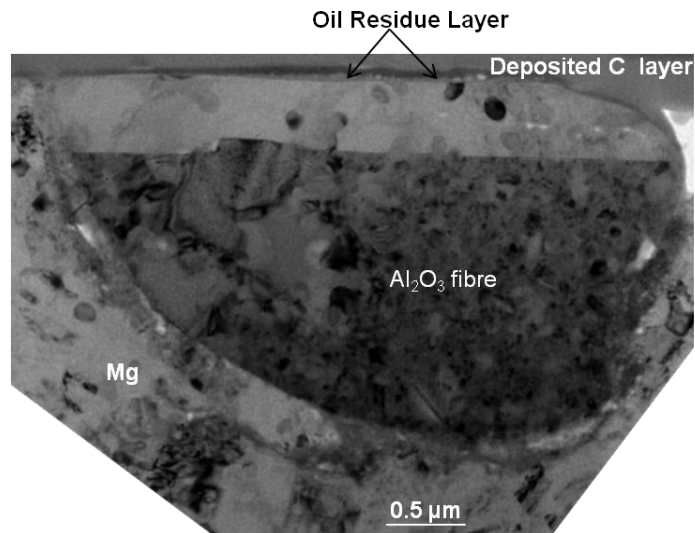


Fig.5.12. Cross-sectional TEM image of the microstructure of the subsurface material under the wear track, tested at 1.0 N load and 100 °C, showing formation of oil residue layer on top of Al<sub>2</sub>O<sub>3</sub> fibres. Corresponding EDS analysis of the oil residue layer show the constituent elements of the oil residue layer to be Zn, P, S, Ca and C.

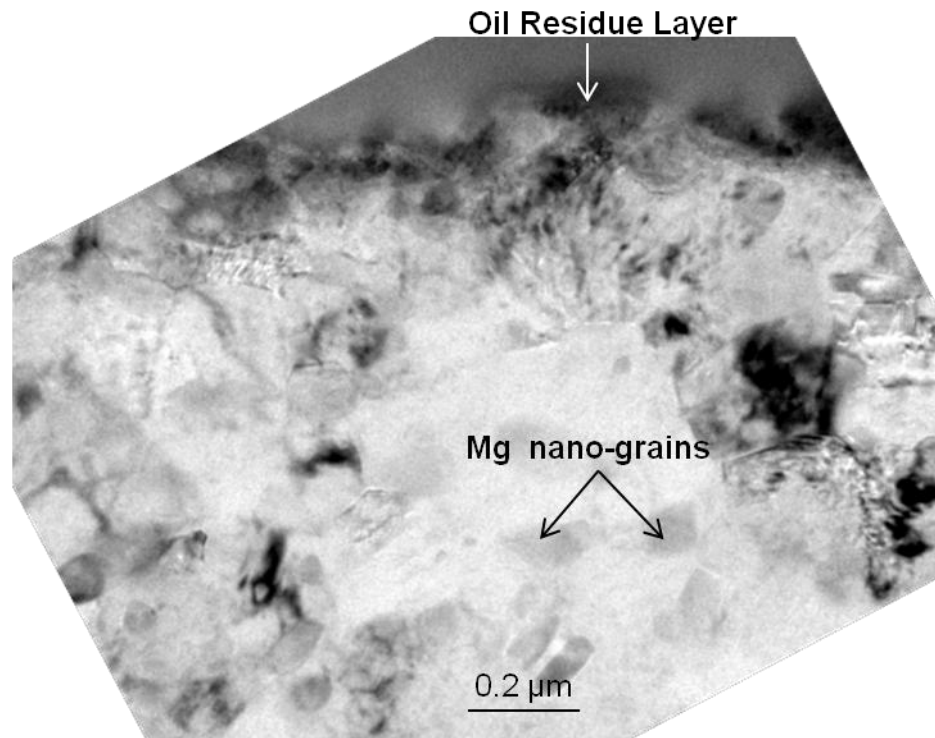


Fig.5.13. Cross-sectional TEM micrograph of the subsurface material under the wear track, tested at 100 °C and 2.0 N load, showing formation of continuous oil residue layer on the worn Mg matrix. Immediately below the layer presence of Mg nano-grains were detected.

## Chapter 6: Summary and Conclusions

### 6.1. Summary

Lubricated pin-on-disk sliding wear tests were performed on matrix alloy AM60, particle and fibre reinforced Mg composites at a load range of 1.0-5.0 N and at 25 °C and 100 °C to evaluate the wear mechanisms. The main findings are as follows:

i) Magnesium matrix composites were developed using saffil fibre/particle preform fabrication and a squeeze casting technique. This process involved application of a constant high (90 MPa) pressure for a stipulated period of time (90 s) on the preheated preform and the molten Mg matrix to fabricate Mg composites with uniform reinforcement distribution.

ii) Wear mechanisms of magnesium alloy, AM60, at 1.0 N consisted of damage by surface plastic deformation and oxidative+adhesive type wear. Material removal rate for the AM60 alloy,  $5.67 \times 10^{-4} \text{ mm}^3/\text{m}$ , indicated occurrence of mild wear throughout test conditions. Transfer of magnesium oxide particles from the alloy to the counterface was detected. Comparison with the wear rate of the Mg composite AM60-9%  $(\text{Al}_2\text{O}_3)_f$  worn at 5.0 N indicated that the highest wear rate was  $1.82 \times 10^{-6} \text{ mm}^3/\text{m}$  which was of the order of  $10^2$  times lower than that of the AM60 alloy.

iii) Wear of the composite AM60-9%  $(\text{Al}_2\text{O}_3)_f$  occurred in the UMW regime under the experimental conditions and followed a non-linear behaviour. At 25 °C damage occurred during sliding wear in the following ways: a) In the initial sliding cycles the exposed  $\text{Al}_2\text{O}_3$  fibre fractured and fragmented into shorter fibres, b) the  $\text{Al}_2\text{O}_3$  fibre height reduced due to sinking in of the fragmented fibres and c) as the  $\text{Al}_2\text{O}_3$  fibre and the Mg matrix



reached the same elevation, the matrix suffered damage due to the counterface. No protective tribolayer formation was detected on the worn surface, indicating that the damage was accumulative.

iv) Wear of all composites was negligible and comparable for low sliding cycles. AM60-9%  $(\text{Al}_2\text{O}_3)_f$  showed the highest rate of material loss as compared to AM60-11%  $(\text{Al}_2\text{O}_3)_f$  and AM60-26%  $(\text{Al}_2\text{O}_3)_f$ . Although an increase in the volume percentage of  $\text{Al}_2\text{O}_3$  fibres led to a decrease in the material loss from the Mg matrix composites, it also enhanced the damage to the counterface. Also greater fibre fracture and fragmentation was observed with increase in fibre volume percentage.

v) The contact pressure on the tops of  $\text{Al}_2\text{O}_3$  fibres was estimated using modified Greenwood-Tripp contact mechanics model where the exposed  $\text{Al}_2\text{O}_3$  fibres were considered as asperities. The contact pressure was found to be the highest, 3.124 GPa under 5.0 N load, at the centre of the wear track. This exceeded the hardness of the Mg matrix and the compressive strength of  $\text{Al}_2\text{O}_3$  fibre causing plastic deformation to the Mg matrix and fibre fracture under all loading conditions.

vi) The wear mechanisms were rationalized by the following considerations: the normal applied pressure on the  $\text{Al}_2\text{O}_3$  fibres, estimated using Greenwood-Tripp contact model, was counterbalanced by the matrix hardening effect due to increase in dislocation density as a result of fibre addition and high strain deformation in the subsurface. A critical fibre length was calculated which determined the lower limit of the fibre fragmentation size. Also, it was shown that the fibre fragmentation was directly proportional to the fibre length. All of this corroborated well with the experimental findings. Thus, for future

design of composites, use of short fibres ( $\leq 3 \mu\text{m}$ ) would reduce the propensity for fracture and might lead to higher wear resistance.

vii) For the sliding wear tests performed at  $100^\circ\text{C}$  following features were observed: At low load (1.0 N) the  $\text{Al}_2\text{O}_3$  fibre reduction was delayed, relative to the room temperature observations, due to formation of a protective tribofilm on tops of  $\text{Al}_2\text{O}_3$  fibres. At higher loads the tribofilm formed on the worn Mg matrix thus leading to reduced volumetric wear loss as compared to the room temperature counterpart. The tribolayer, also known as the oil residue layer consisted comprised of Zn, P, S, Ca and C all of which were assumed to originate from the breakdown of ZDDP additive in the lubricant.

## 6.2 Conclusions

It will be useful to discuss the conclusions arising out of this research by describing the factors effective in delaying the damage process to the Mg matrix and the resulting increase to higher rate of volumetric wear loss. The factors, represented in a bar chart (Fig.6.1), are i) increasing fibre volume percent and ii) increasing the operating temperature to  $100^\circ\text{C}$ .

Fig.6.1 shows that decreasing the applied load from 5.0-2.0 N increases the transitional sliding cycle from  $1 \times 10^5$  cycles to  $6 \times 10^5$  cycles. This can be rationalized by the increase in contact pressure on the  $\text{Al}_2\text{O}_3$  fibres as a result of increase in load leading to fracture of fibres. Increasing the  $\text{Al}_2\text{O}_3$  fibre content from 9 vol%-26 vol% delayed the transition from  $6 \times 10^5$  cycles to  $1 \times 10^6$  cycles as a result of increase in the number of load bearing elements. However, higher fibre content also increased the damage to the counterface (Fig.6.1). Elevated temperature tests showed a delayed transition to higher

rate of volumetric wear loss from  $6 \times 10^5$  cycles to  $1 \times 10^6$  cycles due to the formation of the oil residue layer on tops of worn  $\text{Al}_2\text{O}_3$  fibre and Mg matrix supported by ultrafine Mg grains. Also tests conducted at  $100^\circ\text{C}$  indicated volumetric wear loss even lower than those obtained for AM60-26%  $(\text{Al}_2\text{O}_3)_f$  under the same test conditions (Fig.6.1).

Thus, an optimum operating conditions for the Mg composite AM60-9%  $(\text{Al}_2\text{O}_3)_f$  is wear at 1.0 N load and  $100^\circ\text{C}$  where it is expected to show a favourable long term wear performance.

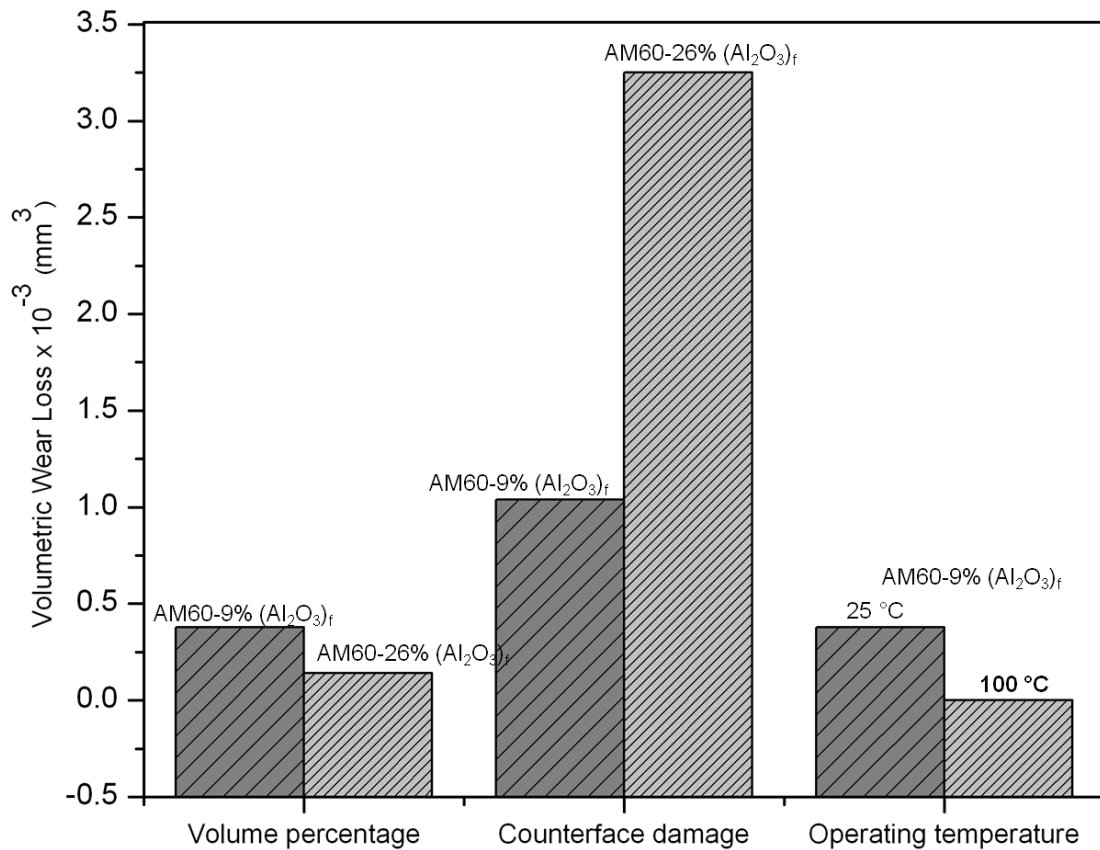


Fig.6.1. Plot of variation of volumetric wear loss with change in Al<sub>2</sub>O<sub>3</sub> fibre volume percentage and operating temperature. Increasing the fibre volume percentage from 9% (AM60-9% (Al<sub>2</sub>O<sub>3</sub>)<sub>f</sub>) to 26% (AM60-26% (Al<sub>2</sub>O<sub>3</sub>)<sub>f</sub>) decreased the volumetric wear loss ( $0.379 \times 10^{-3} \text{ mm}^3 - 0.14 \times 10^{-3} \text{ mm}^3$ ) but increased the damage to the counterface. At 100 °C AM60-9% (Al<sub>2</sub>O<sub>3</sub>)<sub>f</sub> showed comparable wear resistance to that of AM60-26% (Al<sub>2</sub>O<sub>3</sub>)<sub>f</sub> proving to be the optimum operating condition.

### **6.3 Future work**

The understanding of ultra-mild wear mechanisms in Al-Si alloys prompted the study of ultramild wear in Mg composites. This research helped understand the wear behaviour of Mg composites under ultra-mild wear conditions. However, further studies on the following points would help development and implementation of Mg composites for use as engine block in small or hybrid cars:

- i) A study of wear of Mg composites against alternate counterface materials, namely carbon-carbon composites, to prevent the damage of the counterface by hard reinforcements.
- ii) An analysis of the oil residue layer formative mechanisms and their dependence on contact pressure and temperature. Also the mixing of the components of the oil residue layer with the substrate (Mg and Al) will be an interesting and useful study.
- iii) Study of corrosion and fatigue behaviour of the Mg composites to better understand their applicability as engine blocks.

## References

- [1] GS Cole, AM Sherman. Light weight materials for automotive applications, *Mater Charact.* 35 (1995) 3-9.
- [2] H Friedrich, S Schumann. Research for a "new age of magnesium" in the automotive industry, *J.Mater.Process.Technol.* 117 (2001) 276-281.
- [3] SC Tung, ML McMillan. Automotive tribology overview of current advances and challenges for the future, *Tribol.Int.* 37 (2004) 517-536.
- [4] EP Becker. Trends in tribological materials and engine technology, *Tribol.Int.* 37 (2004) 569-575.
- [5] EG Jacobsen, General Motors 390 Aluminum Alloy 60 degree V6 Engine. SAE Special Publications. (1983) 29-34.
- [6] E Aghion, B Bronfin, D Eliezer. The role of the magnesium industry in protecting the environment, *J.Mater.Process.Technol.* 117 (2001) 381-385.
- [7] BL Mordike, T Ebert. Magnesium: Properties — applications — potential, *Materials Science and Engineering: A.* 302 (2001) 37-45.
- [8] S Huang, Y Jeng, VI Semenov, Y- Dai. Particle size effects of silicon carbide on wear behavior of SiC p-reinforced magnesium matrix composites, *Tribology Letters.* 42 (2011) 79-87.
- [9] CM Taylor. Automobile engine tribology-design considerations for efficiency and durability, *Wear.* 221 (1998) 1-8.
- [10] M Scherge, K Pöhlmann, A Gervé. Wear measurement using radionuclide-technique (RNT), *Wear.* 254 (2003) 801-817.
- [11] M Chen, X Meng-Burany, TA Perry, AT Alpas. Micromechanisms and mechanics of ultra-mild wear in Al-Si alloys, *Acta Materialia.* 56 (2008) 5605-5616.
- [12] JF Archard, W Hirst. The Wear of Metals under Unlubricated Conditions, *Proceedings of the Royal Society of London.Series A, Mathematical and Physical Sciences.* 236 (1956) pp. 397-410.
- [13] JF Archard. Contact and rubbing of flat surfaces, *J.Appl.Phys.* 24 (1953) 981-988.

- [14] JF Archard, W Hirst. An Examination of a Mild Wear Process, Proceedings of the Royal Society of London. Series A, Mathematical and Physical Sciences. 238 (1957) pp. 515-528.
- [15] JK Lancaster. The Formation of Surface Films at the Transition between Mild and Severe Metallic Wear, Proceedings of the Royal Society of London. Series A, Mathematical and Physical Sciences. 273 (1963) pp. 466-483.
- [16] W Hirst, JK Lancaster. The Influence of Speed on Metallic Wear, Proceedings of the Royal Society of London. Series A, Mathematical and Physical Sciences. 259 (1960) pp. 228-241.
- [17] AR Riahi, AT Alpas. Wear map for grey cast iron, Wear. 255 (2003) 401-409.
- [18] W Hirst, JK Lancaster. Surface film formation and metallic wear, J. Appl. Phys. 27 (1956) 1057-1065.
- [19] AD Sarkar. Wear of aluminium-silicon alloys, Wear. 31 (1975) 331-343.
- [20] AS Reddy, BNP Bai, KSS Murthy, SK Biswas. Wear and seizure of binary AlSi alloys, Wear. 171 (1994) 115-127.
- [21] J Zhang, AT Alpas. Transition between mild and severe wear in aluminium alloys, Acta Materialia. 45 (1997) 513-528.
- [22] BK Yen, T Ishihara. Effect of humidity on friction and wear of Al-Si eutectic alloy and Al-Si alloy-graphite composites, Wear. 198 (1996) 169-175.
- [23] M Elmadagli, AT Alpas. Sliding wear of an Al-18.5 wt.% Si alloy tested in an argon atmosphere and against DLC coated counterfaces, Wear. 261 (2006) 823-834.
- [24] BN Pramila Bai, SK Biswas. Characterization of dry sliding wear of Al-Si alloys, Wear, 120 (1987) 61-74.
- [25] J Clarke, AD Sarkar. Wear characteristics of as-cast binary aluminium-silicon alloys, Wear. 54 (1979) 7-16.
- [26] F Wang, H Liu, Y Ma, Y Jin. Effect of Si content on the dry sliding wear properties of spray-deposited Al-Si alloy, Materials and Design. 25 (2004) 163-166.
- [27] M Elmadagli, T Perry, AT Alpas. A parametric study of the relationship between microstructure and wear resistance of Al-Si alloys, Wear. 262 (2007) 79-92.

- [28] M Elmadagli, AT Alpas. Progression of wear in the mild wear regime of an Al-18.5% Si (A390) alloy, *Wear*. 261 (2006) 367-381.
- [29] H Chen, AT Alpas. Sliding wear map for the magnesium alloy Mg-9Al-0.9 Zn (AZ91), *Wear*. 246 (2000) 106-116.
- [30] NN Aung, W Zhou, LEN Lim. Wear behaviour of AZ91D alloy at low sliding speeds, *Wear*. 265 (2008) 780-786.
- [31] J An, RG Li, Y Lu, CM Chen, Y Xu, X Chen, et al. Dry sliding wear behavior of magnesium alloys, *Wear*. 265 (2008) 97-104.
- [32] WD Callister Jr. *Materials science and engineering, An Introduction*, John Wiley & Sons, Inc. Third Avenue, New York (2001).
- [33] A Luo. Processing, microstructure, and mechanical behavior of cast magnesium metal matrix composites, *Metallurgical and Materials Transactions A*. 26 (1995) 2445-2455.
- [34] Q Zhang, H Hu, J Lo, Solidification of discontinuous Al<sub>2</sub>O<sub>3</sub> fiber reinforced magnesium (AM60) matrix composite, *Defect and Diffusion Forum*. 312-315 (2011) 277-282.
- [35] Z Wang, RJ Zhang. Mechanical behavior of cast particulate SiC/Al (A356) metal matrix composites, *Metallurgical Transactions A*. 22 (1991) 1585-1593.
- [36] A Luo. Development of matrix grain structure during the solidification of a Mg(Az91) SiCP composite, *Scripta Metallurgica et Materiala*. 31 (1994) 1253-1258.
- [37] EO Hall. Variation of hardness of metals with grain size [5], *Nature*. 173 (1954) 948-949.
- [38] GE Dieter. *Mechanical Metallurgy*. JR. McGraw-Hill Book Company, INC. New York, Toronto, London 1961, 189.
- [39] Z Trojanová, Z Drozd, S Kúdela, Z Száraz, P Lukáč. Strengthening in Mg-Li matrix composites, *Composites Sci.Technol*. 67 (2007) 1965-1973.
- [40] H Fukuda, T Chou. An advanced shear-lag model applicable to discontinuous fiber composites, *J.Composite Mater*. 15 (1981) 179-191.
- [41] VC Nardone, KM Prewo. On the strength of discontinuous silicon carbide reinforced aluminum composites, *Scripta Metallurgica*. 20 (1986) 43-48.



- [42] E Orowan. Fracture and strength of solids, Reports on Progress in Physics. 12 (1949) 185-232.
- [43] DA Rigney. Transfer, mixing and associated chemical and mechanical processes during the sliding of ductile materials, Wear. 119 (1987) 369-390.
- [44] XY Li, KN Tandon. Microstructural characterization of mechanically mixed layer and wear debris in sliding wear of an Al alloy and an Al based composite, Wear. 245 (2000) 148-161.
- [45] XY Li, KN Tandon. Mechanical mixing induced by sliding wear of an Al-Si alloy against M2 steel, Wear. 225-229 (1999) 640-648.
- [46] AR Riahi, AT Alpas. The role of tribo-layers on the sliding wear behavior of graphitic aluminum matrix composites, Wear. 250-251 (2001) 1396-1407.
- [47] A Alahelisten, F Bergman, M Olsson, S Hogmark. On the wear of aluminium and magnesium metal matrix composites, Wear. 165 (1993) 221-226.
- [48] SC Sharma, B Anand, M Krishna. Evaluation of sliding wear behaviour of feldspar particle-reinforced magnesium alloy composites, Wear. 241 (2000) 33-40.
- [49] L Falcon-Franco, E Bedolla-Becerril, J Lemus-Ruiz, JG Gonzalez-Rodríguez, R Guardian, I Rosales. Wear performance of TiC as reinforcement of a magnesium alloy matrix composite, Composites Part B: Engineering. 42 (2011) 275-279.
- [50] AT Alpas, JD Embury. Sliding and abrasive wear behaviour of an aluminum (2014)-SiC particle reinforced composite, Scripta Metallurgica et Materiala. 24 (1990) 931-935.
- [51] AT Alpas, J Zhang. Effect of SiC particulate reinforcement on the dry sliding wear of aluminium-silicon alloys (A356), Wear. 155 (1992) 83-104.
- [52] S Wilson, AT Alpas. Wear mechanism maps for metal matrix composites, Wear. 212 (1997) 41-49.
- [53] B Hu, L Peng, W Ding. Dry sliding wear behavior of Saffil fiber-reinforced Mg-10Gd-3Y-0.5Zr magnesium alloy-based composites, J.Composite Mater. 45 (2011) 683-693.
- [54] CYH Lim, SC Lim, M Gupta. Wear behaviour of SiCp-reinforced magnesium matrix composites, Wear. 255 (2003) 629-637.

[55] SK Jo, WJ Lee, YH Park, IM Park. Effect of SiC particle size on wear properties of Al<sub>2</sub>O<sub>3</sub>•SiO<sub>2</sub>/SiC/Mg hybrid metal matrix composites, Tribology Letters. 45 (2012) 101-107.

[56] KC Ludema. A review of scuffing and running-in of lubricated surfaces, with asperities and oxides in perspective, Wear. 100 (1984) 315-331.

[57] BE Slattery, T Perry, A Edrissy. Microstructural evolution of a eutectic Al-Si engine subjected to severe running conditions, Materials Science and Engineering A. 512 (2009) 76-81.

[58] M Dienwiebel, K Pöhlmann, M Scherge. Origins of the wear resistance of AlSi cylinder bore surfaces studied by surface analytical tools, Tribol.Int. 40 (2007) 1597-1602.

[59] M Chen, AT Alpas, Ultra-mild wear of aluminum alloys: Role of silicon particles, Proceedings of STLE/ASME International Joint Tribology Conference, IJTC (2006).

[60] M Chen, AT Alpas. Ultra-mild wear of a hypereutectic Al-18.5 wt.% Si alloy, Wear. 265 (2008) 186-195.

[61] M Chen, T Perry, AT Alpas. Ultra-mild wear in eutectic Al-Si alloys, Wear. 263 (2007) 552-561.

[62] SK Dey, MJ Lukitsch, MP Balogh, X Meng-Burany, AT Alpas. Ultra-mild wear mechanisms of Al-12.6wt.% Si alloys at elevated temperature, Wear. 271 (2011) 1842-1853.

[63] SK Dey, TA Perry, AT Alpas. Micromechanisms of low load wear in an Al-18.5% Si alloy, Wear. 267 (2009) 515-524.

[64] X Meng-Burany, TA Perry, AK Sachdev, AT Alpas. Subsurface sliding wear damage characterization in Al-Si alloys using focused ion beam and cross-sectional TEM techniques, Wear. 270 (2011) 152-162.

[65] DA Hughes, N Hansen. High angle boundaries formed by grain subdivision mechanisms, Acta Materialia. 45 (1997) 3871-3886.

[66] PJ Apps, JR Bowen, PB Prangnell. The effect of coarse second-phase particles on the rate of grain refinement during severe deformation processing, Acta Materialia. 51 (2003) 2811-2822.

[67] M Ortiz, EA Repetto, L Stainier. Theory of subgrain dislocation structures, J.Mech.Phys.Solids. 48 (2000) 2077-2114.

[68] SD Terhune, D Swisher, K Oh-Ishi, Z Horita, TG Langdon, TR McNelley. An investigation of microstructure and grain-boundary evolution during ECA pressing of pure aluminum, *Metall Mat Trans A Phys Metall Mat Sci.* 33 (2002) 2173-2184.

[69] IM Hutchings, *Tribology, Friction and Wear of Engineering Materials*, CRC Press, Boca Raton, (1996) 77-105.

[70] GM Bancroft, M Kasrai, M Fuller, Z Yin, K Fyfe, KH Tan. Mechanisms of tribochemical film formation: Stability of tribo- and thermally-generated ZDDP films, *Tribology Letters.* 3 (1997) 47-51.

[71] ML Suominen Fuller, L Rodriguez Fernandez, GR Massoumi, WN Lennar, M Kasrai, GM Bancroft. The use of x-ray absorption spectroscopy for monitoring the thickness of antiwear films from ZDDP, *Tribology Letters.* 8 (2000) 187-192.

[72] Z Yin, M Kasrai, M Fuller, GM Bancroft, K Fyfe, KH Tan. Application of soft X-ray absorption spectroscopy in chemical characterization of antiwear films generated by ZDDP Part I: The effects of physical parameters, *Wear.* 202 (1997) 172-191.

[73] H Spikes. The history and mechanisms of ZDDP, *Tribology Letters.* 17 (2004) 469-489.

[74] Y Wan, L Cao, Q Xu. Friction and wear characteristics of ZDDP in the sliding of steel against aluminum alloy, *Tribol.Int.* 30 (1997) 767-772.

[75] M Fuller, M Kasrai, JS Sheasby, GM Bancroft, K Fyfe, KH Tan. X-ray absorption spectroscopy of antiwear films on aluminum alloys generated from zinc dialkyldithiophosphate, *Tribology Letters.* 1 (1995) 367-378.

[76] MA Nicholls, PR Norton, GM Bancroft, M Kasrai. X-ray absorption spectroscopy of tribofilms produced from zinc dialkyl dithiophosphates on Al-Si alloys, *Wear.* 257 (2004) 311-328.

[77] JA Schey. *Tribology in Metal Working*, American Society for Metals, Metals Park, Ohio 44073 (1983).

[78] MA Nicholls, T Do, PR Norton, M Kasrai, GM Bancroft. Review of the lubrication of metallic surfaces by zinc dialkyl-dithiophosphates, *Tribol.Int.* 38 (2005) 15-39.

[79] PA Willermet, RO Carter III, EN Boulos. Lubricant-derived tribochemical films-An infra-red spectroscopic study, *Tribol.Int.* 25 (1992) 371-380.

- [80] HZ Ye, YL Xing. Review of recent studies in magnesium matrix composites, *J.Mater.Sci.* 39 (2004) 6153-71.
- [81] A Yu, S Wang, N Li, H Hu. Pressurized solidification of magnesium alloy AM50A, *J.Mater.Process.Technol.* 191 (2007) 247-250.
- [82] M Baucio. "ASM Metals Reference Book," Third Edition, ASM International, Metals Park, Ohio (1993).
- [83] B Bhushan. *Principles and Applications of Tribology*, New York: Wiley. (1999) 201-202.
- [84] KL Johnson. *Contact mechanics*, New York, Cambridge Press, (1985) 416-422.
- [85] ML Baucio. *ASM engineered materials reference book*, ASM International, Ohio, United States of America. (1994).
- [86] JA Greenwood, JH Tripp. The elastic contact of rough spheres, *Transactions of the ASME.Series E, Journal of Applied Mechanics.* 34 (1967) 153-159.
- [87] IM Hutchings. The contributions of David Tabor to the science of indentation hardness, *J.Mater.Res.* 24 (2009) 581-589.
- [88] D Tabor. *The Hardness of Metals*. Oxford, Oxford University Press (1951) 46-51.
- [89] HE Dève. Compressive strength of continuous fiber reinforced aluminum matrix composites, *Acta Materialia.* 45 (1997) 5041-5046.
- [90] N Ramakrishnan. An analytical study on strengthening of particulate reinforced metal matrix composites, *Acta Materialia.* 44 (1996) 69-77.
- [91] MM Avedesian, H Baker. *Magnesium and Magnesium Alloys*, ASM Specialty Handbook, ASM International, September 1999 (Second Printing). (2009).
- [92] K Maruyama, M Suzuki, H Sato. Creep strength of magnesium-based alloys, *Metall Mat Trans A Phys Metall Mat Sci.* 33 (2002) 875-882.
- [93] AR Riahi, AT Alpas. Fracture of silicon-rich particles during sliding contact of Al-Si alloys, *Materials Science and Engineering A.* 441 (2006) 326-330.

## Vita Auctoris

Name: Anindya Banerji

Place of Birth: Kolkata, West Bengal, India

Year of Birth: 1986

Educaion: Bachelor of Science (B.Sc.), Chemistry (Hons.), St. Xavier's College, Kolkata, West Bengal, India. 2005-2008.

Master of Science (M.Sc.), Chemistry (Organic Chemistry Specialization), St. Stephen's College, University of Delhi, Delhi, India. 2008-2010.

Master of Applied Science (M.A.Sc.), Engineering Materials, University of Windsor, Windsor, Ontario, Canada. 2010-2012.

### Refereed Journal Publications

1. Banerji A., Hu H., Alpas A.T., "Ultramild wear of Al<sub>2</sub>O<sub>3</sub> fibre and particle reinforced magnesium matrix composites", *Advanced Materials Research*, 445 (2012), 503-508.
2. Banerji A., Hu H., Alpas A.T., "Sliding wear behaviour of squeeze cast magnesium composite AM60-9% (Al<sub>2</sub>O<sub>3</sub>)<sub>f</sub>", *Magnesium Technology, TMS*, March 2012, 169-174.

### Conference Proceeding

3. Banerji A., Hu H., Alpas A.T., "Sliding wear behaviour of Mg alloy (AM60) reinforced with different volume fractions of Al<sub>2</sub>O<sub>3</sub> fibres", manuscript accepted for 9<sup>th</sup> International Conference on Magnesium Alloys and their Applications, July 2012.
4. Banerji A., Hu H., Alpas A.T., "Micromechanisms of low load wear of AM60 reinforced by Al<sub>2</sub>O<sub>3</sub> fibre (f) and Al<sub>2</sub>O<sub>3</sub> particle (p) + fibre (f)", poster presented at 18th International Conference on Wear of Materials (WOM), Philadelphia, PA, USA, April 2011.

Conference Presentation (Oral)

5. Banerji A., Hu H., Alpas A.T., “Sliding wear behaviour of Mg alloy (AM60) reinforced with different volume fractions of  $\text{Al}_2\text{O}_3$  fibres”, accepted for oral presentation in 9<sup>th</sup> International Conference on Magnesium Alloys and their Applications, 12 July 2012.

6. Banerji A., Hu H., Alpas A.T., “Sliding wear behaviour of squeeze cast magnesium matrix composites”, oral presentation at SAE World congress, 26 April, 2012.

7. Banerji A., Hu H., Alpas A.T., “Sliding wear behaviour of squeeze cast magnesium composite AM60-9%  $(\text{Al}_2\text{O}_3)_f$ ”, oral presentation at Magnesium Technology, TMS, 14 March 2012.